Scalable Bundle Design for Massively Parallel Neuronal Recordings *In Vivo*

Thesis

Scalable bundle design for massively parallel neuronal recordings *in vivo*

The Open University

William Wray

PhD Thesis

Neurotechnology

Amended November 2017

Declaration

This thesis is my own work but the overall project was a group effort involving significant contributions from two postdocs.

Dr. Romeo Rácz, an electrochemist, performed electrochemical characterization of electrodes and collected the data for cyclic voltammetry and impedance figures based on the iridium chloride electrolyte and pilot iridium oxide electrodeposition protocols I had developed.

Dr. Mihály Köllő, an electrophysiologist, performed mouse surgeries, developed the custom software necessary for collecting and storing data with our camera system, built the olfactometer, and designed histology protocols. We performed most *in vivo* experiments together as electrode alignment was initially labor intensive and we assessed needed electrode improvements. jULIEs were developed together but in vivo experiments were led by Romeo and Mihály.

Dr. Carles Bosch, an electron microscopist, performed micro-CT imaging experiments.

Dr. Tobias Ackels, an electrophysiologist, performed two-photon imaging experiments.

Abstract

Neural coding consists of precise interactions between related neurons. New techniques are needed to measure the time sensitive interactions within entire neural networks to understand how the brain functions. Extracellular recording is the oldest method of measuring neural activity and can sample at a temporal resolution to resolve fast spiking neurons. If scaled to a sufficiently large number of simultaneous recorded neurons, this technique would be an excellent candidate for such large scale recording. I propose the combined use of glass ensheathed microwire bundle electrodes and an infrared camera readout integrated circuit to collect massively parallel neuronal recordings *in vivo*. This design will allow for the recording of high quality signals because of the non-intrusive dimensions, low stray capacitance, and enhanced surface impedance of the electrodes, as well as the high signal to noise amplification of the camera electronics.

Here the construction of a system to record neural activity is described and its electrical properties are characterized. The results demonstrate the ability to successfully connect fabricated bundle electrodes to the indium bumps of the readout integrated circuit chip and to record voltage waveforms with a signal to noise ratio to resolve simulated spikes. *In vivo* experiments in the olfactory bulb of anaesthetized mice have resulted in recordings of action potentials from single units. The spike rate of these units increases with odor presentation and is pharmacologically inhibited which demonstrates the biological origin of the recorded activity. To further advance this technology, the stability and rate of connection to the readout electronics need to improve and insertion of electrode bundles with hundreds of more recording sites needs to be optimized. This promising design has several distinct advantages over existing fluorescence imaging and extracellular recording neurotechnologies for large scale neuronal recording.

Acknowledgments

This work would not have been possible without the guidance and support of many people. Here I thank the scientific collaborators who directly contributed help, expertise, and materials:

Romeo Rácz and Mihály Köllő have worked tirelessly to progress this project. I have spent many hours with them in the trenches making electrodes and performing animal experiments. They both provided useful data used for figures herein. Many thanks to the Bundle Brothers, and I wish the project future success.

Andreas Schaefer has continually supported me from my year in the lab in Heidelberg through my 4 years in London. As a supervisor his knowledge of the many projects developing in his lab simultaneously is astounding. Andreas made enormous effort to get this project started and and shopped around for the best possible infrared camera readout. I also thank him for providing great advice for experimental design and timely editing of scientific writing.

Former members of the bundle project team: Nikolai Kiskin, Rob Edgington. Nikolai worked to develop pulling protocols for large bundles and started a collaboration with Southampton University in regards to microwire technology. Rob went out of his way many times to teach me MATLAB programming which allowed me to analyze all stray capacitance data in this thesis. He is also going to put me as an author on his latest paper just because I helped him sort out a bunch of equipment!

The indefatigable Mina Hana, Abdul Obaid, and Nick Melosh who are developing the next generation bundle alignment system and electrode fabrication protocol and have provided thought provoking discussions.

My thesis committee: Troy Margrie, Denis Burdakov, and Justin Molloy for great feedback throughout the development of this project. Especially Justin for going out of his way to look at data with me. I wanted Ede Rancz on my committee but he wasn't a PI yet!

The rest of the Schaefer lab and former Neurophysiology division for support and ideas during my lab meetings over the years.

Martyn Stopps and Nick Burczyk for years of engineering assistance. Martyn helped me build the strain gauge circuits and independently developed the Ghost Lifter based on our experimental needs and we literally would have not been able to record any data from the camera without it. He also snuck me into the Plymouth Microelectrodes Course electronic day where I gained great theoretical knowledge of circuits and have been able to attended and demonstrate for three years running. Nick provided lots of practical advice, offered support as a 3D printing guru, and taught me the ropes of printing.

Alan Ling and the mechanical engineers who designed the electrode alignment system and were willing to modify designs after I frequently moved the goalposts.

Keith Fairhall for being a lab manager without peer.

Isabell Whitely for being amazingly cooperative while assisting with our research and helping us move labs.

Anja Schmaltz and Christian Niedworok were particularly helpful in providing practical advice with German efficiency when I first moved to Heidelberg and when I first moved to London, and were very supportive division-mates in the years that followed.

Matt Angle for getting me into Andreas's lab in the first place. Matt and his wife Steph were very supportive to me when I transitioned to life in Germany. With regards to the bundle electrode project, Matt was an endless source of ideas (and words). I hope his company Paradromics, which is related this work, continues to prosper.

Ian Oldenburg for being a great supervisor when I was an undergraduate technician and Bernardo Sabatini for hiring me even though the first time we met he was justifiably yelling at me.

Dr. Dr. Alex Brown for providing phenomenal feedback on drafts of this thesis and delivering the greatest scientific talk parody anyone has ever seen.

Martin Kaiser for proofreading drafts and refusing to take my money when I temporarily stayed in his flat in Heidelberg.

I would also like to thank the following for less science-y support:

For current and former members of Francis & the Crickets for giving me an outlet to make noise and giving me an excuse to get out of the lab. Especially labmates and rhythm section of Andrew Erskine and Tobias Ackels (extra props to Tobias for proofreading most of this thesis, teaching me LyX, and the bass-drums bond).

Dr. Drank and Mr. Fire for being best housemates I've ever had and letting me complain about work.

My parents Sue and Bill and my sister Ally for encouraging me to pursue an expatriate life and showing their love through postcards.

Finally, Bethan for taking care of me, putting up with me, and making my time in London much more enjoyable. I promise to read your thesis too.

Contents

List of Figures

Abbreviations

CB	Crystalbond 509
CMOS	complementary metal oxide semiconductor
CTIA	capacitive transimpedance amplifier
CV	cyclic voltammetry
DAPI	4',6-diamidino-2-phenylindole
EEG	electroencephalography
EEI	electrode electrolyte interface
EIS	electrochemical impedance spectroscopy
GABA	gamma-Aminobutyric acid
IrOx	Iridium Oxide
LFP	local field potential
MEG	magnetoencephalography
MRI	magnetic resonance imaging
OB	olfactory bulb
PBS	phosphate buffered saline
PDMS	polydimethylsiloxane
PEDOT	poly(3,4-ethylenedioxythiophene)
PEEK	polyether ether ketone
PFA	paraformaldehyde
PTFE	polytetrafluoroethylene
REF	reference electrode
ROIC	readout integrated circuit
SD	standard deviation
SEM	scanning electron microscope
WE	working electrode

1 Introduction

1.1 Ensemble activity in the brain

The mouse brain contains ~7.5x10^7 neurons (Vincent et al., 2010) while the human brain contains ~8x10^{10} neurons (Azevedo et al., 2009). The brain functions through time dependent interactions both between and within distinct groups of these neurons (Buzsáki, 2010; Harris, 2005). The spatiotemporal pattern of action potentials (spikes) acts as a neural code in a variety of sensory systems (Castelo-Branco et al., 2000; Panzeri et al., 2001; Laurent, 2002) and in the formation of memory (Leutgeb, 2005; Wilson and McNaughton, 1994; Engel and Singer, 2001). Limb movements are controlled by large populations of neurons in the motor cortex and the ensemble activity of these neurons has been harnessed to control external devices through brain machine interfaces (Donoghue, 2002; Lebedev and Nicolelis, 2006; Wessberg et al., 2000).

Developments in neurotechnology have enabled the monitoring of population activity *in vivo* via calcium imaging (see 1.2.4) and high density extracellular probes (see 1.3.2), as well as the manipulation of targeted cell types through optogenetics (Yizhar et al., 2011). Despite recent advances, the ability to record high fidelity data from more than a few dozen neurons simultaneously *in vivo* has proven to be challenging. Simultaneous recordings from hundreds to thousands of neurons will be needed if we are to understand the mechanisms of neural coding at the level of neuronal networks. Therefore, there has recently been a call for new or improved technologies enabling simultaneous recording from larger numbers of neurons *in vivo* to better understand the precise spatiotemporal activity patterns underlying brain function (Alivisatos et al., 2012; Marblestone et al., 2013).

1.2 Measuring neuronal activity *in vivo*

1.2.1 Origin of the action potential

The unit of communication between almost all neurons is the action potential[1]. The selective permeability of ions through channels in the neuronal membrane allow for large concentration gradients of sodium and potassium ions between the intra- and extracellular space (Hodgkin and Huxley, 1952). In most cases the all or nothing event of the action potential occurs when synaptic input depolarizes (makes less negative) the potential of the cell to its threshold, at which point the potential quickly rises with a swift influx of sodium ions and subsequently falls with an efflux of potassium (Johnston and Wu, 1995). This "spike", also known as an action potential, is propagated along the axon by regenerative

[1]There are other forms of communication in the brain. Glia communicate via various signaling mechanisms with each other and with neurons, allowing them to affect neuronal excitability and synaptic transmission (Fields, 2002).

action of voltage gated channels to terminals which contact other neurons at synapses where neurotransmitters are released. The action potential firing frequency varies greatly among different cell types and the width of an action potential at threshold ranges from ~1.6 ms for pyramidal cells to ~0.6 ms for fast spiking interneurons (Bean, 2007). In order to capture all features of the spike waveform, recordings are typically performed at sampling rates >15 kHz.

1.2.2 Intracellular recording

Action potentials result from the integration of synaptic inputs and other subthreshold fluctuations in membrane voltage, thus there is a great deal of information that can be measured about a neuron beyond its spiking activity (Bean, 2007). Two principle methods of intracellular recording are commonly used. Sharp glass microelectrodes directly impale neurons to measure membrane voltage and subthreshold events (Purves, 1981). Alternatively, microelectrodes with a larger tip diameter can be sealed to the neuronal membrane to record membrane potential from a local region of membrane, or break through the membrane to allow access to the internal potential ("whole cell") (Hamill et al., 1981). The electrode must be connected to electronics to amplify these small recorded signals without adding noise. Amplifiers used in conjunction with microelectrode recordings offer a variety of modes, including voltage and current clamp so that the effects of differing membrane voltage or injected current on the activity of the cell can be isolated and investigated. Sealing the electrode to the membrane is a skilled method, however it can be performed *in vivo* (Margrie et al., 2002) and in behaving animals (Long and Lee, 2012) and efforts have been made to automate the whole cell technique (Kodandaramaiah et al., 2012). Furthermore, *in vivo* whole cell recording has been combined with the delivery of nucleic acid vectors through the intracellular pipette, in order to combine electrophysiology with techniques such as genetic labeling or monosynaptic retrograde tracing to map the synaptic input of recorded cells (Rancz et al., 2011). Extremely small pipette tips (<30 nm) have been developed to record from individual dendrite spines in quantum dot (light emitting particles) assisted targeted recordings (Jayant et al., 2016).

Intracellular methods allow for the highest signal to noise measurement of membrane voltage and precise control of cellular activity, but only allow for simultaneous recording from a few neurons due to the difficulty of obtaining and maintaining a seal as well as the required space for multiple pipettes. This makes large scale intracellular recording unviable. The absolute amplitude of a recorded spike with intracellular recordings (20-100 mV), is much higher than that of extracellular recording (Humphrey and Schmidt, 1990)(Fig. 1.1A). The subthreshold activity of firing neurons measured with intracellular techniques typically cannot be measured with extracellular electrodes (Henze et al., 2000).

1.2.3 Extracellular recording

The oldest method of measuring the activity of neurons *in vivo* is extracellular recording. The extracellular space surrounding neurons acts as a volume conductor and has a finite resistivity (Johnston and Wu, 1995). All changes in current due to the flow of ions from proximal neurons contribute to the potential field at a given point (Buzsáki et al., 2012). When the conductive metal within an electrode penetrates tissue and enters the extracellular space, an electrode-electrolyte interface (EEI) is formed and the electrode acquires a potential (Geddes, 1972). At the EEI, a reaction occurs in which the flow of ions is converted to current flow in electrons. This reaction is either capacitive where the EEI double layer charges and discharges or faradaic where the electrode surface is oxidized and reduced (Cogan, 2008).

This extracellular electrode is measuring the field potential at a single point, compared to a distant reference electrode ground. When the extracellular recording is able to resolve action potentials from a single neuron it is said to record "unit" activity (Fig. 1.1B). As the extracellular space is a volume conductor, electrodes often record the activity multiple neurons simultaneously, known as multi-unit activity, or many/networks of neurons, known as the local field potential (LFP, Fig. 1.1A). Extracellular recordings are often selectively filtered to separate high frequency unit activity (high pass) and lower frequency LFP (low pass). LFP can be measured less invasively by placing electrodes on the surface of the cortex subdurally, known as electrocorticography (ECoG), but with significantly lower signal strength (Viventi et al., 2011; Khodagholy et al., 2015, 2016).

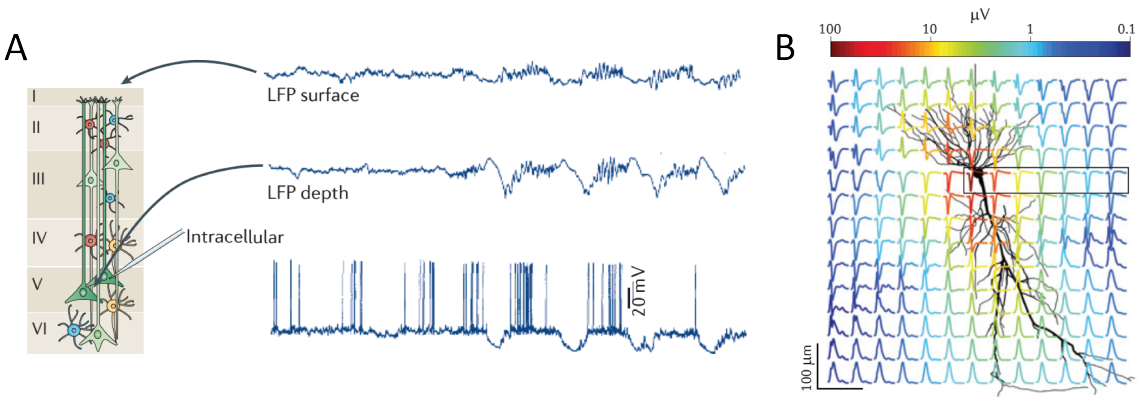

Figure 1.1: Intracellular and Extracellular recording waveforms. **(A)** Simultaneously recorded superficial and deep LFP traces and an intracellular recording from a layer 5 pyramidal neuron (Buzsáki et al., 2012). **(B)** Simulated data of normalized extracellular spike waveforms in the vicinity of a neuron (Buzsáki et al., 2012).

The amplitude of the recorded potential field is highest near the membrane and steeply drops with increasing distance of the recording electrode from the membrane (Buzsáki et al., 2012). Very close to the membrane, an extracellularly recorded action potential can reach several mV in amplitude (Humphrey and Schmidt, 1990). The recorded potential will be positive where current flows out of a cell (current source) and it will be negative where there is inward current (current sink). The recorded waveforms vary greatly with distance of the recording electrode from the membrane, as well as the electrode's orientation in relation to the sources and sinks created by the neuronal geometry, and the specific portion of the membrane local to the electrode (Gold et al., 2006)(1.1B). Surprisingly, a method for ground truth validation of the source of extracellular potentials and multi-unit activity was only developed recently (Neto et al., 2016).

Electrodes can also be used in a configuration in which they apply an extracellular current to depolarize neuronal membranes, in order to stimulate neurons with defined patterns of activity (Brummer et al., 1983). Stimulating electrodes are desirable for experimental neuroscience but also have wide-ranging clinical applications and for years their efficiency has been tested in a variety of animal models (Rose and Robblee, 1990; Merrill et al., 2005).

1.2.4 Foreign body response

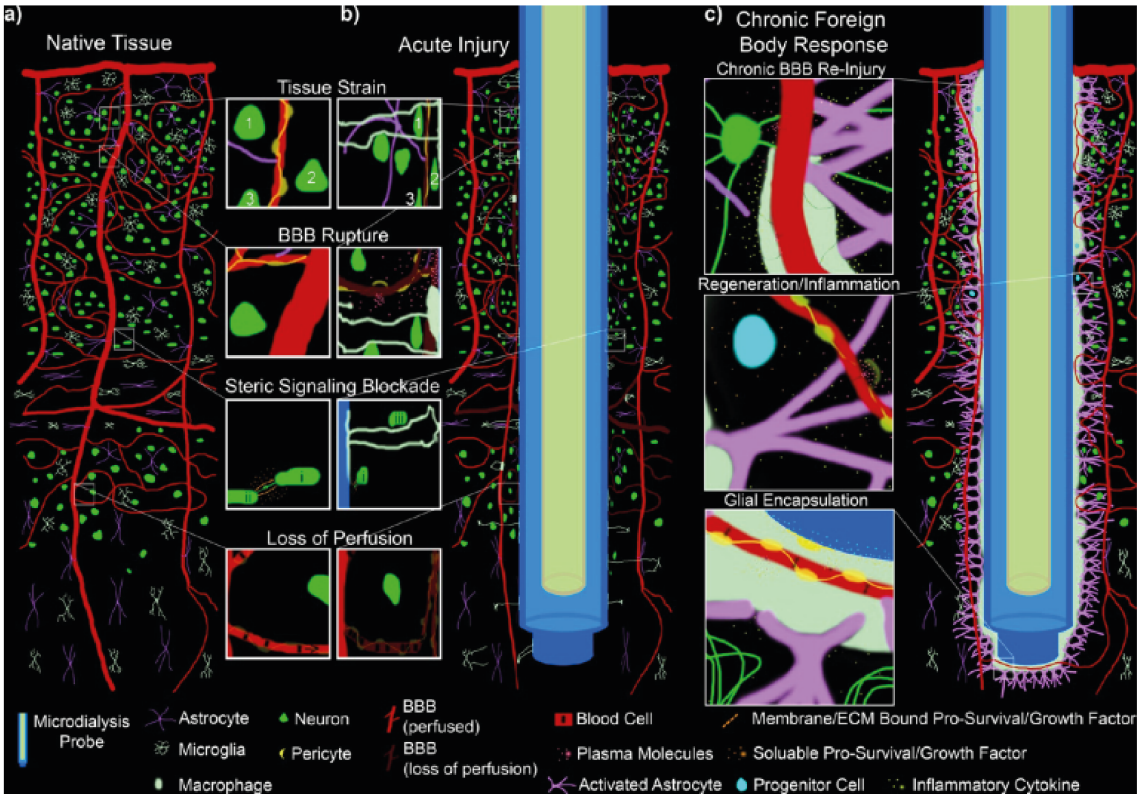

Figure 1.2: Tissue response to an inserted probe. This schematic displays the movement of neurons and a variety of glial cell types within native brain tissue (A), after acute injury (B) and after the probe has remained inserted chronically (C). The diameter of the microdialysis probe is a similar scale to that of a silicon probe (Kozai et al., 2015b).

Brain tissue is a dynamic system of neurons, neuroglia, and vasculature (Fig. 1.2A). Volumetric tissue displacement occurs whenever a recording electrode is inserted into the brain, which causes mechanical stress to cells and ruptures the blood brain barrier (BBB). The response to the foreign body (inserted probe) is known as gliosis and mediated via microglia and astrocytes (Polikov et al., 2005). Immediately after insertion, microglia cells within a few hundred microns of the probe are activated (Kozai et al., 2012b). Within minutes after insertion, microglia stretch towards the probe. Also after acute insertion, neuronal cell death can be caused by the steric blockade of signaling molecules and growth factors and a loss of perfusion (blood flow) due to vascular damage (Fig. 1.2B).

After 12 hours microglia begin moving towards the insertion site and by 24 hours have surrounded the probe (Kozai et al., 2015b). Astrocytes are most active during the first week of the foreign body response and 2-3 weeks after insertion form a compact sheath around the activated microglia (Fig. 1.2C). This inflammatory response can create a glial scar around the electrode which prevents neural regeneration via progenitor cells and causes additional cell death (Fitch et al., 1999). Micromotions in the brain (from

blood circulation and respiration) can accelerate the response against electrodes which are anchored to the skull (Kim et al., 2004).

Even when probes are removed directly after insertion, there is still evidence of chronic changes to the local tissue environment (Biran et al., 2005). Many properties of electrodes are known to affect the foreign body response. Injury site size decreases with smaller electrodes and chronic electrode performance improves when electrode cross sectional area decreases (Wellman et al., 2017). Microglia *in vitro* have been shown to respond to material stiffness and to move from softer to stiffer substrates (Bollmann et al., 2015). In accordance with this, coating stiff electrodes with soft materials has been shown to reduce gliosis and improve neuronal health *in vivo* (Sridharan et al., 2016).

The density difference of the probe and the surrounding tissue is another property which can cause signal quality to degrade chronically (Lind et al., 2013). There is not a consensus in the literature of the effect of insertion speed on the tissue response as faster speeds have been shown to cause increased force and long term gliosis, but slower speeds have been shown to increase the damage to vasculature (Wellman et al., 2017). Large blood vessels can be avoided during insertion with imaging techniques, but this is more difficult for electrodes with more complex geometries (e.g. multiple shanks).

A variety of dyes are commonly used as markers in histological preparations to measure the response of brain tissue to electrode insertion. The fluorescent dye Evans blue binds to albumin which is released when the BBB is disturbed (Kozai et al., 2012a). The immunohistological stains glial fibrillary acidic protein (which fluorescently tags astrocytes) and Iba-1 (fluorescently tags microglia) allow for monitoring of gliosis (Kozai et al., 2012a). Propidium iodide is a fluorescent stain which enters cells with damaged membranes and thus can be used as a marker for cell membrane integrity (Blanche et al., 2005). These and other markers can help qualitatively estimate the brain tissue damage caused by electrode insertion over acute and chronic timescales. Histology after insertion should be assessed for all electrode technologies in order to measure the foreign body response.

1.2.5 Imaging techniques

The simultaneous activity of many neurons can also be measured without the need for inserting electrodes into tissue with optical techniques. Changes in intrinsic properties (light scattering, absorption or fluorescence of chromophores) or light emission via fluorescence can be linked to spiking activity and measured with a detector. Activity dependent intrinsic signals (local blood volume and oxygen delivery) can be imaged through a thinned skull or cranial window in behaving animals but suffers from low spatial resolution (Frostig et al., 1990). Voltage sensitive dyes bind to the neuronal membrane and emit potential dependent fluorescence that can be measured with photodiodes or a camera

(Ebner and Chen, 1995). Calcium indicators, which produce large changes in fluorescence when bound to calcium ions, can be loaded into cells through a patch pipette, bulk loaded through de-esterification by native cell processes, or genetically encoded to specific cell types (Pologruto et al., 2004; Smetters et al., 1999). Intracellular calcium transients measured with fluorescence microscopy are evoked by action potentials and depend on indicator concentration and buffering properties (Helmchen et al., 1996). However these indicators are nonlinearly related to neural activity and are fundamentally an indirect measure of membrane potential (Nauhaus et al., 2012).

Two-photon microscopy is a fluorescence imaging technique where near-infrared excitation light is delivered by a femtosecond pulsed laser which scans across the sample to excite fluorescent indicators (Denk et al., 1990). This technique allows for high resolution *in vivo* imaging of neuronal morphology (even individual dendritic spines) at up to 1-2 mm in depth without inducing additional photodamage to tissue (Kerr and Denk, 2008). This depth limitation arises principally from the scattering of light in the brain. However increasing illumination power for a stronger fluorescence signal can cause a nonlinear increase in photodamage (Hopt and Neher, 2001). The recorded change in fluorescence in this technique is also based on calcium indicators and measured through a thinned skull or cranial window, which enables chronic recording *in vivo*. Two-photon imaging experiments are generally performed in head-fixed preparations which can be designed to allow animals to walk or run on a ball during imaging (Dombeck et al., 2007). It is very difficult to move the microscope with the animal during behavioral experiments due to the required bulky optics of most two-photon systems. However, a miniaturized microscope was created with laser light delivered through fiber optics which allowed two-photon imaging while animals freely behaved (Helmchen et al., 2013). Recent advances in microscope miniaturization even allow two-photon imaging of individual spines while mice freely behave in an arena (Zong et al., 2017).

There are some limitations in temporal resolution due to the kinetics of the calcium signal and calcium indicators. However calcium indicators have improved to allow the recording of individual action potentials (see GCaMP6, Chen et al., 2013), so the bottleneck for improving speed is mostly due to the microscopy technology. Laser scanning speeds have improved with acousto-optic deflectors to allow a sampling rate at nearly 1 kilohertz frequency (Grewe et al., 2010). Two-photon imaging has developed to allow simultaneous single neuron optogenetic manipulation and recording from small groups of neurons *in vivo* over the course of weeks (Packer et al., 2014). New technology even permits imaging in multiple focal planes simultaneously in the mouse cortex *in vivo* through the use of spatial light modulators (Yang et al., 2016). The field of view of two-photon microscopy is also expanding from ~1 mm^2 to >10 mm^2 due to the development of more advanced laser scanning systems (Stirman et al., 2016; Sofroniew et al., 2016).

Though two-photon microscopy has a superior resolution and imaging depth than other

techniques, it has limitations that will prevent it from recording from large brain volumes. During two-photon imaging, light is dissipated as heat in the brain. The laser power required to excite large fields of view would inevitably cause thermal damage to tissue. For an entire mouse brain, delivering 1 excitation pulse per neuron per frame (a low estimate because more that 1 pulse is usually required to excite detectable fluorescence) at 1 kilohertz frequency would dissipate about 10 W (Marblestone et al., 2013). Typical two photon experiments use ~50 mW laser power and tissue damage begins to occur in the mouse brain with ~250 mW (Podgorski and Ranganathan, 2016). Damage is also caused to brain tissue before imaging during microinjection of calcium indicators or GCaMP encoding virus. The depth limitation of 1-2 mm also prevents 2-photon microscopy from imaging anything below superficial layers of cortex. Even when the underlying technology (laser scanning speed, detector density, etc.) improves, these limitations will persist.

1.2.6 "Non-invasive" methods

Neural activity can also be measured from outside the skull, though more indirectly than the previously described methods. In electroencephalography (EEG), electrodes on the scalp record a spatiotemporally smoothed version of the LFP. This technique cannot record individual spikes because the extracellular signal is weakened through the soft and hard tissue barrier between the electrode and the neuron (Buzsáki et al., 2012). A similar technique is magnetoencephalography (MEG) which uses superconducting quantum interference devices to measure magnetic fields produced by neurons (Hämäläinen et al., 1993). MEG has better spatiotemporal resolution than EEG but still cannot resolve individual spikes and requires complex shielding. Both techniques are commonly used in human studies to analyze the different frequency "waves" of activity during sleep (Hughes et al., 1976).

Magnetic Resonance Imaging (MRI) measures local changes in magnetic fields in tissue. In blood-oxygen-level dependent functional MRI, the activity of neurons is related to changes in vascular concentration of paramagnetic deoxyhemoglobin (Ogawa and Lee, 1990). This technique is completely noninvasive and allows scanning through the full depth of the brain, but suffers from very poor spatial resolution compared to optical techniques and its temporal resolution is limited by blood flow in the brain and thus cannot resolve individual spikes. In a method combining MRI and optogenetic expression for circuit mapping *in vivo*, spatial resolution was limited to 100x100x500 µm voxels, far worse than single cell resolution (Desai et al., 2011).

An additional technique for mapping large scale neuronal activity could be the use of engineered DNA polymerases which record time-varying signals into DNA "ticker tape" (Glaser et al., 2013). However, this exploratory technique would not be able to temporally resolve spiking activity and has yet to be demonstrated *in vivo*.

1.3 Increasing yield of simultaneously recorded units

1.3.1 Single wire electrodes to multielectrode arrays

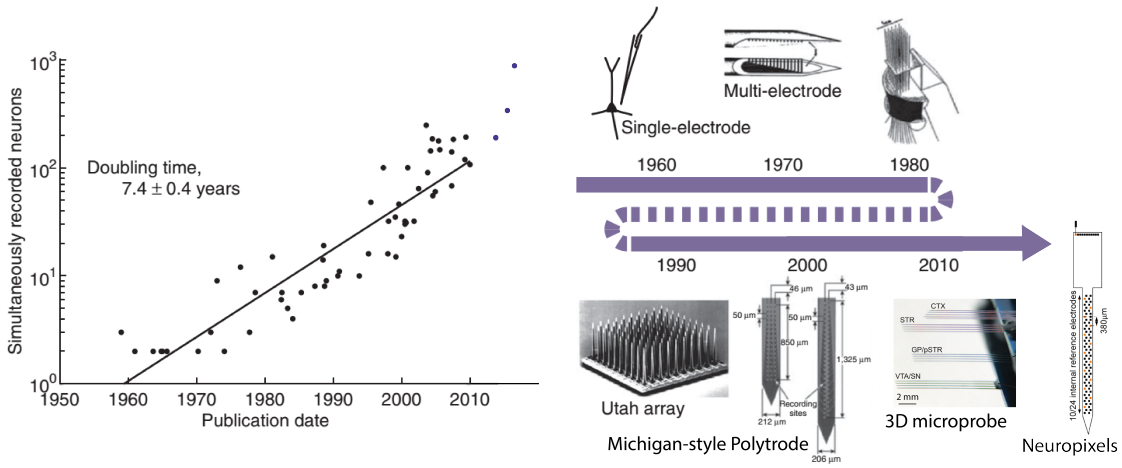

Figure 1.3: Exponential increase in simultaneously recorded neurons. The ~7.4 year doubling time for the number of simultaneously recorded neurons is much slower than Moore's law (transistor count doubling every 2 years). 3 modern studies were added to the plot, 163 units recorded by Berényi et al., 2014, the 3D microprobe which recorded 308 units by Shobe et al., 2015, and the Neuropixels probe which recorded 831 units in a dual probe recording by Steinmetz et al., 2016. The plot is updated from that of Stevenson and Kording, 2011.

The number of simultaneously recorded neurons *in vivo* has increased steadily since the introduction of extracellular recording, but has increased far slower than the growth of integrated circuit density, as described by Moore's Law (Fig. 1.3, Stevenson and Kording, 2011). This increase in probe recording density is a testament to the inherent scalability of extracellular recording. One of the earliest designs of an extracellular recording electrode was a sharpened, lacquer insulated tungsten wire with a tip less than 0.5 µm in diameter which was used to measure spiking activity from single neurons in a cat model (Hubel, 1957). Extracellular electrodes then developed from the 2 recording site stereotrode (McNaughton et al., 1983) to the 4 site tetrode (Wilson and McNaughton, 1993; O'Keefe and Recce, 1993; Harris et al., 2000). Tetrodes were constructed by braiding 4 insulated nichrome wires together and plating their tips with gold (Gray et al., 1995; Nguyen et al., 2009). Tetrodes have the advantage of recording multiple neurons (isolated by spike sorting, see 1.3.4) and are mechanically stable enough to be used for chronic recordings (Buzsáki, 2004). Tetrodes are commonly controlled with chronically implanted microdrives to allow insertion without the mechanical stress of head fixation and the repositioning of the electrodes in different brain regions during behavioral experiments (Yamamoto and Wilson, 2008; Kloosterman et al., 2009).

To increase the number of recording sites further, many wires can be grouped together

into multielectrode arrays (MEAs) (Nicolelis et al., 1997; Ward et al., 2009). MEAs, first designed for rat and monkey models, were composed of stainless steel or tungsten microwires, and like tetrodes featured microdrives for electrode placement (Kralik et al., 2001; Nicolelis et al., 2003). The population recordings from many individual neurons allowed the first glimpse into neuronal ensemble activity in freely moving animals.

1.3.2 Silicon probes

The next major advancement in *in vivo* extracellular recording was the development of silicon probes. These probes were first developed by electroplating gold electrodes with custom spacing exposed by photolithography on a silicon wafer and insulating with silicon dioxide (Wise et al., 1970). For years the two major designs of silicon probes have been planar multisite Michigan probes which evolved from the first electrodes on silicon at the University of Michigan (Drake et al., 1988) and planar needle Utah arrays developed at the University of Utah (Maynard et al., 1997, see Fig. 1.3). The first Utah arrays were insulated in polyimide and the needle tips are exposed revealing platinum recording sites. The major advantage of these arrays is the horizontal spacing of recording sites which allows them to record from neurons throughout a cortical area. Utah arrays have been used in a variety of chronic experiments in rodents and primates and were the first intracortical array approved for usage in human studies (House et al., 2006). Michigan probes however have more flexible geometry than Utah arrays allowing them to match the spacing of cells and layers in desired brain structures.

Michigan-style silicon probes have advanced to contain on-chip electronics that can help to increase signal amplitudes and decrease the number of external leads (Najafi and Wise, 1986; Wise et al., 2008). They also progressed to have 54-sites on a single shank (Blanche et al., 2005, see Fig. 1.3) and later advanced to 3D arrays with recording sites on both sides of the shank to improve the spatial resolution of recording (Du et al., 2009). Though it has yet to be adopted as a standard method, there are numerous reports of wireless readout systems for silicon probes to limit the need for tethering in behavioral experiments (Kim et al., 2009; Chestek et al., 2009; Schwarz et al., 2014; Wise et al., 2004). Silicon probes have also been combined with microdrives in order to reposition the electrodes *in vivo* in rodents (Michon et al., 2016; Berényi et al., 2014) and primates (Mendoza et al., 2016) though it has also been demonstrated that high quality recordings can be maintained over months with immobile probes (Okun et al., 2016).

In recent years silicon probes were fabricated to have 8 individual shanks within a single wafer and were used in *in vivo* experiments with 512 total electrodes (using x2 256-site wafers simultaneously, Berényi et al., 2014). The number of simultaneous recording sites increased again to 1024 (x4 256-site probes, Shobe et al., 2015, see "3D microprobe" in Fig. 1.3) and 1000 more densely packed electrodes on 5 shanks on 1 printed circuit board

(PCB) for "spatially oversampling" neurons (Scholvin et al., 2016). Due to advances in lithographic fabrication techniques, silicon probes also can now have recording sites as small as a few hundred square microns or less. The latest innovation in recording site density is the Neuropixels probe which has 384 channels (from 966 selectable electrodes), on probe amplification, and can record at 30kHz with low noise Lopez et al., 2017. Dual recordings with 2 Neuropixels probes simultaneously allowed for the recording of more than 800 units from 5 different brain regions in an acute experiment in an awake head-fixed mouse which broke the existing record for simultaneously recorded units *in vivo* (Steinmetz et al., 2016, see Fig. 1.3).

Though silicon probes are the most widely used technology to record with single unit resolution *in vivo*, they have several limitations. The major disadvantage is that during implantation they induce a foreign body response which causes tissue damage at acute and chronic timescales (1.2.4). Signal quality can degrade due to this inflammatory tissue response and to the mechanical mismatch between commonly used electrode materials within the probe itself (Kozai et al., 2015a). Silicon probes are also generally spatially restricted to linear designs penetrating perpendicular to the surface of the brain which prevents them from recording horizontally distributed neuronal networks (Csicsvari et al., 2003). If increasing the sampling of neurons is achieved simply by increasing the number of probes, the total brain displacement volume and total tissue damage would increase proportionally. However, volume displacement constraints are unlikely to be a fundamental limit to whole brain recordings with extracellular electrodes. But depending on how many neurons can be recorded by a single electrode, their diameter would need to decrease to submicron scales to record from an entire mouse brain without displacing >1% of total tissue volume (Marblestone et al., 2013). To create probes with more recording sites, microfabrication of the integrated circuits which contain the signal amplifiers will need to scale up which will significantly increase the cost and complexity of the readout electronics. These limitations will cause the number of simultaneously recorded neurons *in vivo* to plateau at some point unless novel technological approaches are developed.

1.3.3 Functionalization of small recording sites

When metal recording sites get smaller, the surface area of the electrode decreases and impedance increases. This makes it more difficult to record small extracellular voltages. Electrochemical functionalization, a process in which the chemical composition and surface morphology of recording sites is modified, is commonly performed on tetrodes and MEAs to lower the impedance of electrode surfaces and increase the signal to noise ratio by increasing the surface area through roughening or enhancing electron transfer at the EEI (Heim et al., 2012).

Iridium Oxide (IrOx) is a well established thin film for stimulating and recording electrodes. IrOx films were first developed and tested *in vitro* on insulated iridium metal stimulating electrodes through repeated oxidation and reduction which produced IrOx on the electrode surface (Conway and Mozota, 1983; Robblee et al., 1983). Films formed in this manner are known as "activated" IrOx films (AIROFs) and can inject charge in a fast and reversible faradaic reaction (Cogan et al., 2006, see Fig. 1.4). Another method of creating IrOx electrodes was developed by reactive sputtering from Ir metal in oxidizing plasma onto recording sites (known as SIROF) (Hackwood, 1981; Anderson et al., 1989; Klein et al., 1989; Wessling et al., 2006). SIROFs have similar charge injection properties to AIROFs, but can be deposited on non-iridium substrates. In a third method, IrOx films can be deposited onto non-iridium electrodes via electrodeposition (EIROF) (Yamanaka, 1989). EIROFs are formed by cycling voltage in an iridium salt solution where in a faradaic reaction the Ir^{4+} reduces to Ir^{3+} creating the dark blue oxide (Meyer et al., 2001), the morphology of which is determined by the charge density during electrodeposition (Mailley et al., 2002). Cyclic voltammograms (CVs) display this change in redox state and electrochemical impedance spectroscopy (EIS) demonstrates the decrease in recording site impedance due to the EIROF (Mailley et al., 2002). EIROFs have been electrodeposited on electrodes intended for extracellular recording with recordings substrates of gold, platinum, platinum-iridium, and stainless steel (Meyer et al., 2001) as well as more elaborate substrates like gold nanowires (Yoon et al., 2010) and carbon fibers (Gillis et al., 2017). IrOx electrodes have been used chronically *in vivo* (though almost exclusively as AIROFs and SIROFs and more often for stimulation than recording) in a variety of animal models (Weiland and Anderson, 2000; Kane et al., 2013; Cogan et al., 2006; Ward et al., 2009). However, IrOx films are known to degrade over time as evidenced by delamination of the film and quantified by a decrease in charge storage capacity (CSC, the area under the CV curve and a quantification of an electrode's ability to store stimulating charge) (Cogan, 2008; Negi et al., 2010).

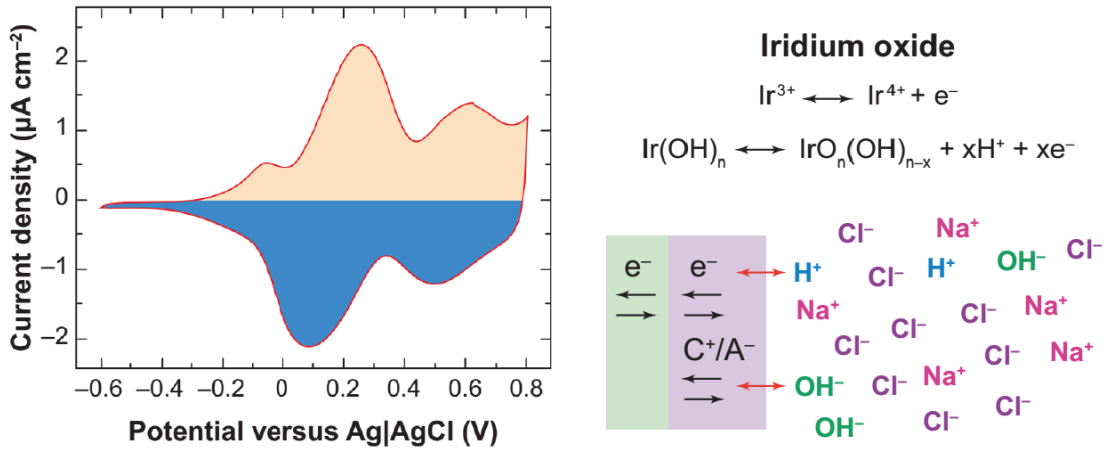

Figure 1.4: Iridium oxide electrochemistry. CV of IrOx showing its characteristic redox peaks (left) and the reversible faradaic reaction of IrOx at the EEI (right)(adapted from Cogan, 2008).

As an alternative, electrically conductive polymers have been used to lower the impedance of electrodes. Poly(3,4-ethylenedioxythiophene) (PEDOT) is an electrically conductive polymer used on stimulating and recording electrodes. PEDOT is formed by polymerizing the EDOT monomer in solution with poly(styrene sulfonate) potentiostatically (constant voltage) or galvanostatically (constant current) (Cui and Martin, 2003). PEDOT films have been found to have even lower impedance and greater charge storage than IrOx films and can be electrodeposited on gold, iridium, platinum-iridium, and platinum (Wilks et al., 2009; Green et al., 2012) and have been used to record activity chronically *in vivo* (Ludwig et al., 2006). PEDOT electrodeposits have been successfully loaded with bioactive molecules (including peptides such as nerve growth factor or drugs such as dexamethasone) or carbon nanotubes (Luo et al., 2011; Castagnola et al., 2016) to enhance biocompatibility and can be prepared in different non-film morphologies such as nanotubes (Boehler et al., 2017; Xiao et al., 2006; Abidian et al., 2006; Green and Abidian, 2015; Heim et al., 2012).

Carbon nanotubes (CNTs) are a unique material for electrode coating due to their high surface/volume ratio, physical flexibility, and cell adhesion properties (Bareket-Keren and Hanein, 2013). CNTs can be synthesized on electrodes via chemical vapor deposition, producing vertically aligned CNTs (Gabay et al., 2007; Nguyen-Vu et al., 2007) or co-electrodeposited with gold particles at a lower temperature (Keefer et al., 2008; Xiang et al., 2014). Beyond its potentially improved biocompatibility, CNT coatings have been shown to have lower impedance and charge storage capacity than both IrOx and PEDOT films (Jan et al., 2009).

There are a few other notable state of the art electrode surface coatings that have recently been established. Gallium phosphide nanowire based electrodes have been used to record single units in acute *in vivo* recordings (Suyatin et al., 2013) and electrodeposited plat-

inum grass (Boehler et al., 2015) and electrodeposited PEDOT on IrOx or nanostructured Pt have been tested *in vitro* and proposed as superior novel electrode coatings (Boehler et al., 2017). Graphene has been used on flexible parylene ECoG electrodes which are transparent enough to simultaneously perform imaging and electrophysiology *in vivo* (Kuzum et al., 2014; Park et al., 2014). Also, attempts to enhance biocompatibility beyond just the recording interface were made by nanostructuring the shank of silicon probes which increased neuronal survival adjacent to the probe (Bérces et al., 2016). These newer coating technologies have some unique characteristics, but IrOx, PEDOT, and CNTs remain the most commonly used electrode coatings for neural recordings.

1.3.4 Spike sorting

Ideally large scale recording techniques would allow for the detection of the spiking activity from single neurons. However, the recording sites of all current extracellular technologies pick up the activity of multiple units due to the conducting nature of the extracellular space and the proximity of cells. To isolate single units from multi-unit activity, a variety of spike sorting algorithms have been developed (Lewicki, 1998). These techniques generally: detect spikes from a band pass filtered signal, extract features from the spike shape, apply a clustering algorithm to the features, and attribute each cluster to a unit (Rey et al., 2015). There are a variety of methods for feature extraction including principal component analysis and wavelets.

Spike sorting can be applied beyond a few neurons to the ensemble level in which spiking activity is analyzed as a representation of external stimuli. In population decoding, spiking activity in response to a variety of known stimuli are recorded (encoding) to train a model which can then be used to estimate an unknown stimulus from spiking activity alone (decoding) (Brown et al., 1998). These and other methods for analyzing sorted spike trains (such as maximum likelihood, cross coherence, and information theory) are subject to certain limitations. Most algorithms require large datasets of spike trains to perform, evolving spike waveforms can corrupt spike sorting, and different algorithms can give different results when applied to the same datasets (Brown et al., 2004).

Due to the increased recording site density of modern probes, the activity pattern along the probe shank can be used to localize the cell bodies of neurons and contains information about the morphology of the neuron, which is often neglected during spike sorting (Delgado Ruz and Schultz, 2014). Spike sorting methods have also become specifically tailored to the specifications of the most modern extracellular probes (Jun et al., 2017; Pachitariu et al., 2016; Rossant et al., 2015).

1.3.5 Advanced extracellular probe technologies

There are several novel extracellular probe technologies that are being adapted for the challenges of recording *in vivo* and to overcome the weaknesses of standard silicon probes. Due to the mechanical mismatch between common electrodes and tissue, there is a great need for softer probes that are mechanically compliant with tissue for longer *in vivo* recordings (Lacour et al., 2016). A wide variety of soft materials have been used for *in vivo* electrodes including Parylene (Takeuchi et al., 2005; Kim et al., 2009; Sohal et al., 2014), PDMS (Kozai and Kipke, 2009; McClain et al., 2011), and other custom polymers (Lacour et al., 2010; Harris et al., 2011; Ware et al., 2012; Kolarcik et al., 2015). The disadvantage of these probes is that their softness makes them more difficult to insert into tissue and they often require external shuttles to properly penetrate tissue (Kozai and Kipke, 2009; Gilgunn et al., 2012).

Another method of decreasing the tissue damage caused by probes during *in vivo* electrophysiology, is decreasing the overall probe volume. Bundles of 12.5 µm diameter tungsten wires embedded in gelatine were inserted into rat cerebral cortex and the gelatine coating reduced acute tissue damage compared to uncoated control wires (Lind et al., 2010). In a similar manner, gelatine was also used to insert clusters of 29 ultrathin platinum electrodes which spread in tissue and successfully recorded from units in the deep brain of rats (Etemadi et al., 2016) (Fig. 1.5A). Microscale carbon fibers are another alternative to the standard glass, silicon, and metal materials generally used in microelectrodes. Carbon fibers <5 µm in diameter have been used as a 16-channel electrode array to record firing patterns over months from the brains of behaving zebra finches (Guitchounts et al., 2013) and in a later study were modified to have a lower impedance with electrodeposited IrOx films (Gillis et al., 2017). Another carbon fiber based electrode design was used to record *in vivo* chronically in rats with a reduced tissue response compared to silicon probes (Kozai et al., 2013). Similar fibers were adapted into arrays of 16 channels which recorded chronically from rats with tissue insertion aided by poly(ethylene glycol) (PEG) (Fig. 1.5B) (Patel et al., 2015).

Other state of the art materials and fabrication methods have been applied to the development of extracellular probes. Conventional lithography processes were used to produce a 3D macroporous mesh electrode made of flexible SU-8 photoresist polymer with recording sites on thin arms which bend outwards during tissue insertion which was aided by freezing the electrode in buffer solution (Xie et al., 2015). The 19 field effect transistor sensors on a single probe were used to acutely record LFP and single units from rat somatosensory cortex. Another use of lithography in a novel configuration was for the development of nanoelectronic thread (Luan et al., 2017). These electrodes (Fig. 1.5C) were also composed of SU-8 photoresist, had platinum or gold recording sites, and were so thin (<5 µm) that a micropost shuttle was needed to insert them into the brain. The nanoelectronic thread

electrodes were able to record single units over the course of months and simultaneous 2 photon imaging revealed no neuronal degradation or scarring.

Thermally drawn polymer fibers have also been used as a material for extracellular probes. Flexible polymer probes combining conductive carbon black doped polyethylene (for recording sites) and polycarbonate (as a fiber optic) were constructed to allow simultaneous extracellular recording and optogenetic stimulation in the mouse spinal cord *in vivo* (Lu et al., 2014). The same group advanced their thermal drawing process to incorporate conductive polyethylene or tin recording sites (Fig. 1.5D) and channels for drug delivery (Canales et al., 2015). These probes continued to function after bending and could record from mouse prefrontal cortex *in vivo* for up to 2 months. Next the channels in the probes were used to inject viruses to target specific neurons for optogenetic stimulation and record from neurons all within one surgical implantation from 2 probes in different brain regions simultaneously in behaving mice (Park et al., 2017).

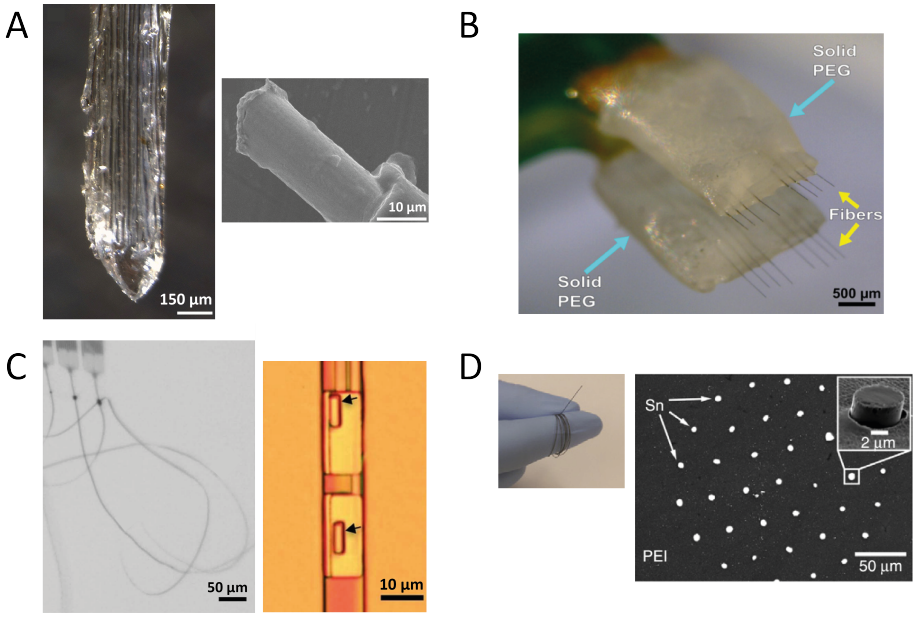

Figure 1.5: Advanced *in vivo* extracellular recording technologies. **(A)** A platinum cluster electrode embedded in gelatine (Left) and the de-insulated tip of a single wire (Right) (Etemadi et al., 2016). **(B)** An array of 16 carbon fibers embedded in polyethylene glycol (Patel et al., 2015). **(C)** Multiple nanoelectronic thread probes in water (Left) and 2 of the recording sites on a single probe (Right) (Luan et al., 2017). **(D)** A thermally drawn electrode fiber wrapped around a finger (Left) and the cross section of a drawn fiber of 36 tin electrodes in poly(ethermide) cladding (Right). The inset is a single wire etched with oxygen plasma (Canales et al., 2015).

These technologies offer improved tissue integration for chronic study of neural activity because they are formed from ultrasmall, soft, and flexible materials. However, each technique has limited scalability. Connecting more than a few tens of electrodes to the same electronic readout has yet to be demonstrated. Also, there will be greater tissue displacement and damage as the number of electrodes inserted together increases and techniques have not been developed to decrease electrode sizes further and enable them to insert into tissue.

2 Concept

2.1 Thesis Aims

New approaches are needed to simultaneously record with high temporal resolution from more neurons than the tens to hundreds of cells that are typically recorded with silicon probes. Extracellular recording allows the recording of fast spiking activity of individual neurons and has a higher temporal resolution than optical methods. Additionally, extracellular arrays can reach deep brain structures and their geometry can be designed for the specific brain area of interest.

Building on previous experience with nanoscopic intracellular (Angle and Schaefer, 2012) and extracellular probes (Angle and Schaefer, unpublished), the combined use of glass ensheathed gold microwire bundles with a high speed, low input capacitance Readout Integrated Circuit (ROIC) chip readout is proposed as an *in vivo* extracellular recording technology. It is difficult to record subtle changes in extracellular potentials at these electrode surface dimensions, so a low impedance electrochemically deposited iridium oxide film will be employed. The major advantage of this design over existing extracellular techniques is its scalability. Recordings could be made with adequate temporal resolution from an entire chip consisting of hundreds of thousands of potential amplifiers. Additionally, commercial infrared camera electronics will continue to develop independently of this technology, providing the opportunity to record with even more pixels at higher speeds. Due to my lab's wealth of experience with the olfactory system, the target for pilot *in vivo* experiments was the mouse olfactory bulb (OB) (Fukunaga et al., 2012; Kollo et al., 2014).

2.2 Advancing readout electronics

Whilst much progress has been made in electrode design, amplifiers and interfaces to record from such electrodes have also needed to advance. The usage of novel electronics for an electrophysiology setting was required to achieve higher density recording of neurons *in vitro*. Complementary metal oxide semiconductor (CMOS) chips, classically used in digital imaging devices, are fabricated in standardized processes and contain dense arrays of thousands of recording sites which can sample in the kilohertz range (Obien et al., 2015). CMOS readouts have been used to measure extracellular activity (Bakkum et al., 2013; Eversmann et al., 2003) and to stimulate in cultured neurons (Lei et al., 2011), in brain slices (Frey et al., 2009; Ferrea et al., 2012), and in whole retinas (Fiscella et al., 2012; Maccione et al., 2014). CMOS chips have also been adapted to novel electrode architectures including micro-nails (Huys et al., 2012) and nanowires for intracellular recordings (Robinson et al., 2013; Abbott et al., 2017; Liu et al., 2017). CMOS fabrication processes

have also been used to develop planar probes to record extracellularly *in vivo* (Ruther and Paul, 2015; Malerba et al., 2016). A disadvantage of such high density probes is that the conducting lines can capacitively couple to create significant crosstalk between channels (Lopez et al., 2014).

For an even larger number of recording sites, a ROIC imaging chip with 81,920 pixels was used to record extracellular activity from a retinal section *in vitro* (Johnson et al., 2012). Johnson et al. recorded at multiple sampling rates from selectable regions of a ROIC chip directly bonded to a microwire glass array to acquire extracellular traces with similar waveforms and signal to noise as compared to traditional amplifiers.

ROIC chips are traditionally used in infrared cameras and are composed of a readout array fabricated in silicon with an array of indium bump pixels. The pixels are bonded to a photosensitive layer to convert light from a photodetector to an amplified voltage (Fig. 2.1). Capacitive feedback transimpedance amplifiers (aka current to voltage converters) are connected to each pixel and perform the voltage amplification. The detector array of these cameras are very dense and the readout electronics record at high frequencies (>10 kHz) to support the performance needs of infrared imaging (Hsieh et al., 1997). ROICs are available commercially in a variety of array sizes and sampling rates from such imaging companies as Ratheon, Selex, FLIR, and Xenics. It is difficult to compare the exact specifications (sampling rate, noise, etc.) of the chips from different infrared camera models as this information is not publically available. Due to the fabrication complexity of the ROIC electronics and its specific industrial market, they are generally more costly than CMOS chips.

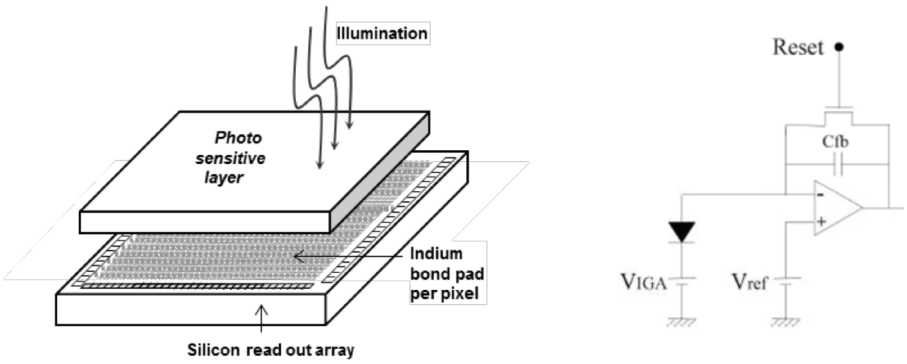

Figure 2.1: Readout Integrated Circuits. Schematic of a photosensitive layer bonding to the indium bumps of a ROIC interface (Rider et al., 2011)(left). Commonly used orientation of a capacitive feedback transimpedance amplifier (V_{IGA}= voltage of indium gallium arsenide pixel, V_{ref} is voltage reference , C_{fb}= feedback capacitor)(Neys et al., 2008)(right).

The transimpedance amplifiers in these arrays have very similar properties to the amplifiers in extracellular recording headstages and thus the ROIC readout without a photosensitve layer can be considered an array of extracellular amplifiers. The major advantage of a ROIC readout over standard commercial recording systems is its scalability. The tens to hundreds of thousands of additional channels (pixels which can perform amplification) allow the potential for higher channel counts than any other current technology permits. This is achieved while sampling at a rate equal to or greater than commercial extracellular recording systems.

2.3 Glass ensheathed microwires as electrodes

For high density extracellular recording, electrodes need to have very small recording surfaces and be well insulated from each other. Larger diameter electrodes are unable to record from individual neurons and cause more damage to brain tissue during insertion. If the electrodes are not insulated there will be signal loss due to stray capacitance and unwanted crosstalk between adjacent electrodes. To this end continuously conductive glass ensheathed microwires can be manufactured commercially through the Taylor-Ulitovsky method (Donald, 1987). Microwires are formed by casting metal into glass tubes and pulling both materials together while inductively heating at a temperature near the melting point of the glass. Extruding a glass-insulated metal wire in this way can reduce the diameter from millimeters to microns while conserving metal to glass diameter ratios. The large outer glass to inner metal diameter ratio gives the microwires thick insulation and low stray capacitance. These wires typically have inner metal cores ranging from 2-12 µm and outer diameters from 25-30 µm and are conductive over hundreds of meters (Badinter et al., 2010, Fig. 2.2).

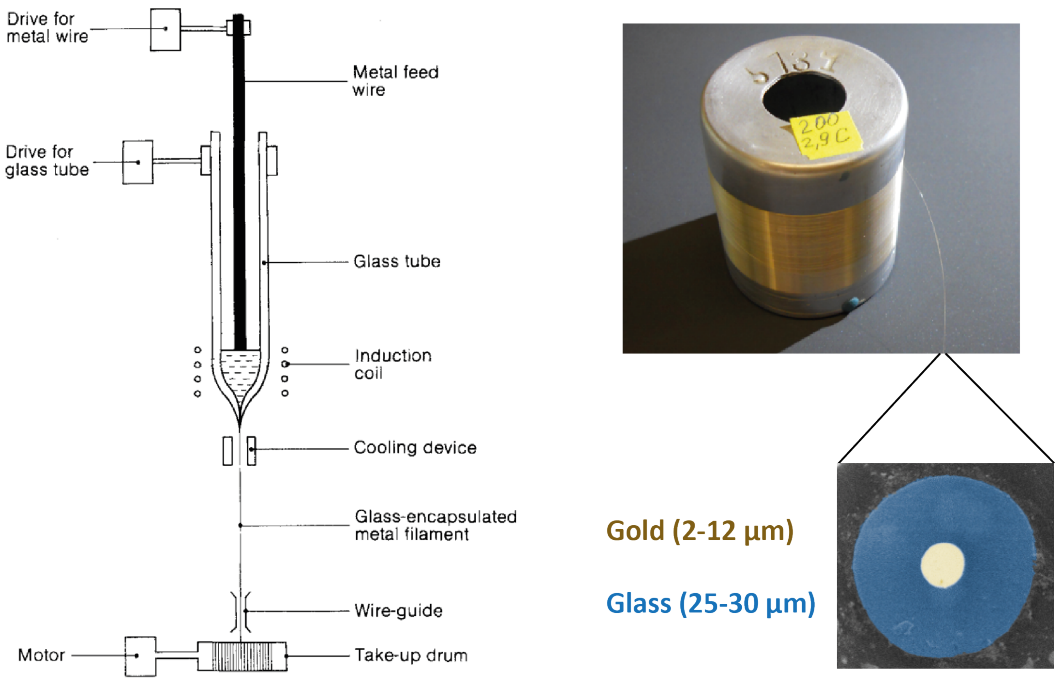

Figure 2.2: Glass ensheathed gold microwire fabrication. Continuously conductive glass ensheathed gold microwires are formed on a drawing tower by heating gold cast in a glass tube and pulling it with a motor (left). A single microwire thread hundreds of meters long is wrapped onto a spool (right). A false colored SEM micrograph shows the wire cross section.

Metal in glass wires have also been formed from a similar method, lithography assisted fiber drawing, which has the advantage of using lithographic techniques to deposit conductive cores from a variety of metals before drawing the wire to submicron core diameters (Gholipour et al., 2016). Hundreds to tens of thousands of microwires could be grouped into a bundle and pulled while heating to reduce its dimensions further and form a dense array (Badinter et al., 2010).

These glass ensheathed metal microwires have the properties of an ideal extracellular electrode. The microwires are available in a variety of inner metal to outer glass diameter ratios and can bend without breaking conductivity but are rigid enough to be inserted into brain tissue without a shuttle. They also have very low stray capacitance because glass is a good electrical insulator. Microwires could be formed into bundles of many wires with recording surfaces optimized for inserting into tissue and recording extracellular signals.

2.4 Design challenges

The main goal of this project is to develop a system to record neurons *in vivo* which has the potential to record from more neurons simultaneously than current technology permits. Bundle electrodes also have the potential to record from a larger tissue volume with an arbitrary distribution of recording sites. The scalability of the readout and electrodes provides a platform to compete with other large scale recording techniques. This thesis describes the methods and developments made toward the achievement of this goal by describing the journey to proof of principle experiments *in vivo.*

There are a number of challenges that need to be overcome before *in vivo* recordings can be performed. Bundle electrodes must be developed which can connect to the chip of the ROIC. These electrodes are required to insert into brain tissue while maintaining connectivity to individual indium bumps. The electrodes must also be electrochemically modified in order to lower the electrode impedance and increase the contact surface area. These and other challenges will be addressed by creating custom protocols to reproducibly fabricate electrode bundles (see 4.1).

Simultaneous to this, methods for connecting electrodes to the camera chip will be developed. These methods must electrically connect individual wires of a bundle to the indium bumps of the ROIC. The indium bumps are malleable and will need to be connected through the application of pressure. The density of the pixel array (pixel pitch can be $<$20 µm) also creates the risk that electrodes interconnect pixels to each other. Novel electrode designs and connection strategies must be devised to overcome these challenges (see 4.2). The design goals are to maximize the connectivity rate to the chip and to maintain the connection over the course of experiments without damaging the indium bumps.

To ensure that the system can record neural activity, the individual components of the system must be characterized. Experiments must be devised to measure the response of the readout to controlled voltage waveforms and to measure the electrical properties of electrodes (surface impedance, stray capacitance, etc.). The ultimate goal of these characterization experiments is to assess electrode connectivity and signal responses in an electrolyte bath stimulated with voltage waveforms as an *in vitro* model neural activity. These challenging measurements will be performed with custom equipment and novel experimental designs (see 4.3).

After overcoming the previous design challenges, the system can be used to measure neural activity in anaesthetized mice to demonstrate the performance of the system *in vivo* (see 4.4). Recorded waveforms (filtered to LFP and action potential bandwidths) will be analyzed and the recorded traces from the system will be compared with standard recording techniques (commercial amplifier with a compatible silicon probe). To confirm the biological nature of the recordings, the system can be tested in a behavioral paradigm, specifically the response to odor presentation in the olfactory bulb. Another challenge is to

assess the damage and insertion pattern of bundle electrodes with histology and imaging. The final goals in development are to increase the scale of recording density and to modify the bundles to ensure they separate in tissue.

There are trade-offs to consider with some important aspects of the design. The diameter ratio of inner conductive core to outer insulating glass of bundle electrodes is flexible. Larger electrode surfaces generally have lower impedances and record action potentials with higher signal to noise. However, they are more likely to record the overlapping activity of multiple neurons and displace larger tissue volumes during insertion. Also, the more wires that are fabricated into a bundle, the greater potential number of channels and tissue volume to record from, but the greater fabrication complexity and tissue damage caused. These and other design parameters will be balanced in the development of this extracellular recording technology.

3 Materials and methods

This section describes the technical details of methods required to perform all experiments and the subsections are ordered as they are written in subsequent results chapters.

Electrode fabrication (4.1)

ELIRI, S.A. was chosen as the supplier for glass ensheathed microwires due to their their ability to demonstrate wire conductivity over hundreds of meters and publications featuring wire bundle pulling. The materials used for the bundle electrode fabrication protocol are discussed in detail in section 4.1. The custom polishing tools were the final product of many versions prototyped with support engineers. The electrodeposition of iridium oxide was based on published formulations and advice from Dr. Stuart Cogan and adapted to bundle electrodes. Chemical solutions were provided by onsite scientific support staff.

Electrode to chip connection (4.2)

After researching the ROICs from a variety of infrared imaging chips, the Cheetah 640CL was chosen from Xenics due to its industry leading sampling rate of the chip at full frame resolution. Xenics was also willing to sell a Cheetah with the photodetector layer left out of the fabrication process and while keeping the package surrounding the chip accessible. The three armed electrode alignment setup (4.7) was constructed with micromanipulators used for *in vitro* electrophysiology rigs and designed with mechanical engineers. The strain gauge system which allowed for force feedback was a standalone circuit from RS and was modified to fit the three armed setup with the help of support engineers. Interconnect foils for reversible connection to the chip were purchased from Shin-Etsu as they were available in a variety of grid sizes and pitches which were similar to the pitch of the Cheetah camera and left no residue when pressed against the chip.

Electronic characterization (4.3)

The VSP-300 potentiostat was procured in order to perform sensitive electrochemistry on up to 6 channels simultaneously. The Ghost Lifter was developed to manipulate the voltage of the system around the electrode (Ringer's solution *in vitro* or an anaesthetized mouse *in vivo*) and was also used to stimulate individual camera pixels. The device was designed to perform these tasks while introducing the lowest possible noise, hence the name "ghost". The LCR device had been previously used in the lab to measure the stray capacitance of nanoelectrodes and was selected again to measure the capacitance of glass ensheathed microwire.

In vivo recordings (4.4)

Animal preparation procedures were based on surgery and anaesthesia techniques used for *in vivo* electrophysiology in the lab. The Tucker Davis recording system was provided by Dr. Ede Rancz and juxtacellular ulta-low impedance electrodes (jULIEs) were developed to integrate with the amplifier's headstage (discussed in section 4.1.4). The olfactometer was previously developed in the lab for odor discrimination tasks in awake mice and modified for usage with the camera setup. Histological and imaging protocols were established with onsite Scientific Technology Platforms.

3.1 Equipment

175 Multimeter	Fluke	USA
2 mm strain gauge	RS	UK
2245 Mini hot vac desiccator	Ted Pella, Inc.	USA
852-AA+ hot air rework station	C.I.F.	France
A16 Silicon probe	NeuroNexus	USA
Cheetah 640 CL camera	Xenics	Belgium
CompactStat potentiostat	Ivium Technologies	Netherlands
Core DVR system	IO Industries	Canada
Dissection light microscope	Leica	Germany
Heating pad	FST	USA
Interconnect foil	Shin-Etsu	Japan
LCR-821	GW Instek	Taiwan
MaiTai Deep See laser	Spectra Physics	USA
Manual sputter coater	Agar Scientific Ltd	UK
MetaServ 250 polisher with Vector head	Buehler	USA
Microm HM650V vibration microtome	Thermo Scientific	USA
Mini 25 micromanipulator	Luigs & Neumann	Germany
Micromanipulator	Scientifica	UK
Optima 1100 winding machine	Synthesis	India
Phenom Pro SEM	Phenom-World	Netherlands
Power 1401 DAQ	CED	UK
PZ2 Preamp with RA16AC Headstage	Tucker-Davis Technologies	USA
Raspberrry Pi Model-B with Camera V2	Raspberry Pi	UK
RH basic 2 hot plate	IKA	Germany
RZ2 BioAmp processor	Tucker-Davis Technologies	USA

SM7 control box	Luigs & Neumann	Germany
SP5 confocal microscope	Leica	Germany
Multiphoton VivoScope	Scientifica	UK
USB-6218 DAQ	National Instruments	USA
V7412 PCB strain gauge amplifier	RS	UK
VSP 300 potentiostat	Bio-Logic	France
Water immersion objective	Nikon	Japan
Xradia 510 Versa X-ray microscope	Zeiss	Germany

3.2 Chemicals and metals

Ag|AgCl|KCl/3.5M REF	Bioanayltical Systems	USA
Carbon nanopowder	Aldrich	USA
Conductive silver epoxy	Chemtronics	USA
Copper wire (100µm)	Alfa Aesar	USA
Crystalbond 509	Agar	USA
Crystalbond 509-S Stripper	Agar	USA
DAPI	Sigma	USA
Evans Blue	Sigma	USA
Gold wire (12.7 µm)	Alfa Aesar	USA
Indium	Aldrich	USA
Iridium (IV) chloride hydrate	Sigma-Aldrich	USA
Isoamyl acetate	Aldrich	USA
Mineral oil	Sigma	USA
Oxalic acid dihydrate	Sigma-Aldrich	USA
Paladur dental cement	Heraeus Kulzer GmbH	Germany
Platinum rod 0.5 mm counter electrode	Goodfellow	UK
Potassium carbonate	Sigma-Aldrich	USA
Potassium dicyanoaruate	Sigma	USA
Schnellfest 2 part epoxy resin	UHU	Germany
SP-DiO	Invitrogen	USA
Sulforhodamine 101	Sigma-Aldrich	USA
Tin	Aldrich	USA

3.3 Solutions and buffers

Ringer's solution used during *in vitro* experiments was composed of 135 mM NaCl, 5.4 mM KCl, 5 mM HEPES, 1 mM $MgCl_2$, 1.8 mM $CaCl_2$, pH 7.2, and 285 mOsm kg^{-1}. Phosphate-buffered saline (PBS) was composed of 182.5 mM NaCl, 3.4 mM KCl, 10.1 mM Na_2PO_4, and 1.8 mM KH_2PO_4 at pH 7.3.

3.4 Glass ensheathed microwires

Glass ensheathed gold microwires (ELIRI, S.A., Moldova) were provided as continuous threads of various lengths (50-500 m) on individual spools. Each spool had a distinct inner and outer diameter and % error.

3.5 Microwire polishing tools

Microwires were polished with custom manufactured aluminum holders (Fig. 3.1). These were designed to support embedded electrodes while attached to the Vector Head of a MetaServ 250 polisher. Inventor software was used to create the 3D designs.

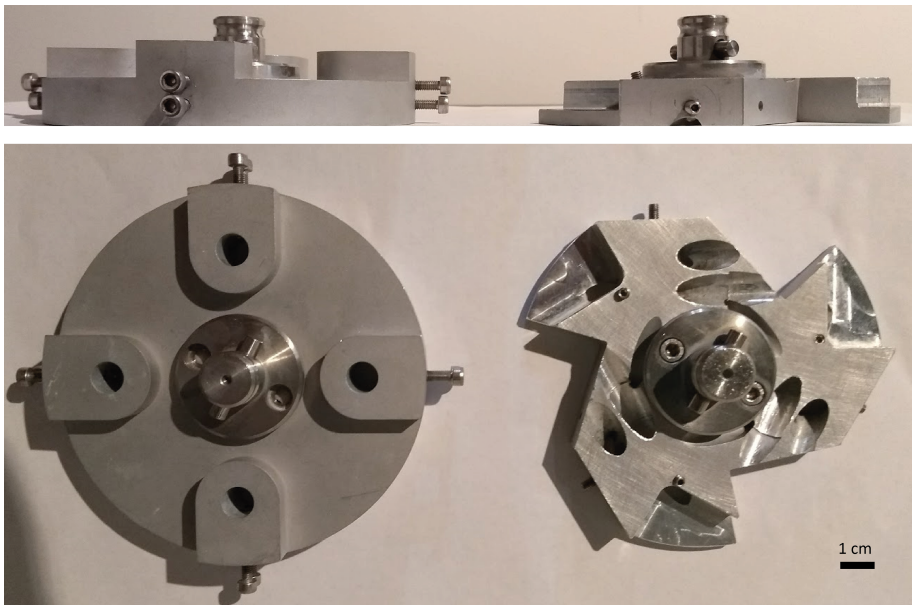

Figure 3.1: Custom polishing holders. Side and top views of flat and angle polishing holders fabricated from aluminum.

3.6 Preparation of iridium chloride electrolyte bath

The electrolyte bath for the electrodeposition of Iridium Oxide (IrOx) was based on a formulation reported by Meyer et al. 2001 and contained 10 gL^{-1} iridium (IV) chloride hydrate (99.9%, trace metal basis), 25.3 gL^{-1} oxalic acid dihydrate (reagent grade), and 13.32 gL^{-1} potassium carbonate (99.0%, BioXtra). Reagents were added sequentially to 50% of the solvent's volume first by dissolving $IrCl_4$ in the presence of oxalic acid followed by the addition of K_2CO_3 over a 16 hour period until a pH=12 was reached. The electrolyte was aged approximately 20 days at room temperature in normal light conditions until the solution reached a dark blue color.

3.7 Preparation of galinstan

Galinstan is a eutectic alloy that is liquid at room temperature and readily wets glass. Galinstan was prepared by mixing 70/20/10 by mass gallium/indium/tin in a covered ceramic crucible and heating on a hotplate at 125°C until the alloy became liquid.

3.8 Camera specifications

Recordings were performed with a Cheetah 640 CL infrared camera (Fig. 3.2). The photosensitive layer was omitted by the manufacturer, so the indium bumps at each pixel of the camera chip could be directly accessed. The ~10 µm pixels have a pitch of 20 µm in a 640x512 array. In the Cheetah CL camera, the input impedance of each amplifier is ~66 MOhm. The camera has a high and low gain mode. In the high gain mode used during recordings the feedback capacitance is 6.73 fF, sensitivity is 22.8 µV/electron, and the saturating charge is 75000 electrons with 192 electrons of noise (Neys et al., 2008). The reference voltage for the camera (virtual ground of the transimpedance amplifier of every pixel) was about 2.3 V. Other default adjustable camera settings are the 148 nA bias current and 50 µs integration time. The camera operated in integrate while read mode where the frame is integrated while the previous frame is readout through the camera link ports. Depending on the selected window of pixels, recordings took place at 1.7 kHz (full frame) to 200 kHz (smallest frame). The resolution of the camera's analog to digital converter is 14 bit. A Core DVR System was used to record data at up to 2 GB/s.

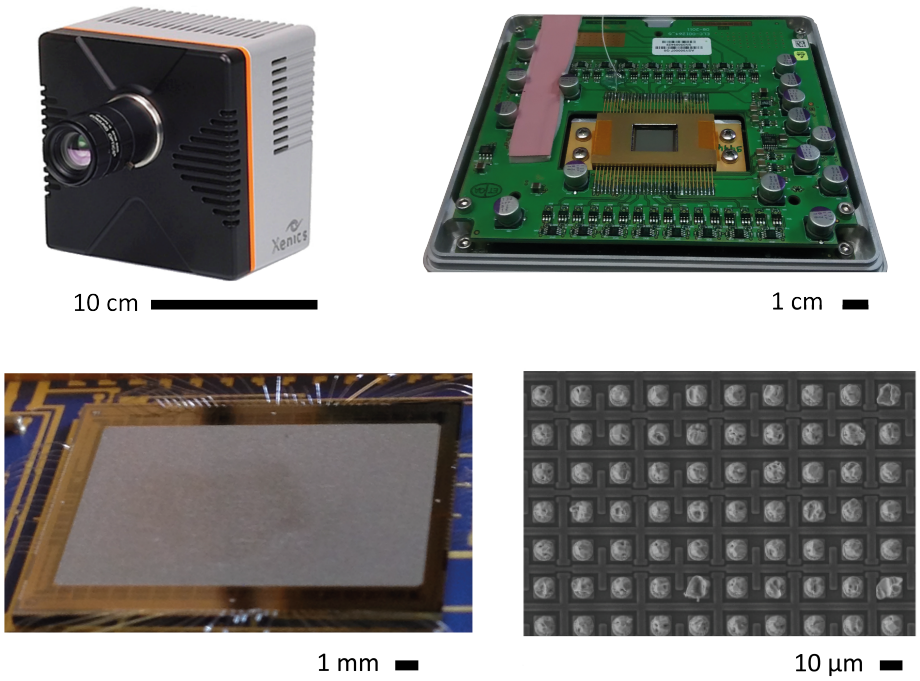

Figure 3.2: Cheetah Camera design. (From upper left to bottom right) The off the shelf camera with a lens, the readout circuit board underneath the lid, the open chip package with the photosensitive layer removed, and a SEM micrograph of individual indium bumps.

3.9 Camera stimulation

A 12.7 µm uninsulated gold wire was used to contact individual pixels for single pixel recordings. For these experiments, an optically isolated, low noise voltage source called the Ghost Lifter (Fig. 3.3) was developed to move the pixel within saturation limits of the amplifier by raising its voltage ~2.3 V above ground, then using fine voltage control, and then applying voltage waveforms. These functions were performed while adding minimal additional noise (hence "ghost"). The Ghost Lifter connected to one end of the wire through a soldered gold pin and the other freed end of the wire was pressed against the chip under the control of micromanipulators.

For *in vitro* stimulation experiments, a bundle electrode was connected to the chip via a freed wire connection (see 4.2.2), the camera was inverted, and a bath of Ringer's solution was raised until the tissue end of the electrode was immersed. The Ghost Lifter was used to lift the bath to the offset voltage of the circuit through a reference electrode and then apply a 1 mV square pulse or spike waveform.

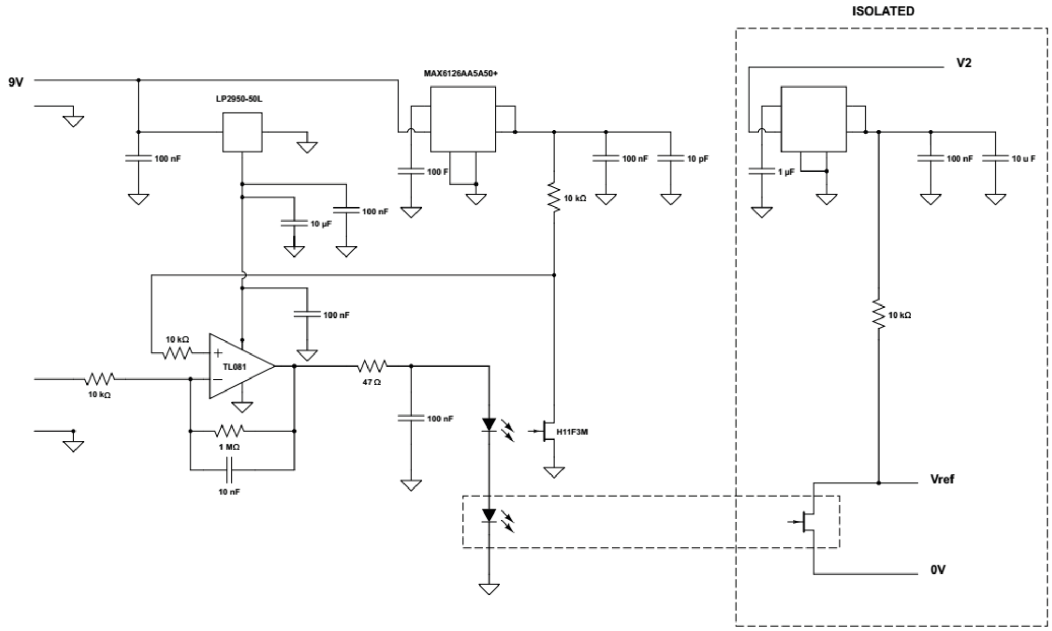

Figure 3.3: Ghost Lifter circuit. Note the diode opto-isolator.

3.10 Capacitance measurement

Resistance and stray capacitance of glass ensheathed microwires were measured with an LCR meter. A 3D printed chamber supported a microwire connected to 2 ports filled with conductive liquid galinstan (see 3.7 for preparation). The resistance across the 7.5 cm wire was measured with both ends of the wire connected to a galinstan port. An external electrode (copper wire) was immersed along with the connected microwire in PBS solution for various lengths measured with calipers and the capacitance at 100 kHz was measured from the external electrode (in grounded solution surrounding the microwire) to one of the galinstan ports.

3.11 Amplifier simulation

A simplified simulation of a single microwire connected to a capacitive feedback transimpedance amplifier (CTIA) was created with Circuitlab software. The operational amplifier open loop gain was 300, the output resistance was $5*10^{30}$ Ω, the input resistance was $1*10^{30}$, and the other component values are in Fig. 3.4. The simulated neuron was an ideal voltage source with a 1 kHz sine wave at 1 mV amplitude.

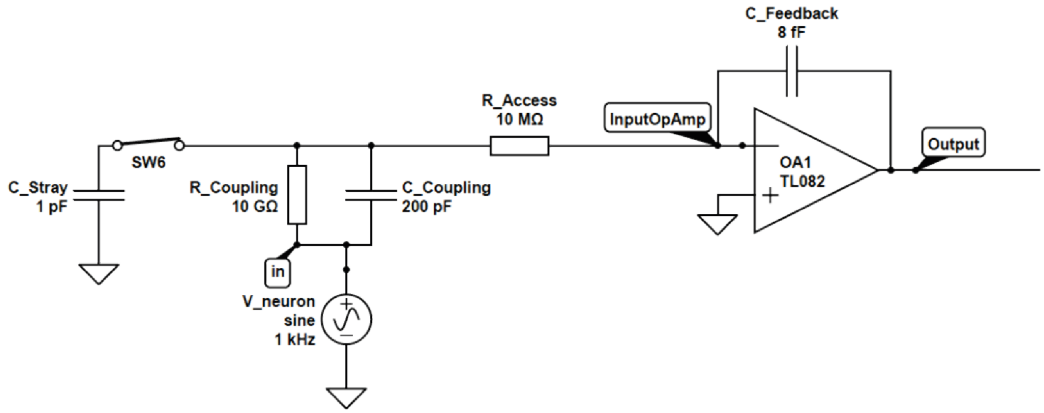

Figure 3.4: Simulation of microwire connected to a CTIA. The simulated neuron connects to the input of a capacitive feedback transimpedance amplifier across the electrode-electrolyte interface through a coupling resistance and capacitance and the access resistance of the electrode itself. This single electrode also has stray capacitance to ground.

3.12 Animal preparation

C57BL/6 mice aged 4-6 weeks were used in anesthetized recordings. To expose the olfactory bulb (OB), craniotomy surgeries were performed. For surgery, mice were anesthetized using ketamine (100 mg per kg of body weight) and xylazine (20 mg per kg for induction and 10 mg per kg for maintenance) administered intraperitoneally and supplemented as required. Body temperature was kept at 37°C with a feedback regulated heating pad. A custom made steel headplate was fixed to the parietal bone plates with dental cement. A 2x3 mm craniotomy was drilled over cortex. The chamber surrounding the craniotomy was filled with Ringer's solution to prevent it from drying out. Next a Ag|AgCl reference electrode was placed in the meniscus of Ringer's solution.

After surgery the anaesthetized mouse was brought directly to the camera setup and kept under anaesthesia with intraperitoneal supplementation of ketamine/xylazine as needed. The mouse was placed on a three axis manipulator mounted platform below the inverted camera setup with its respiration monitored by a piezoelectric sensor and body temperature maintained at 37°C with the same feedback heating pad. Using a small web camera and mirror, the bundle electrode was aligned over the craniotomy. The Ghost Lifter (Fig. 3.3) was connected to a reference electrode in the meniscus over the brain and the potential of the mouse brain was lifted to the reference voltage of the camera. Wire connectivity and noise were roughly assessed in the meniscus before insertion. For juxtacellular ultra-low impedance electrode (jULIE) recordings, the jULIE was connected to an amplifier headstage mounted perpendicularly to the mouse platform. The control pad for the micromanipulator was used to steadily insert the electrode aligned over the craniotomy. All

animal experiments were performed in accordance with the UK Home Office and Scientific Procedures Act.

3.13 Odor presentation

During anaesthetized recording, odor was presented with a custom airflow dilution olfactometer with valves controlled by a Raspberry Pi. Isoamyl acetate was presented with an inter-trial interval of 7 seconds. The olfactometer was washed by a strong stream of clean air between odor trials, while constant air flow to the animal was established by a final valve at the odor port to achieve a reproducible stimulus shape with minimal contamination.

3.14 Histology

After the craniotomy was performed, 0.2ml of 0.5% Evans Blue was injected intravenously into the tail vein. Insertion of the bundle electrode occurred within 30 minutes of the tail vein injection. Prior to the bundle insertion, the wires were dipped into SP-DiO, and allowed to dry. The bundle electrode was inserted 100 µm into somatosensory cortex. Immediately after the wire bundle was removed the mouse was perfused with ice cold 4% Paraformaldeyde (PFA), the brain was harvested and stored in 4% PFA overnight.

Using a vibratome, the brain was sliced into 100 µm horizontal sections. These sections were stored in 1x PBS during slicing. The slices were stained with DAPI using a 1:1000 DAPI:PBS wash for 10 minutes and were then transferred to fresh 1x PBS. Slices were mounted and coverslips were sealed. Imaging was completed on a confocal microscope.

For two-photon imaging of wire insertion, mice were anaesthetized using a mixture of Fentanyl/Midazolam/Medetomidine (0.05 mg per kg / 5 mg per kg / 0.5 mg per kg) and the skull overlaying the olfactory bulb was thinned using a dental drill and removed with forceps, and the dura was peeled back using fine forceps. Body temperature was maintained at 37 $^{\circ}$C throughout the experiment using a feedback regulated heating pad. Sulforhodamine 101 (100 µM final concentration) was injected intraperitoneally to label blood vessels. Animals were then moved to a two-photon microscope coupled with a laser tuned to 940 nm (~50 mW average power on the sample) for imaging. Images (512 x 512 pixels) were acquired with a resonant scanner at a frame rate of 30 Hz using a 16x 0.8 NA water-immersion objective. For in vivo z stack imaging, images were taken at a resolution of 512 x 512 pixels with 2 µm intervals. Wires were coated in DiO before insertion into the dorsal olfactory bulb using a micro manipulator. Images were analyzed post hoc using ImageJ software.

3.15 Micro-CT Imaging

After the craniotomy, a bundle was inserted into the brain with a micromanipulator. The mouse was then perfused with ice cold 4% PFA. The mouse was then decapitated and the whole head was glued with 2 part epoxy to the microscope specimen holder. The whole head was imaged with an X-ray microscope at 30kV (50.5 um pixels, 40 minute scan) and then the region of interest at the tissue end of the inserted bundle in higher resolution (3.98 um pixels, 10 hour scan). Imaris software was used to extract the features (bundle, skull and jaw bone, and the soft tissue) and color them.

3.16 Software

Circuitlab	Circuitlab	2017
Excel	Microsoft	2013
Illustrator	Adobe	2015
ImageJ	Bethesda	2016
Imaris	Bitplane	2016
Inventor	Autodesk	2016
Labview	National Instruments	2015
LyX	The LyX Team	2.2.2
MATLAB	Mathworks	R2016a
Mendeley Desktop	Mendeley	1.17.10
Origin	OriginLab	2017
Spike2	CED	7.10c
Word	Microsoft	2013

4 Results

These results will be discussed in the following chapters:

4.1 The challenges and design of bundle electrode and jULIE fabrication

4.2 The methods developed to connect bundle electrodes to the camera readout

4.3 Characterization of the bundle electrode's electrical properties and the readout's response to direct stimulation from a single wire and simulated neural activity applied to electrodes in a bath

4.4 The *in vivo* performance of jULIEs and bundle electrodes, an experiment where the camera readout records the response of an olfactory bulb neuron to odor presentation in an anaesthetized mouse, and imaging of the tissue damage caused by bundle electrodes

4.1 Electrode fabrication

4.1.1 Fabrication challenges

The electrode design is based on bundles of glass ensheathed gold microwires that are modified to connect to a camera chip readout and to insert into brain tissue. The main challenges with fabricating these scalable electrodes are to have smooth wire surfaces as an electrodeposition substrate, to electrically connect to the bundles to allow electrochemical functionalization, to seal the bundles to prevent liquid traveling from the electrolyte to the electronics, to modify the wires to ease tissue penetration, and to ensure that the wires separate from each other. These electrodes should be fabricated in groups in order to increase manufacturing throughput.

4.1.2 Bundle electrode fabrication development

During the development of the bundle electrode fabrication protocol, numerous strategies were attempted in order to overcome the fabrication challenges and reach a final protocol.

Polishing microwire surfaces

Electrode surfaces are generally polished or etched in order to create a reproducible substrate. Initial tests to hand polish bundles of a few tens of embedded microwires with fiber optic polishing paper was fairly reproducible but was low throughput, required minutes to polish each electrode, and was victim to the instability of the human grip. A light microscopy target surfacing system could polish electrode surfaces more quickly but it could only modify one electrode at a time and it was difficult to obtain a micron scale surface finish. Ion beam polishing was attempted as a method to polish bundles without the need for embedding. However, it took tens of hours to mill through an entire bundle and after polishing, conductive residue remained on the surface of the outer glass which effectively increased the electrode surface area in an uncontrolled manner. Surface etching had the difficulty of maintaining a flat or controlled metal surface when scaled up to wire bundles. Automated polishing machines for geological surface processing were tested and allowed for smooth wire cores on the micron scale.

To polish bundle electrodes the embedding material surrounding the bundle electrodes needed to be hard enough to polish, not change volume as it solidified, and to dissolve without damaging the microwires or support tubes. A variety of embedding materials were used that were too difficult to completely remove (dental cement, cyanoacrylate) even with potent organic solvents. Any residue present after solvent attack could cause wires to adhere to each other and created the risk of obscuring the recording sites. Other embedding materials were not hard enough for polishing (frozen wax, ice) or significantly changed volume as they hardened (nail polish, cyanoacrylate, Crystalbond diluted with

solvents to increase viscosity). Hard dissolvable polymers exist but these are generally solidified with high pressure injection molds. Any type of mold requiring applied pressure would misalign wires and potentially break the insulating outer glass. Crystalbond 509 was the best suited removable embedding material for bundle electrodes that I tested as it is viscous in its molten state and is readily removed with a matched solvent or acetone.

Electrically connecting bundles

The bundle electrodes needed to be electrically contacted in order to electrochemically modify the polished surfaces of individual wires. It proved simplest to try and connect all wires together and modify all wire surfaces at once. Silver epoxy is often used to connect circuit components without soldering. For electrically connecting bundles, direct application of silver epoxy had low connectivity rates because of its relatively large feature size. The liquid metal galinstan is able to electrically connect individual wires, but was unable to wet more than a few tens of electrodes at once. This led to experimenting with embedding and polishing to expose the cores of the microwires and then coating all of the cores with a thin layer of metal via sputtering. With all of the cores shorted together with low resistance, the sputtered surface created a large contact for electrical connection.

Sealing bundles

Due to capillary action, liquid travels easily through the gaps between wires in a bundle electrode. At some point along its length the gaps must be sealed so that liquid does not damage the readout electronics. Paladur dental cement completely surrounds microwires during embedding but when a thin band around the center of the bundle electrode was exposed to solvent (to remove embedding after polishing), the integrity of the seal was lost. Cyanoacrylate could seal bundles but spread uncontrollably along the length of the bundle during application which led to the risk of permanently sealing either end of the electrode. 2 part epoxy could be applied in a controlled manner at a specific point on the bundle electrode, solidified in minutes at room temperature, and resisted most solvents.

Tissue penetration

The end of the bundle to be inserted into brain tissue needed to be prepared to minimize tissue damage and to ensure wires separate from each other. If microwires remain adhered to each other they will not spread apart to record from a larger population of neurons and will potentially cause a greater foreign body response. The glass ensheathed microwires are flexible and their stiffness during insertion will depend on their freed length and how tightly they are packed. The polishing angle of the tissue end was modified in order to minimize the area of contact of each wire during initial tissue penetration. Novel bundle arrangements were prototyped (twisting the bundles, splitting the end into multiple sub-bundles) but these formations over-complicated the time consuming fabrication protocol.

Final Protocol

The final fabrication protocol (displayed in Fig. 4.1) used the following techniques to meet the requirements of fabrication. To expose the gold cores of wires and to give them a smooth morphology, a semi-automated polisher was used to polish the bundles after they were embedded. There are two electrodeposition steps in the fabrication procedure: the first to deposit gold bumps on the chip end of the electrodes to increase the contact surface area of each microwire, and the second to deposit the low impedance thin film iridium oxide (IrOx) on the tissue end of the electrode. To electrically connect to the tissue end while electrodepositing gold on the chip end, the wires were embedded in dental cement and polished, sputtered with gold to electrically short the wires together, and the sputter was contacted to a macroscopic wire with silver epoxy. To electrically connect to the chip end while electrodepositing IrOx on the tissue end, the already deposited gold bumps were pressed into a reversible carbon paste connector. To seal the bundle electrodes, 2 part epoxy was applied to the bundle before embedding. In tests salt solution could not travel through bundles sealed in this way. To improve the ability of the microwires to insert into tissue the bundles were angle polished to 30° creating a needle like shape. To ensure the wires separate from each other after embedding in Crystalbond 509 (CB), the embedding was removed overnight with a matched solvent solution (CB 509 stripper).

4.1.3 Bundle electrode fabrication

Bundle electrode fabrication was performed in these sequential steps (see simplified schematic in Fig. 4.1):

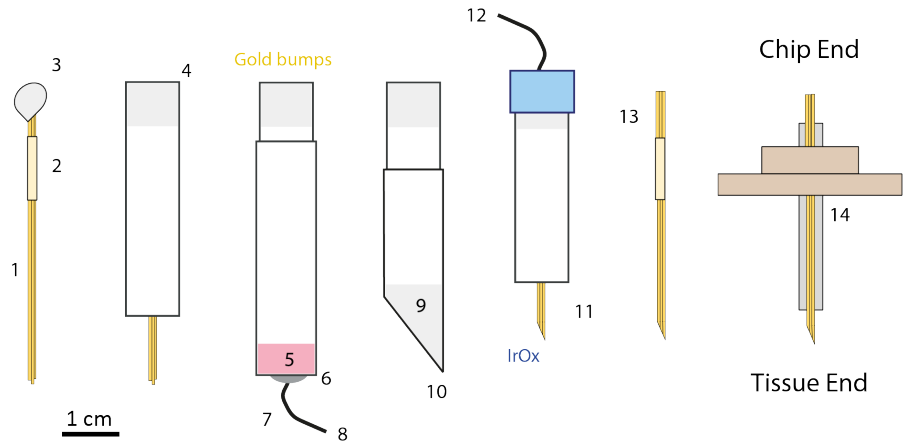

Figure 4.1: Schematic of bundle electrode fabrication. Glass ensheathed gold microwires (gold), epoxy seal (yellow), Crystalbond 509 (light grey), polypropylene tube (white), dental cement (pink), macroscopic wire (black), carbon paste filled connector (blue), polystyrene shank (dark grey), PEEK holder (beige). The numbers correspond to the fabrication steps in the text below.

1. Bundles were created by wrapping microwire from spools with a modified winding machine, tying them together with 100 µm copper wire, and cutting with a razor so that there were 4 bundles, each with a total length of ~5 cm.

2. The bundle electrodes were then sealed by applying 2 part epoxy resin on both sides of the bundle with a cuvette stirrer creating a ~5 mm band 1.5 cm from the chip end. The seal was allowed to harden for 10 minutes.

3. CB 509 polymer was heated to 126°C in a metal crucible within a hot plate desiccator and then pumped to 0.9 bar for 10 minutes to remove bubbles from the molten CB. The chip end of each electrode was dipped in molten CB 20 times, removed from the crucible, and hung up for a few minutes to harden. The bundles were centered within a polypropylene tube (2 mL syringe) and the chip end was back filled with molten CB by pouring from a ladle to fuse it within the tube.

4. The chip end was polished flat by fixing the supporting tube in a custom polishing holder (see 3.1). This holder was designed to fit the pneumatically powered head of the polishing machine and could support up to 4 electrodes simultaneously. The electrodes were first balanced manually, semi-automatically polished at 18 µm grit, then re-aligned and polished on 5 and 0.5 µm grit slurries. The electrode face was then washed with distilled water and inspected with a dissection microscope.

5. The tissue end was embedded in dental cement by filling the end of another polypropylene tube supported in a mold with freshly mixed liquid. The cement was allowed 10 minutes to harden.

6. The cement embedded tissue end was flat polished with the same procedure as step 4.

7. The embedded polished wires at the tissue end were electrically connected by sputtering gold for 170 seconds. Next an insulated macroscopic wire was connected to the sputtered surface with conductive silver epoxy which was allowed to harden overnight. The silver epoxy was then coated with 2 part epoxy to insulate and mechanically support the macroscopic wire.

8. Gold bumps were electrodeposited on the chip end to increase the contact surface area of each wire (see 4.1.6).

9. ~1 cm of the tissue end was cut off with a hot scalpel blade. The tissue end was embedded in CB (as in step 3), but was supported in a polypropylene tube cut at a 30° angle

10. The tissue end was polished again (as in step 4), but with a custom polishing holder which held electrodes at a 30° angle (see 3.1).

11. The tissue end was freed from its CB embedding by removing the CB with a solvent stripper. Near complete removal of CB residue was achieved after immersing in 150 mL of stirred stripper for at least 16 hours with the stripper replaced at 3 different intervals. The freed end was then washed in distilled water. The final freed and separated angle polished wires can be seen in Fig. 4.2.

12. Iridium oxide (IrOx) was electrodeposited on the tissue end (see 4.1.6). To electrically connect to the chip end, the embedded gold bumps were pressed into a tightly fitting connector filled with a paste of carbon powder and mineral oil. This created a reversible connection with contact resistance of 100s of Ω per wire.

13. The chip end was freed from its CB embedding and the carbon paste was washed off with CB stripper as in step 11.

14. The double functionalized electrode bundle freed from embedding was then mounted to a flat length of polystyrene (end of cuvette stirrer) with 2 part epoxy. ~5 mm of the tissue end was left freed on both sides of the bundle electrode. The freed length on the tissue end determined the maximum insertion depth. The polystyrene shank was then mounted with 2 part epoxy to to a polyether ether ketone (PEEK) plastic holder fit for the camera alignment setup.

This procedure produced electrodes for free wire connection method (see 4.2.2). For the connection method of applying force against an interconnect foil (see 4.2.1), the chip end was embedded within the PEEK holder by filling a custom polytetrafluoroethylene (PTFE) mold with dental cement.

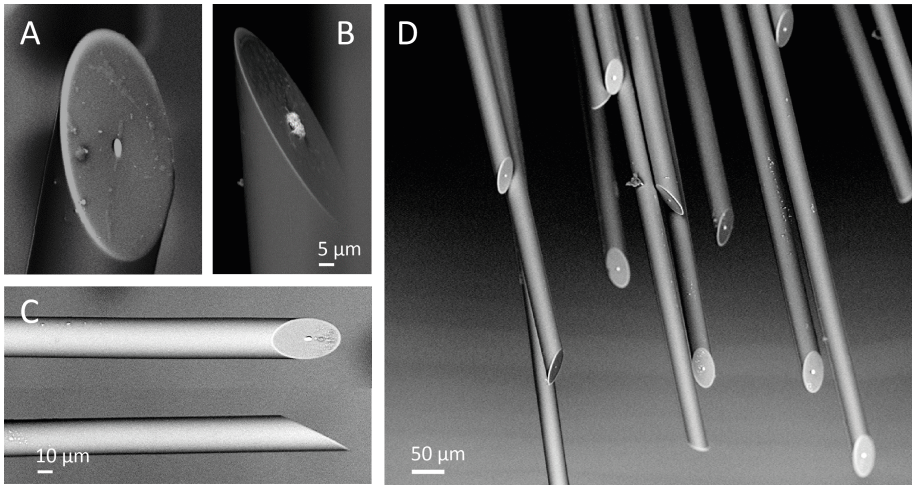

Figure 4.2: Freed angle polished microwires. **(A)** The 30° angle polished surface of a single wire. **(B)** Electrodeposited gold bump on the polished gold surface. **(C)** Front and side view of polished wires. **(D)** Group of freed angle polished wires within a bundle after removal of CB embedding.

4.1.4 jULIE electrode development

We modified the design of bundle electrodes to allow for reversible connection to a standard amplifier headstage and for controlled electrochemical functionalization. A Mill-Max connector for a headstage formed the basis of a 16 channel probe. Glass ensheathed microwires were most reliably electrically contacted by breaking them into pools of liquid galinstan. This method was used to connect each microwire to an individual pin (channel) in the Mill-Max connector. 2 part epoxy was applied over the top of the Mill-Max connector to mechanically support these connections and to insulate the wires. The tissue end of these electrodes consisted of a polystyrene shank which supported the 16 epoxied wires with the freed length of the wires protruding beyond the edge of the shank. We referred to these as Juxtacellular Ultra-low Impedance Electrodes (jULIEs).

4.1.5 jULIE electrode fabrication

jULIEs had a standardized fabrication procedure as follows:

1. Bundles of a few hundred microwires 5 cm in length were CB embedded in a polypropylene tube cut to 30° angle, angle polished with a custom polishing head,

and freed from their embedding in CB stripper (as in step 10 and 11 in bundle electrode fabrication).

2. A polystyrene shank was attached to an 18 pin Mill-Max connector and 16 pins were filled with galinstan using a needle (the remaining 2 channels are for a reference electrode connection).

3. 16 angle polished microwires were chosen, formed into a bundle, and held against the polystyrene shank. The individual unpolished ends were bent into the drop of galinstan in each pin under a dissection microscope with tweezers. While immersed in galinstan, the end of the microwire was broken with a needle to ensure the core was wetted.

4. The freed length of the angle polished bundle over the polystyrene (necessary to reach the target brain region) was measured and the wires and 16 pins were insulated with 2 part epoxy (see Fig. 4.3).

5. After drying for at least 20 minutes the freed wires were immersed in PBS and connected to a potentiostat as the working electrode in a 3 electrode cell to assess connectivity of individual channels and measure the impedance at 1 kHz.

6. The jULIE was immersed in electrolyte and connected to a potentiostat for electrodeposition of gold on all channels (see gold bumps in Fig. 4.2B), then immersed in PBS to measure impedance of each individual channel, then in electrolyte for a second electrodeposition of IrOx on all channels (see 4.1.6), and a final impedance measurement of each channel in PBS.

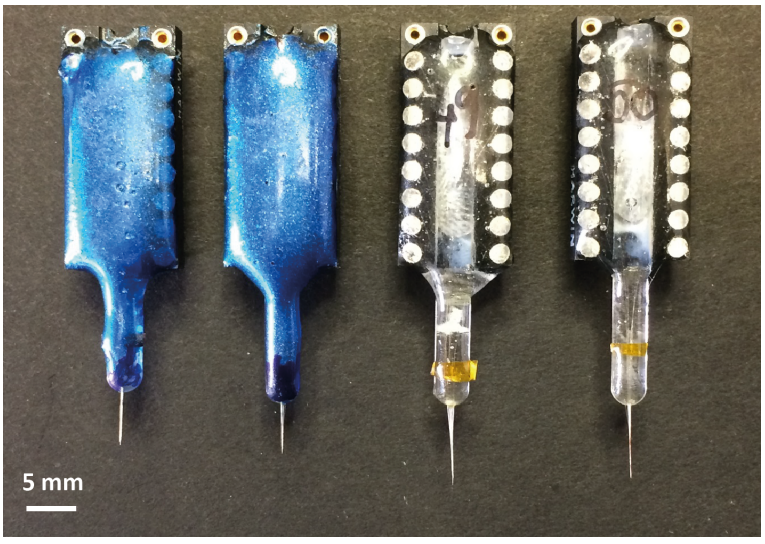

Figure 4.3: Fabricated jULIEs. Completed 16 channel jULIEs with 5 and 10 mm freed length.

4.1.6 Electrodeposition

By immersing the exposed metal core of gold microwires in electrolyte solution and applying voltage, a redox reaction can be performed which causes the formation of a thin film on the conductive surface. Electrodeposition of gold was performed to increase the surface area of the electrical contact on the chip end of bundle electrodes. Hemispherical gold bumps were electrodeposited onto polished bundles from an electrolyte bath containing 10 gL^{-1} $KAu(CN)_2$ (99%) based on a formulation reported by Elias et al., 2012. The three electrode cell setup comprised of a bundle electrode as the working electrode (WE), a platinum rod as the counter electrode, and a Ag|AgCl reference electrode (REF). A potentiostat (Ivium) was used to perform a potentiostatic deposition protocol (-1 V vs REF for 25 s) in a stirred solution heated to 60 °C in a chemical hood. After deposition the bumps were washed with distilled water and visually inspected under a dissection light microscope. See the morphology of a gold bump imaged with SEM in Fig. 4.5B.

The second usage of electrodeposition was to decrease the impedance of the recording sites at the tissue end of the electrode. A multichannel potentiostat (Bio-Logic) was used for the electrodeposition of IrOx, with an identical 3 electrode cell immersed in an iridium chloride electrolyte bath (see 3.6 for electrolyte preparation). The IrOx electrodeposition protocol consists of two stages: CV and pulsed potentiostatic. Between the two stages the WE is kept at the open circuit voltage of the 3 electrode system for 180 s to allow Ir^{+4} concentration to equilibrate both in the deposited solid-state film and liquid diffusion layer. During CV deposition the WE potential is swept between -0.5 and 0.6 V vs REF at a rate of 1 Vs^{-1}(Fig. 4.4); during pulsed potentiostatic deposition the WE potential is pulsed between 0.8 V and 0 V for 1 second 350 times. Obtained deposit morphologies were characterized by SEM. The morphology of electrodeposited IrOx with SEM is shown in Fig. 4.5C.

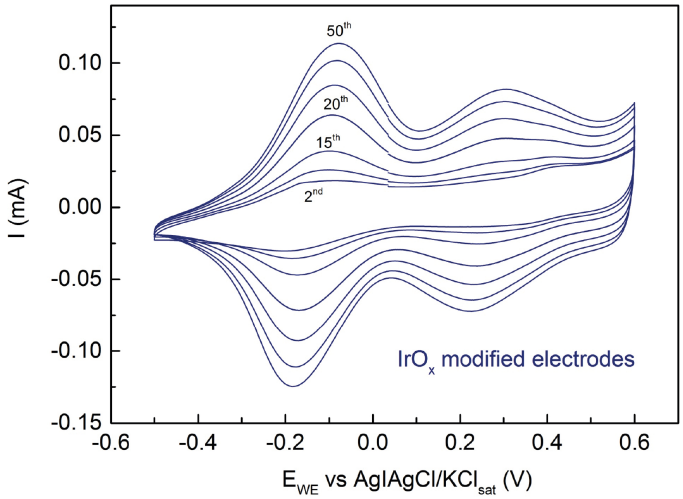

Figure 4.4: Electrodeposition of gold and IrOx. Cyclic voltammogram in iridium chloride electrolyte showing redox peaks at up to 50 cycles for a polished embedded bundle of 330 microwires with 6µm core diameter.

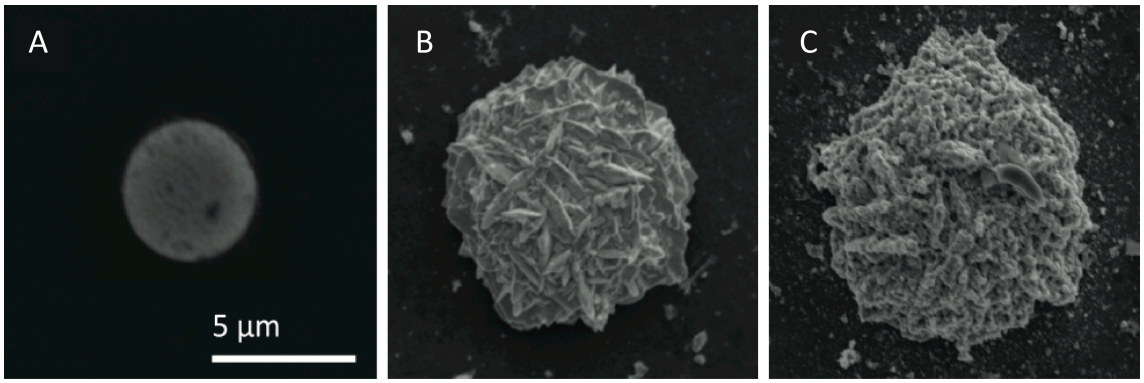

Figure 4.5: Morphology of electrodeposits. **(A)** SEM of bare polished surface of gold microwire. **(B)** SEM of nanostructured gold on the gold microwire. **(C)** SEM of IrOx on the electrodeposited gold.

4.1.7 Conclusion

I overcame numerous fabrication challenges in the development of bundle electrodes. With this fabrication protocol, a batch of 4 bundle electrodes could be produced over the course of about 2 days. There is room to improve the standardization and scale of these bundle electrodes (see 5.5). Next strategies were developed to connect bundle electrodes to the camera readout electronics. 16 channel jULIEs were also developed as a smaller scale electrode which could directly connect functionalized microwires to a specific amplifier headstage and off the shelf extracellular recording system.

4.2 Electrode to chip connection

4.2.1 Anisotropically conductive interconnect foil

Bundle electrodes were connected to the exposed indium bumps of the camera chip to conduct the signal to the camera circuit. The first method to connect to the indium bumps was with an anisotropically conductive silicon interconnect foil. These flexible interconnect foils are designed for the semiconductor industry for reversible connection of circuit components (Yamazaki, 1995). The interconnects are silicon rubber integrated with a grid of gold plated metal wires which allow force dependent low resistance connection (Fig. 4.6A). A 2 mm strain gauge amplified with a PCB circuit connected to a USB DAQ was attached to a steel arm mounted on a micromanipulator to measure calibrated force. When the manipulator pressed the arm down against a scale, it applied perpendicular force which caused the arm and strain gauge to bend. There was a clear linear relationship between the applied force and the output voltage of the strain gauge circuit (Fig. 4.6B). This arm was used to test the pressure required to connect through the interconnect foil by pressing an embedded bundle of 30 polished microwires against the interconnect onto a flat piece of copper while monitoring the resistance from the microwires (electrically connected through gold sputter) to the copper with an ohmmeter. The interconnect allowed the bundles to connect with low resistance in most cases after 0.3 N/mm^2 of pressure was applied (Fig. 4.6C).

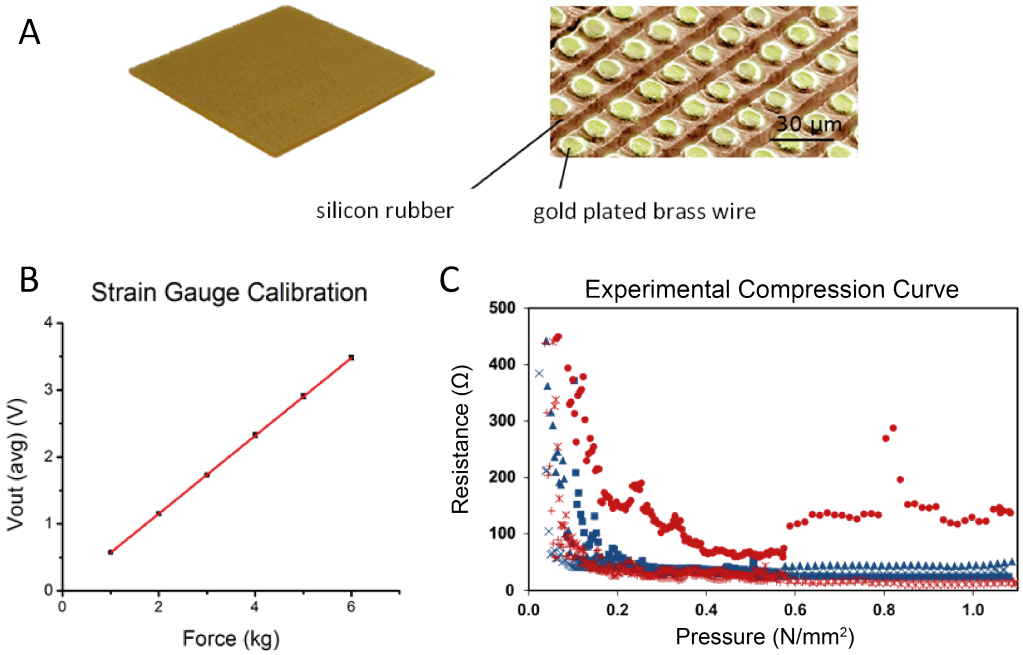

Figure 4.6: Compression of the interconnect foil. **(A)** The interconnect foil consists of silicon rubber with a grid of gold plated metal wires. **(B)** Calibration of strain gauge circuit showing linear output of the strain gauge amplifier in response to force applied against a scale. **(C)** Raw compression curves of two different 30 wire bundles (red, n=3, blue, n=3) on an interconnect foil measured with the calibrated strain gauge circuit and an ohmmeter.

To connect an electrode to the camera chip, the camera was first moved with manual manipulators under an interconnect foil held with suction from a hot air rework station and then the foil was gently dropped over the desired region of the chip. A three-armed setup mounted to micromanipulators which held the electrode in a magnetically supported platform (Fig. 4.7) was used to align the electrode against the foil while measuring applied force on each arm through the use of custom Labview software. After the electrode was aligned by balancing the force on each arm, the arms moved together in micron steps to apply pressure while the output of the camera and applied force was monitored. Connectivity thus depended on a contact from the exposed gold wire of the electrode to a wire within the foil and a contact from that wire in the foil to an indium bump.

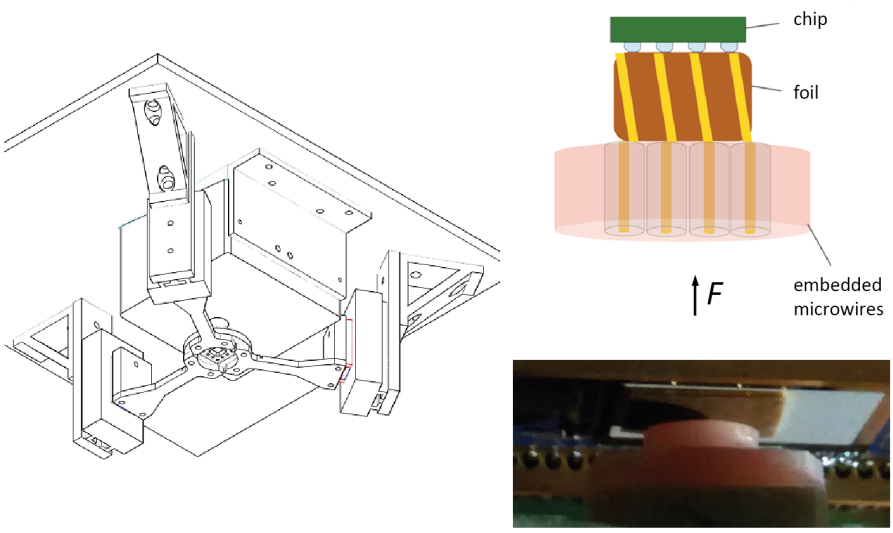

Figure 4.7: Pressure dependent chip connection. A three-armed setup, which moved with micromanipulators and strain gauge force feedback, was used to align the electrode against the interconnect foil on top of the chip and apply the necessary force for connection.

This connection technique places a barrier over the delicate indium bumps, but the applied force can ultimately flatten bumps, interconnect them, or break them off of the underlying metal (Fig. 4.8). The connectivity rate is also hindered by the necessity of an interconnect wire to be connected to both a bundle electrode microwire and an indium bump. The specific size and pitch of the wires in the interconnect foil thus determine the maximum connectivity.

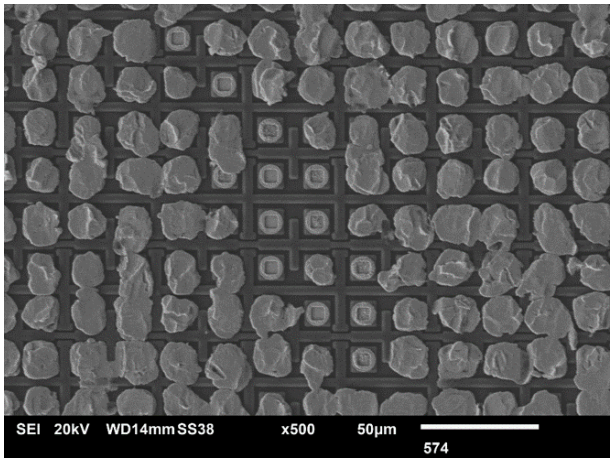

Figure 4.8: Damaged indium bumps. Indium bumps on the chip that have been deformed or removed after repeated application of force from an electrode onto an interconnect.

4.2.2 Freed wire connection

To connect while applying minimal force, an alternate connection technique was developed where un-embedded bundles were directly pressed to the chip. Using the same three-armed setup, the chip end of a bundle could be grossly aligned over the chip and lowered onto the indium bumps causing the individual microwires to buckle under the applied force (Fig. 4.9). The chip end of these electrodes (detailed fabrication in section 4.1.3) were bumped with gold (see 4.1.6) to increase the contact surface area of each wire. Connected pixels were found by sweeping the voltage through pixel saturation limits with the Ghost Lifter (see 3.3) while the tissue end was immersed in the meniscus above the animal's craniotomy. Extensive connection rate data was not collected, but ~10% of wires in a bundle connected to a pixel and fell within the saturation limits of the connected amplifier. This technique minimized damage to the indium bumps as the pixels remained active after pressing and lifting off the freed wires at the chip end of the electrode.

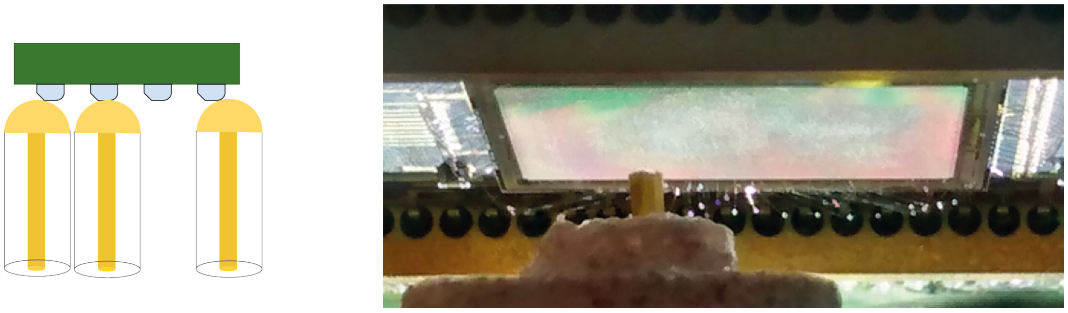

Figure 4.9: Freed wire connection. The chip end of a bundle electrode aligning over the camera chip. The wires are not embedded so they are free to buckle on contact.

4.2.3 Hard interconnect

Another way to protect the malleable indium bumps would be to bond a stronger interconnect to the chip surface which could withstand multiple connections to electrodes. A hard interconnect was designed which could semi-permanently bond to the chip. Thousands of wires were packed into a glass tube and fused together with a custom inductive heater to create an array of embedded gold wires (Fig. 4.10). Pilot attempts were made to cut a section of this fused bundle and polish it. However, it proved extremely difficult to keep both sides of the hard interconnect perfectly parallel while polishing and to perfectly align the interconnect while mounting it to the chip.

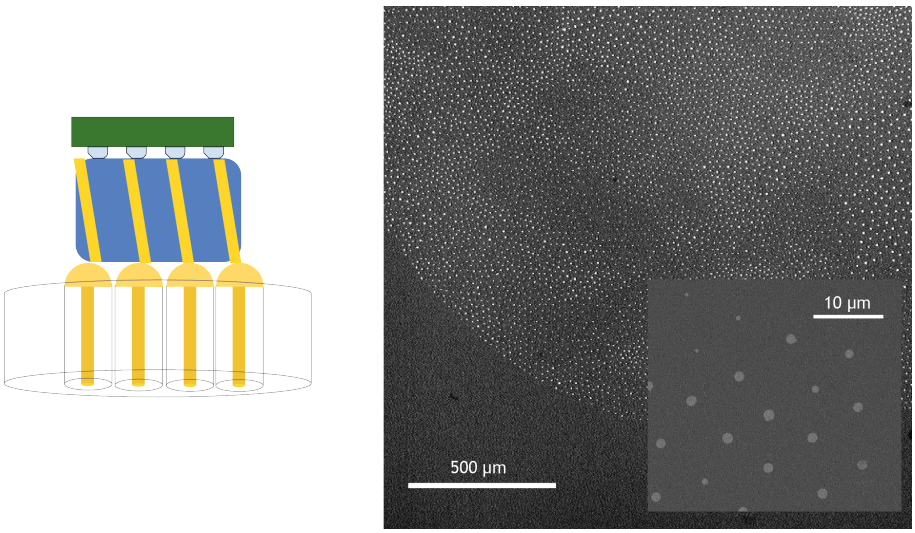

Figure 4.10: Hard Interconnect. SEM of hard interconnect after fusing wires and flat polishing.

4.2.4 Conclusion

A variety of methods were developed to connect electrode bundles to the camera chip readout. An anisotropically conductive interconnect foil could connect embedded bundle electrodes in a pressure dependent matter. When this pressure damaged the indium bumps on the chip surface, a method with less applied force was developed where freed wires with gold bumps to increase their surface area were pressed against the indium bumps. An alternate method was to bond a hard interconnect to the indium bumps once and then reversibly contact bundle electrodes to the face of the interconnect, however these hard interconnects had practical difficulties hindering fabrication. Also, In the future a ROIC chip could be modified to leave out indium altogether and have less malleable contacts (see 5.3). This may significantly increase the connection rate of bundle electrodes to the chip which currently limits the number of active recording sites during *in vivo* experiments. For the methods described in this chapter, the freed wire connection strategy was best suited for connecting electrodes for pilot *in vivo* experiments.

4.3 Electronic characterization

4.3.1 Introduction

After methods were developed to connect electrodes to the chip, the electronic readout of the system could be characterized. The electrical properties of the system were measured to determine under what conditions neuronal signals can be recorded and the amplitude limits of the signal. There are 4 major components in this system: the capacitive feedback transimpedance amplifier (CTIA) of each pixel, the electrode, the connection of the electrode to the input of the amplifier, and the electrode-electrolyte interface (EEI) of the electrode to the extracellular solution in the brain.

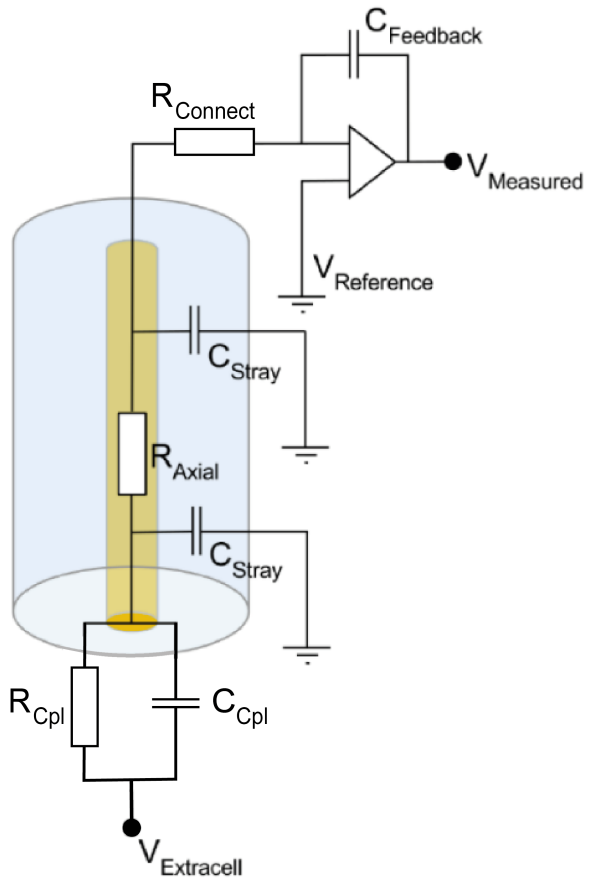

Figure 4.11: Equivalent circuit of the recording system. A single glass insulated gold wire within a bundle electrode is connected to the input of a CTIA within the infrared camera's readout integrated circuit. 'Cpl' represents 'coupling' to the electrolyte.

The potential field in the extracellular space ($V_{Extracell}$) is sensed by the recording surface of the electrode resulting in a voltage difference in the conductive core in comparison to a

reference electrode (Fig. 4.11). The recording surface of the electrode has an associated coupling impedance which has resistive (R_{Cpl}) and capacitive components (C_{Cpl}) in parallel. Higher electrode impedance electrodes have a lower signal to noise ratio and thus electrodes are often functionalized to lower their impedance (Cogan, 2008). When a wire within a bundle electrode connects to a camera pixel, the signal passes across the connection resistance ($R_{connect}$) to the input of the amplifier. The stray capacitance (C_{stray}) along the electrode length depends on the thickness of the insulating glass layer. The greater the stray capacitance, the greater the signal loss along the electrode length. In the more complicated configuration where there are many wires within a bundle electrode, there is also signal crosstalk due to the capacitive coupling of neighboring conductors in space. CTIAs are often used in infrared imaging detectors to convert small photocurrents from light sources into low noise voltage outputs (Kozlowski, 1996). In this system, the CTIA behind each pixel (op amp in Fig. 4.11) acts to convert extracellular voltage from a neuronal current source to an output trace. This output trace relates to an absolute voltage but is given the arbitrary units of pixel values (PV) within the saturation limits of the amplifier. Though our system has a unique design, these electrode properties (electrode impedance, stray capacitance, etc) are characteristic of all recording electrodes.

4.3.2 Single pixel analysis

A single uninsulated gold microwire was contacted to the pixels of the camera in order to measure the response to simulated signals. This wire was connected to a custom device known as the Ghost Lifter (see 3.3) which lifted the voltage of the wire to the reference voltage of the camera and allowed for the application of stimulation waveforms. These functions were performed while adding minimal additional noise (hence “ghost”).

The uninsulated wire was connected to a pixel and the Ghost Lifter applied square pulses to the microwire (see 3.9) and the recorded traces in PV were exported for analysis. The noise of a recording was calculated as the standard deviation of a recorded trace converted from PV to µV using the ratio of the signal amplitude (in µV) to the recorded amplitude (in PV). 21 different pixel contacts to the camera with a 500 µV square pulse stimulation recorded an average amplitude of 842 pixel values (SD 269 pixel values) with a noise of 61.6 µV (SD 29.6 µV).

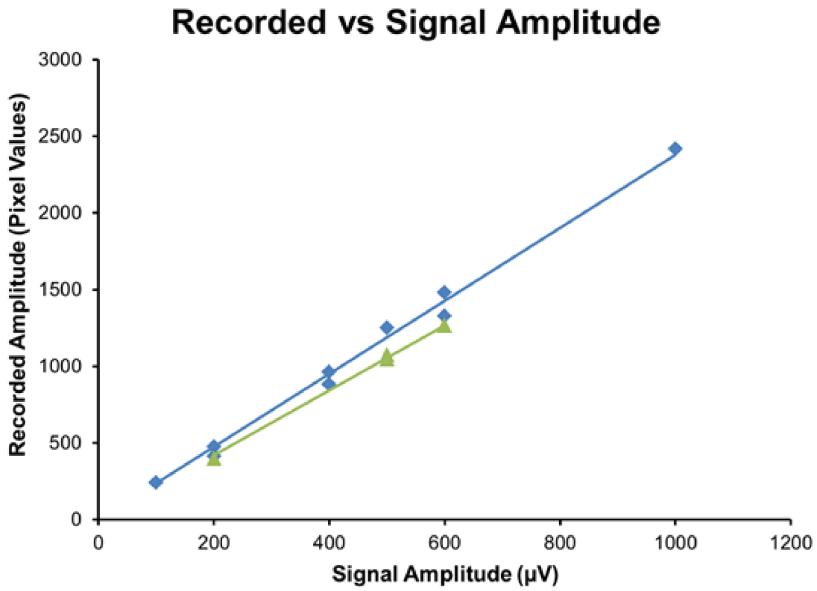

Figure 4.12: Single pixel voltage response. Recorded amplitude in pixel values (PV) of injected square pulses of variable amplitudes to a single pixel in 2 different trials. The trendlines confirm a linear relationship between recorded and signal amplitude (both R^2 >0.99).

Fig. 4.12 demonstrates the recorded amplitude increased linearly with input signal amplitude. These recording properties allowed 300 µV simulated spikes to easily be resolved over the baseline noise. The responses were stable over the timescale of the short recordings (seconds) but the stability over greater timescales was not recorded. Similar linear relationships between the input and output were obtained in other pixel recordings, however the cascade of signal amplitudes with uniform camera settings was only recorded twice.

The response to 500 µV square pulses was recorded in 21 unique pixel connections (Fig. 4.13). The recorded noise of each trace was ~60µV except for 2 outliers with more than double the noise of other connections. This noise is significantly larger than the intrinsic noise of the camera (1.28 µV noise for a 500 µV signal). The negative correlation between noise and amplitude (linear fit, R^2= 0.524) suggests the general trend that larger amplitude responses to the same signal have lower noise.

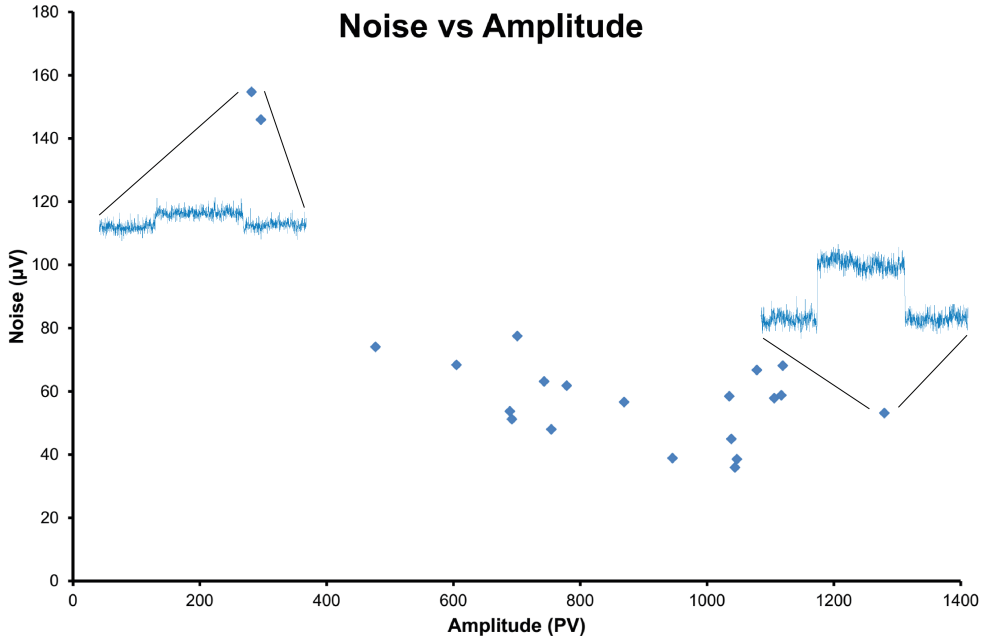

Figure 4.13: Single pixel recording noise. Distribution of the noise in response to a 500 µV square pulse at various signal amplitudes. Each point is a unique contact to a pixel. Raw traces of the highest and lowest amplitude responses are overlayed and positioned with their corresponding data point.

The gain of each pixel is relatively uniform, however the connection of the gold wire to the indium bump (surface area, contact pressure, etc) is different in each trial. Therefore the variation in the noise of each pixel contact is likely due to the quality of connection. It is possible that the outliers are part of a non-linear increase in noise at low recorded amplitudes, however these high noise responses were difficult to consistently record.

4.3.3 Electrical properties

Glass ensheathed microwires are manufactured by casting gold into glass tubes and pulling both materials together while inductively heating at a temperature near the melting point of the glass (see 2.3). It is not clear whether the gold and glass maintain their bulk properties after being fabricated into microwires, so the electrical properties of microwires were tested. Resistance and stray capacitance of microwires were measured with an LCR meter (see 3.10). The recorded experimental resistances included the contact resistance of the probes to the galinstan ports and the galinstan to the severed end of the microwire as well as the axial resistance of the microwire. Theoretical axial resistance was calculated from the equation below where R is resistance, ρ is resistivity, l is length, and A is area :

$$R = \frac{\rho l}{A}$$

The ρ resistivity value used for gold was 2.44x10^{-8} Ωm (Serway, 1998). The resistance across the wire decreased proportionally with core area of the microwire ($\propto$ diameter^{-2}) (Fig. 4.14).

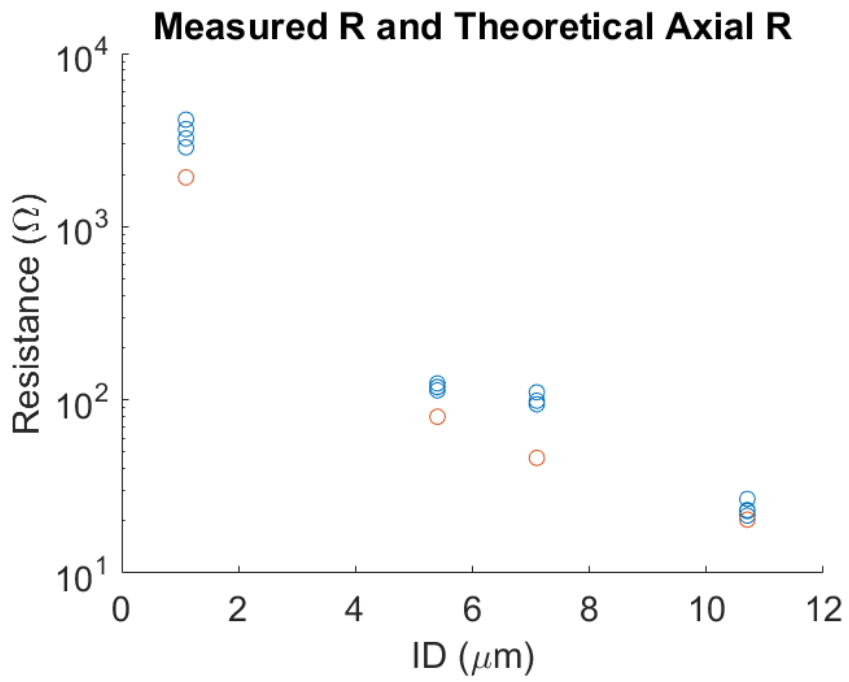

Figure 4.14: Resistance across microwire of different inner diameters. The experimental recordings across a 7.5 cm length of microwire (blue) and the theoretical axial resistance for the same wire dimensions (red) .

Stray capacitance increased linearly with the immersed length of microwire for microwires of all diameters (Fig. 4.15). This demonstrates that the diameters were uniform along entire wire lengths for all microwires tested as jumps in diameter ratio across mm of wire would result in fluctuations in recorded stray capacitance.

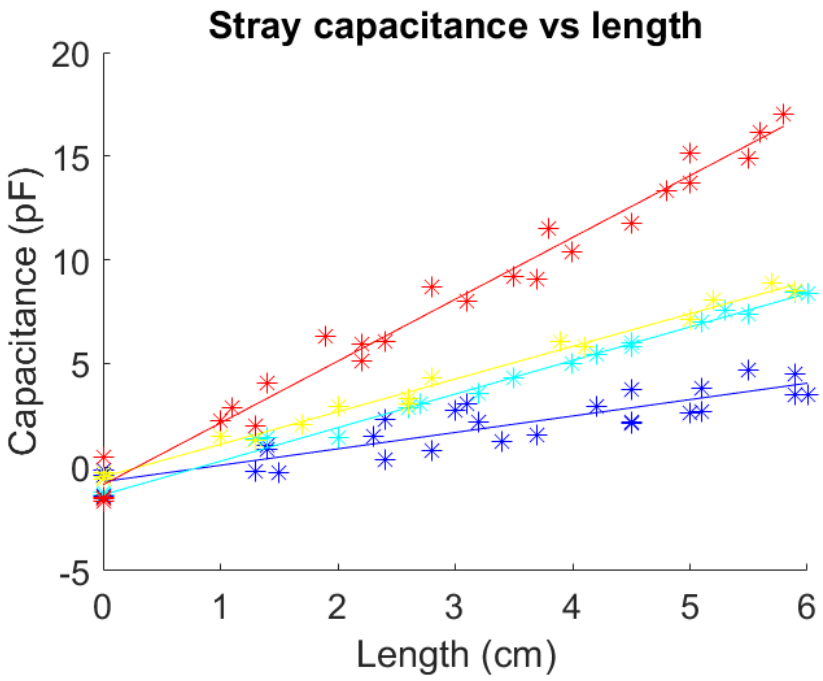

Figure 4.15: Stray Capacitance of glass insulated gold microwire. Inner/outer diameter (µm): 10.7/26.6 (red), 7.1/30.1 (yellow), 5.4/27.4 (cyan), and 1.1/28.3 (blue).

The relative permittivity of the glass surrounding the gold core of the wire could be calculated using the experimental values for stray capacitance from the following equation for capacitance of a coaxial cable where C is capacitance, ε_0 is the electric constant, $\varepsilon_r$is relative permittivity, l is length, OD is outer diameter, and ID is inner diameter:

$$C = \frac{2\pi\varepsilon_0\varepsilon_r l}{ln(\frac{OD}{ID})}$$

By plotting both sides of the capacitance of a coaxial cable equation against each other using the values for experimental capacitance, the ε_r of glass could be determined from the slope of this plot to check the accuracy of the capacitance recordings (Fig. 4.16). The linear slope was 4.76 (R^2= 0.971). This value is very close to the relative permittivity of glass from the literature - 4.8 (Van Hippel, 1944). This verifies the ability of the LCR meter to record the stray capacitance of glass ensheathed microwires and demonstrates that the glass behaves as bulk after being heated and pulled into a microwire.

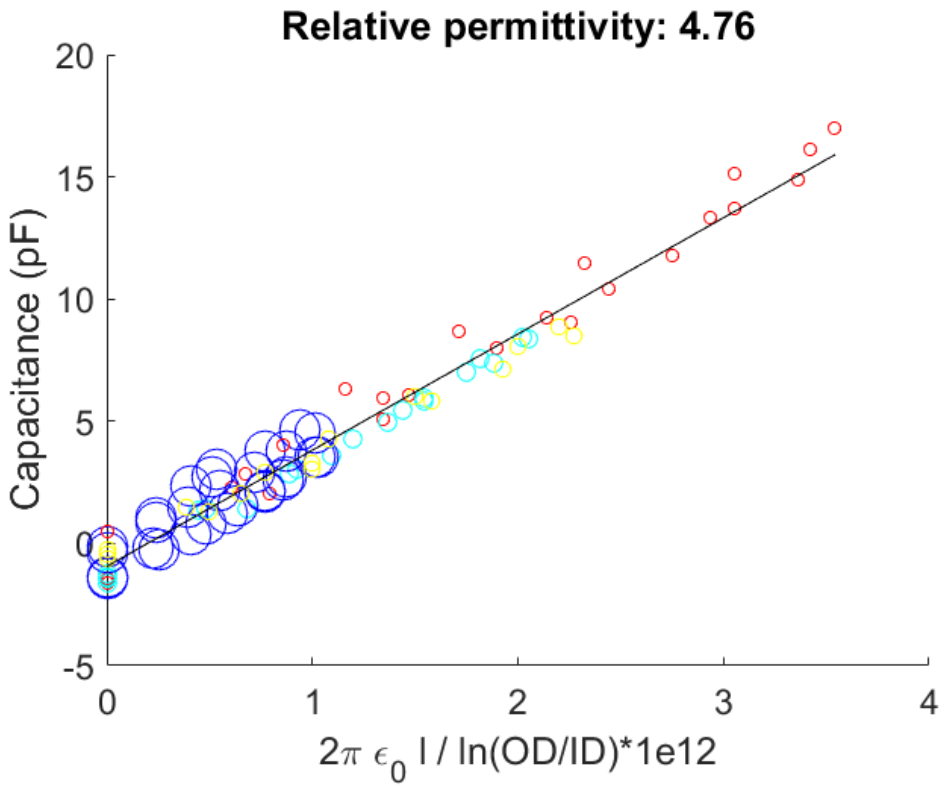

Figure 4.16: Experimental relative permittivity of glass. Relative permittivity of outer glass (ε_r) calculated from capacitance of a coaxial cable equation. Different diameter ratios are color coded as in previous figure and the marker size is determined by the outer to inner diameter ratio.

The coupling impedances (|Z|) of the recording surface of electrodes were recorded with a potentiostat in a 3 electrode cell filled with PBS. The impedance of un-embedded 1.9 µm wires (in the configuration of a jULIE, see 4.3) was recorded after angle polishing, after gold electrodeposition, and after Iridium Oxide (IrOx) electrodeposition over the electrodeposited gold (4.1.6). The mean impedance value for polished wires was 21.63 MΩ for polished wires, 3.87 MΩ for gold, and 0.10 MΩ for iridium oxide on gold (Fig. 4.17). In addition to the 200-fold decrease in impedance over subsequent depositions, there is also a decrease in impedance variance.

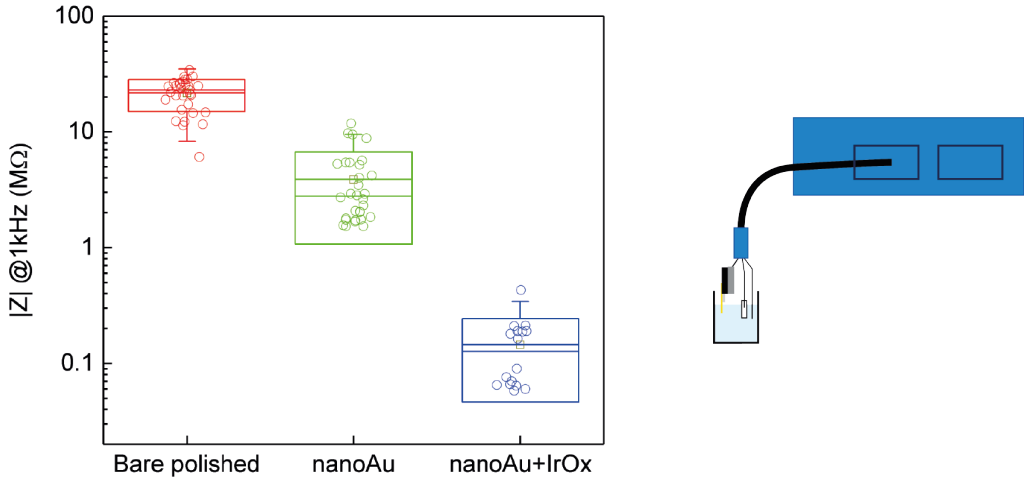

Figure 4.17: Impedance of electrodeposited surfaces. jULIEs with freed, angle polished, 1.9 µm wires were immersed in PBS and the impedance was recorded with a potentiostat for a bare surface after angle polishing, after a gold bump (nanoAu) was electrodeposited, and after IrOx was deposited on the nanoAu. The impedance at 1 kHz is displayed in a box plot, each point signifying an individual channel and the whiskers are 2 SD from the mean. The line with a square marker is the mean.

After measuring the stray capacitance and impedance of the wires, their effect on the output of the camera readout electronics was simulated (see 3.11). Earlier impedance results suggest typical coupling capacitances are >300 pF (calculated from Fig. 4.17, nanoAu+IrOx impedance at 1 kHz of ~400 kΩ using the equation $C = \frac{1}{2\pi Z f}$) and stray capacitance for the length of a bundle electrode of ~5 pF (estimated from Fig. 4.15, depending on the glass to gold diameter ratio). There would be additional stray capacitance due to crosstalk with neighboring wires, but even in the worst case scenario where the outer glass of wires are in direct contact with each other, the total capacitance would only double due to crosstalk. So 10 pF total of stray capacitance (red in Fig. 4.18) is a conservative estimate. From Fig. 4.18 it can be seen that for a coupling capacitance of 300 pF there is little effect on the amplifier output if the stray capacitance increases from 1-10 pF and for the expected stray capacitance (~10 pF), increasing the coupling capacitance further (by lowering the coupling impedance) should not increase the output voltage or input current of the amplifier.

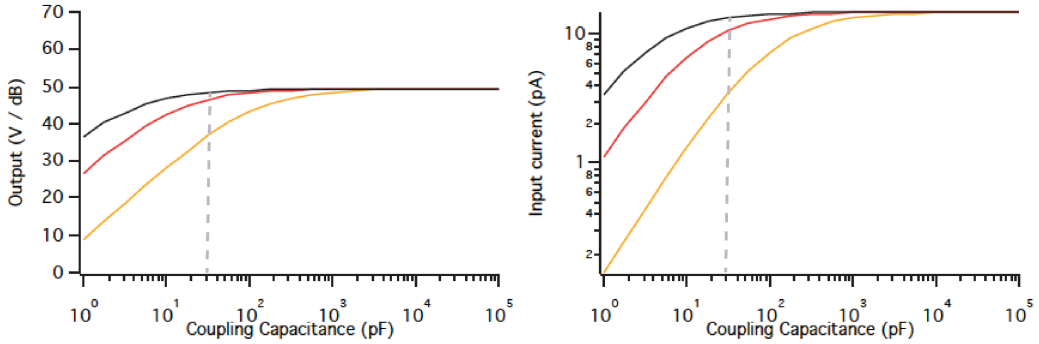

Figure 4.18: Simulated effect of stray capacitance on op amp output. Each line is a different stray capacitance: 1 pF (black), 10 pF (red), 100 pF (orange). Dotted grey line represents 300 pF.

4.3.4 Voltage injection response *in vitro*

To acquire experimental measurements with expected neuronal signals, a bundle electrode of 100 microwires was connected to the chip via a freed wire connection (see 4.2.2), immersed in a bath, and potential pulses were applied to the bath (Fig. 4.19A, also see 3.9).

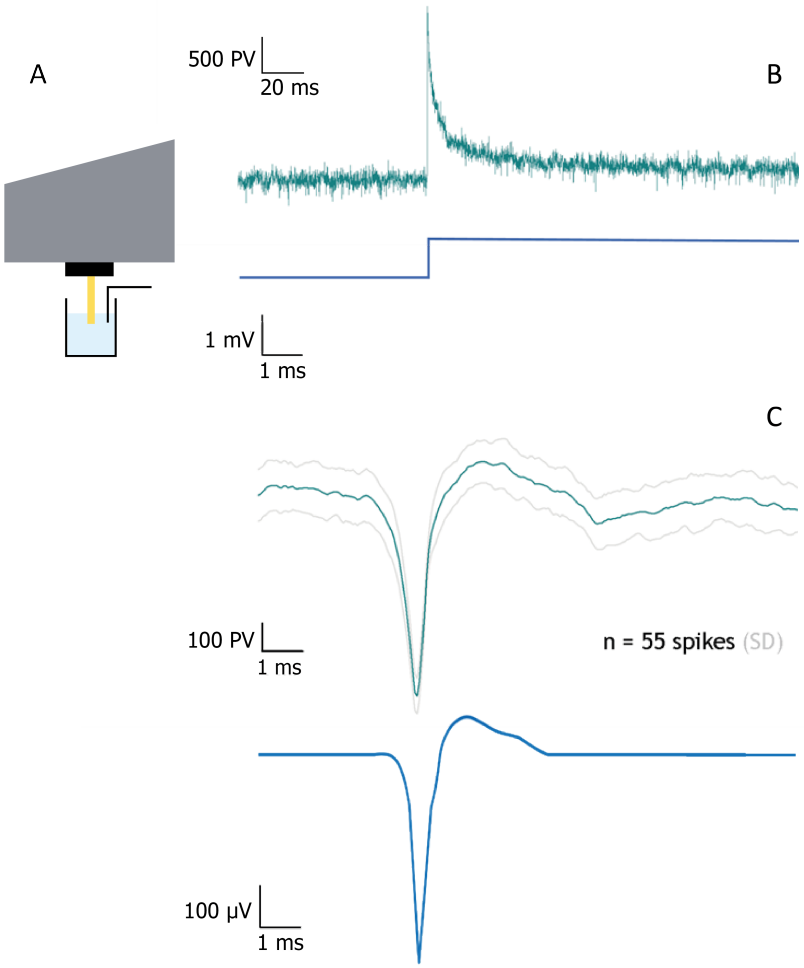

Figure 4.19: Voltage injection *in vitro*. **(A)** *in vitro* bath clamp setup with a bundle electrode (100 wires, 11.1 µm inner gold, 28 µm outer glass, only functionalized with IrOx) connected to the camera with freed wires and an injection electrode immersed in solution. **(B)** Response in pixel values (PV) to injecting 1 mV square pulse (blue trace). **(C)** Response to injecting 500 µV spike-like waveforms (blue trace) displayed as an average trace (green) of 55 spikes in sequence with 1 standard deviation from the mean in grey.

The response to an injected square pulse is displayed in Fig. 4.19B. The decay of the trace is due to the capacitive charging of the electrodeposited IrOx, the time constant of which would depend on the impedance. The response to injected spike-like waveforms (Fig. 4.19C) demonstrates that in a strongly connected pixel, spikes of a realistic physiological amplitude can be easily resolved without filtering.

4.3.5 Conclusion

The combination of these results demonstrates that this recording system has the capability to record real neuronal signals. The average response in pixel values to a 500 µV signal was 842 PV with 61.6 µV noise. The experimental recordings of microwire stray capacitance and axial resistance confirmed the expected theoretical values. The impedance at 1kHz decreased more than 20 times for these electrodes with electrodeposition of gold and subsequent IrOx. The injection of simulated spikes *in vitro* demonstrated that simulated neuronal signals could be resolved with high signal to noise. These results gave me confidence in transitioning to *in vivo* experiments to record real neuronal activity with this system.

The intrinsic noise of the camera is only 0.24% of the signal in high gain mode (see 3.9). The recorded noise is much higher than this which could be attributed to the large resistance from the recording site to the pixel and unshielded electrical interference. To further improve the signal to noise ratio, the connection strength to the pixels will likely need to be increased (see connection methods in 4.2). However, increasing the coupling capacitance of the electrode interface further should not significantly increase recorded amplitude because the coupling capacitance is large compared to the capacitance for the rest of the system (stray capacitance and input capacitance of the amplifier). The connection resistance could be better estimated by connecting large resistors in series with a connected wire. The order of magnitude of the unknown connection resistance could be determined by recording with a constant input signal while increasing the resistance in series. Additionally, the crosstalk capacitance between microwires in a bundle could be measured experimentally if an effective system could be designed to support electrically connected microwires an exact distance from each other. Due to the flexibility of the microwires, this is practically very difficult. Though the signal to noise of this system can improve, it is enough to record simulated spikes and thus experiments progressed to *in vivo* recording.

4.4 *In vivo* Recordings

The *in vivo* recordings are divided into two distinct parts: microwire electrodes with a conventional readout (4.4.1) and bundle electrodes connected to the camera readout (4.4.2).

4.4.1 jULIEs

The efficacy of functionalized microwires to record neuronal signals *in vivo* could be directly assessed with juxtacellular ultra-low impedance electrodes (jULIEs). These jULIEs were used in combination with a conventional amplifier system used for extracellular recording (Tucker-Davis Technologies). The mouse olfactory bulb (OB) is an ideal brain region for testing these electrodes because of its superficial location, known laminar structure, and the neural activity underlying olfactory sensory processing can be studied with standard odor presentation techniques. These electrodes had 16 channels with 1.9 µm diameter recording sites and were electrochemically functionalized (for fabrication see 4.1.5) and inserted into the OB of anaesthetized mice. Clear spikes were recorded over 1 mV in amplitude (Fig. 4.20). In recordings from 17 unique jULIE channels, the average mean amplitude of spikes was 828 µV (SD 276 µV).

The jULIE was lowered at a constant rate of 5 µm/s up to 2.6 mm deep while the insertion depth from the micromanipulator was simultaneously recorded. The amplitude vs vertical displacement plot shows a rising and falling in spiking amplitude as the electrode travels ~30 µm in the brain. This peak in amplitude is presumably as the electrode passes a cell soma (see extracellular waveform vs. position in Fig. 1.1B). The variance in recorded amplitudes is likely due to the varying distance between the electrode track and the soma of neurons as well as the activity of those neurons.

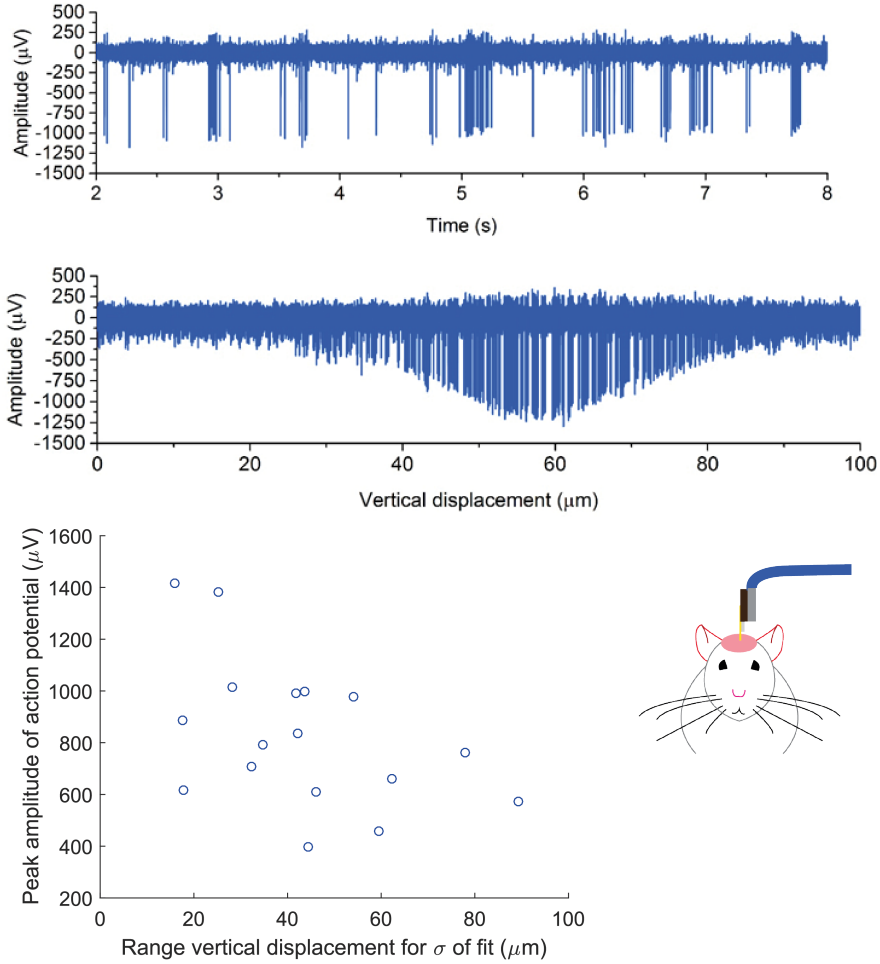

Figure 4.20: jULIE recording *in vivo*. Recorded spikes in the mouse OB from a single 1.9 µm jULIE channel (500-6kHz bandpass filter) (Top). Extracellular amplitude vs vertical displacement of the electrode as it was inserted into the OB (middle). Peak amplitude vs vertical displacement for σ (1 SD) of the Gaussian fit of from all amplitude vs vertical displacement trials (n = 17).

To measure the spatial extent that units can be detected, Gaussian (normal) distributions were fit to the amplitude vs vertical displacement plots. For these fits the range of vertical displacement was calculated for the σ value (1 SD) and plotted against peak action potential amplitude (as the distance from the electrode to the neuron is unknown). There is high variability in this plot, but the largest peak amplitudes tend to occur when the electrode detects a rise in recorded amplitude over shorter distances (because the recording site is closer to the active part of the neuron). The small recording site area (< 4 µm^2) and high spike amplitudes suggest that most of these recordings are of single units.

By connecting individual channels of a jULIE to a potentiostat as the working electrode in a 3 electrode system (with platinum counter and Ag|AgCl reference electrodes) in the meniscus above the brain, the impedance of each channel could be recorded through EIS. There was minimal change in impedance at 1 kHz (|Z|) when measured in the meniscus over the craniotomy (mean impedance was 2.33 MΩ), on the surface of the olfactory bulb (mean: 1.88 MΩ), and after inserting 1300 µm deep (mean: 1.95 MΩ) (Fig. 4.21). This suggests that the functionalized interface did not sustain damage during insertion (no delaminating of gold and/or IrOx) and in acute measurements may have had minimal encapsulation from a foreign body response. The 4 higher impedance channels could be due to a high resistance connection to the galinstan port or delamination of the iridium oxide prior to the experiment.

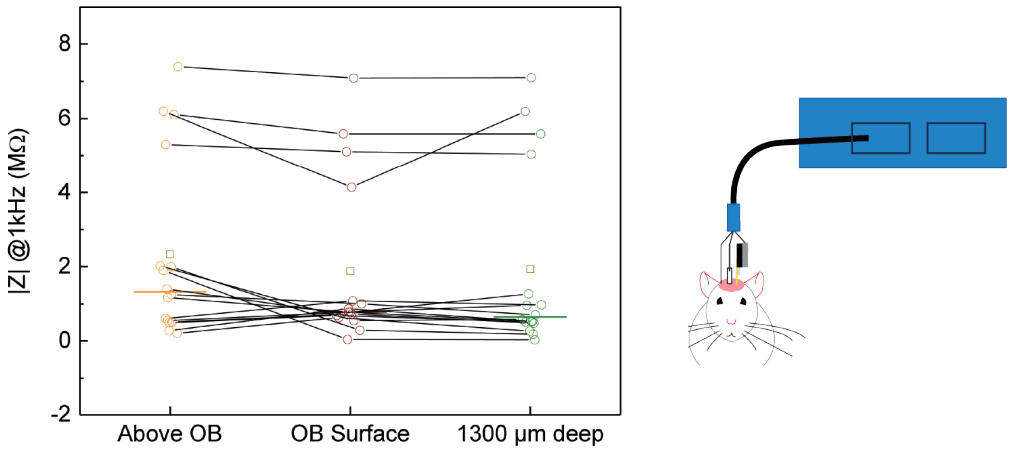

Figure 4.21: Impedance *in vivo*. The impedance at 1 kHz of jULIE channels *in vivo* is displayed with lines connecting the channels. Each point signifies an individual channel, the horizontal line is the median, and the square is the mean. There was insignificant change in impedance of individual jULIE channels above the OB, at the OB surface, and after penetrating 1300 µm.

4.4.2 Camera recordings in vivo

After functionalized microwires were demonstrated to be excellent electrodes, microwire bundle electrodes were connected to the ROIC chip for *in vivo* testing to assess the system's ability to record neural activity. After fabricating and functionalizing (see 4.1.3) the electrodes were connected to the camera chip (see 4.2.2) and inserted into the brain of an anaesthetized mouse (see 3.12). Some recorded traces had the defining shape and frequency of LFP (see 1.2.3). These LFP traces were similar to recordings from the same brain area recorded by a jULIE as demonstrated by the similar phase when the traces are

aligned (Fig. 4.22). However, only ~10 out of the 100 wires in the bundle electrode had a strong connection to a pixel and 4 showed LFP.

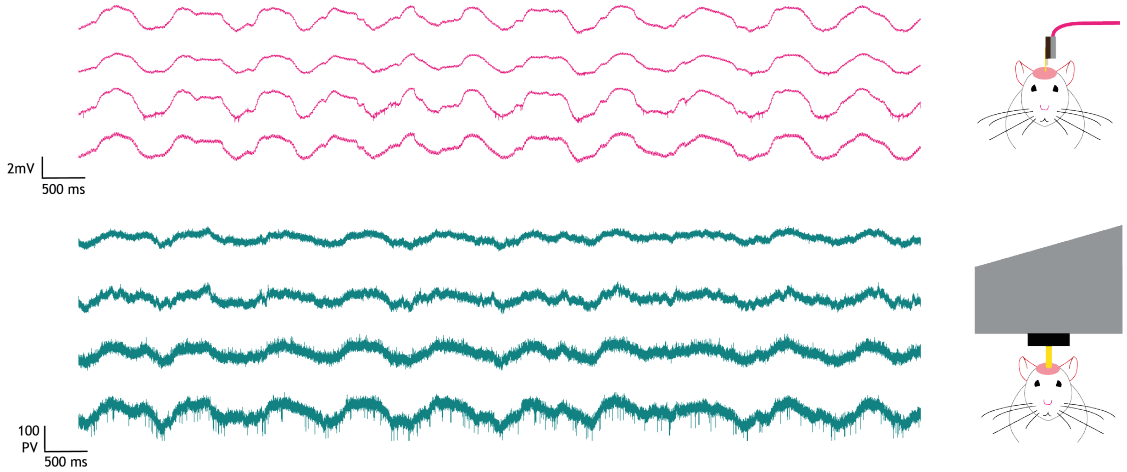

Figure 4.22: LFP *in vivo*. Recording from 4 channels of a jULIE (Top) and bundle electrode connected to the chip (Bottom) in separate experiments from an anaesthetized mouse. jULIE recordings displayed in mV and recordings from the chip in pixel values. Traces were filtered <3kHz.

To further validate that biological signals were recorded with the camera readout, a simultaneous recording was devised by connecting individual channels from a jULIE with a T-junction, split with one direction to the headstage of a conventional amplifier and the other to a single wire connected to a camera pixel. First a single wire was connected to a pixel (as in 4.3.2), then the jULIE was inserted into tissue until a strong unit was picked up by the amplifier system and then the channel was connected to the camera pixel. In this manner, a unit was simultaneously recorded with the jULIE amplifier and the chip readout (Fig. 4.23).

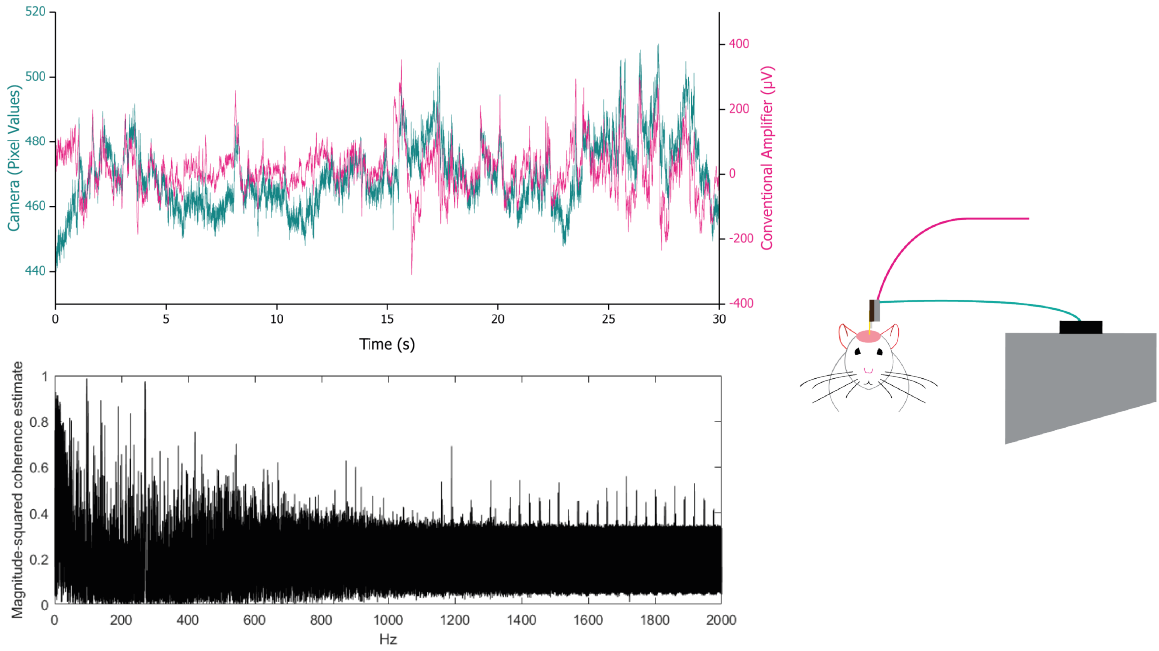

Figure 4.23: *In vivo* validation. A simultaneous recording from a jULIE channel connected both to its normal amplifier and the chip readout and a schematic representation of the experimental setup. Both traces were acquired at a sampling rate of 27.1 kHz and low pass filtered <3kHz (top). Cross coherence of the 2 traces with a Welch window up to 2kHz (bottom).

This recording showed LFP like events simultaneously recorded by both readouts. This suggests that biological activity had some contribution to the activity recorded by the chip. The cross coherence of the two signals was highest at frequencies <200 Hz which encompasses the bandwidth of LFP. There seems to be more noise on the recorded conventional amplifier signal than in standard jULIE experiments. This is possibly from the added axial resistance of the connection and current exchange from the camera to the amplifier. This turned out to be an imperfect method of ground truth validation because activity from the camera can distort the jULIE signal and as such, this labor intensive experiment was only performed once.

To separate the difficulties of connecting the chip end of a bundle electrode with a high connectivity rate from recording in tissue with this electrode, a connector was developed which linked each channel of a jULIE to a 100 µm uninsulated copper wire which readily connected to indium bumps. The copper wires were connected to the Ghost Lifter to raise the voltage to the reference of the camera while aligning against the chip with the three-armed setup. After connectivity was settled on, the back end of the connector was then connected to a jULIE ready to be inserted into an anaesthetized mouse. Data was streamed from the strongly connected pixels while inserting into tissue. In this experiment odor was delivered (see 3.13) and respiration was recorded. Before recording *in vivo*, a 1 mV signal was applied to the bath to later calibrate the pixel responses.

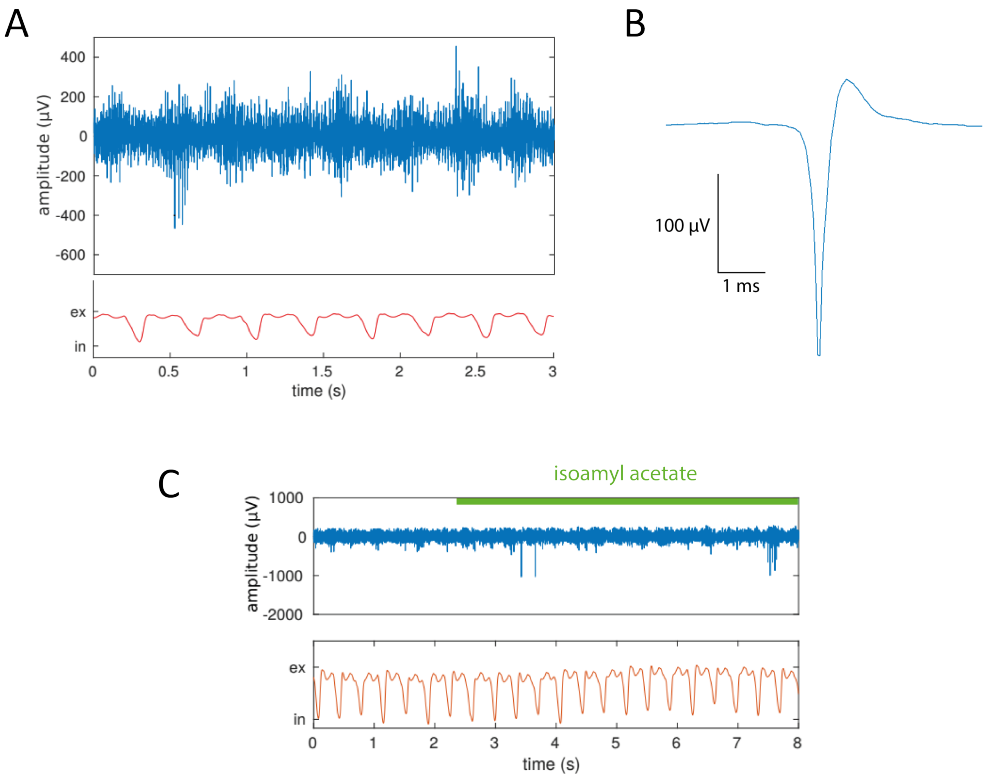

Figure 4.24: Spiking activity *in vivo*. **(A)** Extracellular trace from one pixel (blue, band-pass filter 500-5kHz) and respiration (red, unfiltered) in the mouse OB at a depth of 1200 µm. **(B)** Average waveform of spikes over 1000 pixel values from one pixel. The 780 s trace was high pass filtered (>100 Hz). **(C)** Spikes during odor presentation (green, isoamly acetate).

The recorded trace from a strongly connected pixel revealed spiking activity (Fig. 4.24A) and its amplitude was converted from pixel values to µV based on its response to a 1 mV waveform. The average waveform of detected spikes (over 1000 pixel values, ~350µV threshold) had the characteristic shape of a single unit action potential (Fig. 4.24B). A recorded unit also appeared to spike in response to the presentation of the odorant isoamyl acetate (Fig. 4.24C).

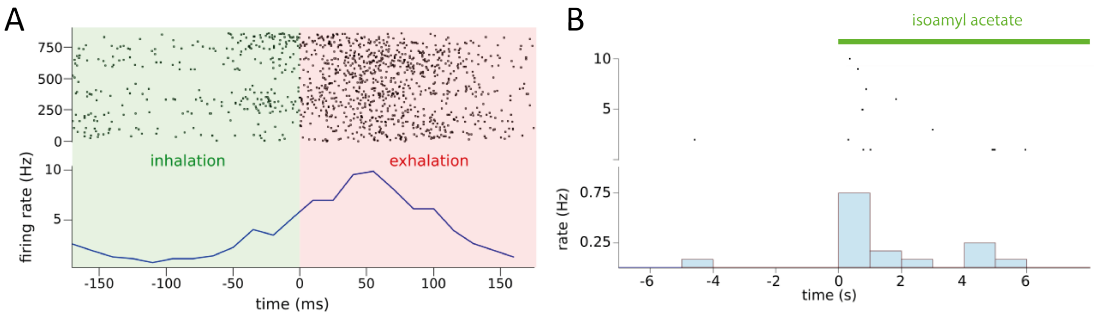

Figure 4.25: Respiration and odor coupling. **(A)** Raster of detected spikes (Top, trials are bins the length of 1 respiration cycle) aligned to the respiration phase. Firing rate (Bottom) increased in the exhalation phase of respiration (peak ~50 ms). **(B)** Raster of large spikes (> 1mV) (Top, trials are binned to odor presentation cycle) aligned to the presentation of isoamyl acetate and the firing rate of these spikes in 1 s bins (Bottom).

The relationship of spike rate to the respiration phase was also analyzed. One recorded unit had an increased firing rate in the exhalation phase of respiration demonstrating the cell had some coupling to the respiration cycle (Fukunaga et al., 2012) (Fig. 4.25A). The spike rate was also aligned to odor presentation and there was an increase in firing rate of large spikes directly after the delivery of isoamyl acetate (Fig. 4.25B).

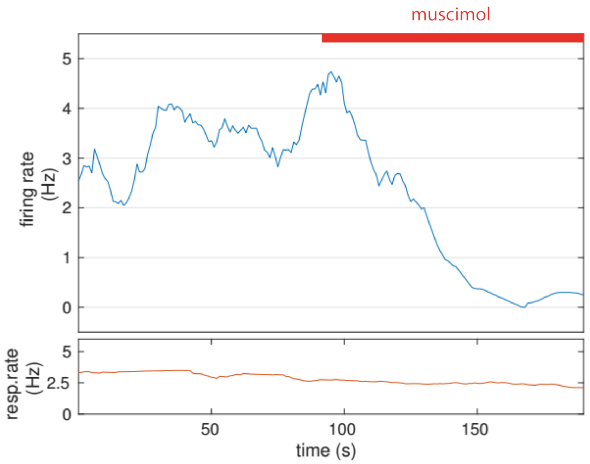

Figure 4.26: Spiking inhibition with muscimol. Superfusion of 100 µM muscimol suppressed firing of the recorded unit.

To confirm that recorded signals were of biological origin, the GABA agonist muscimol was superfused over the brain at the end of the experiment. Muscimol has been known to broadly abolish spiking activity when applied *in vivo* (Caesar et al., 2003). Muscimol inhibited overall firing rate of the recorded unit and spike rate diminished after 3 minutes (Fig. 4.26). These results suggest that well connected wires from a bundle electrode can record the spiking activity of single units in an anaesthetized mouse.

4.4.3 Imaging of insertion

It is also important to analyze the effects of electrode insertion on the tissue around the recording site. Extracellular recording electrodes are known to cause acute and chronic damage after being inserted into brain tissue (Kozai et al., 2015b). Through histology (see 3.14) we compared the acute damage caused by angle polished microwires and a common silicon probe (Fig. 4.27).

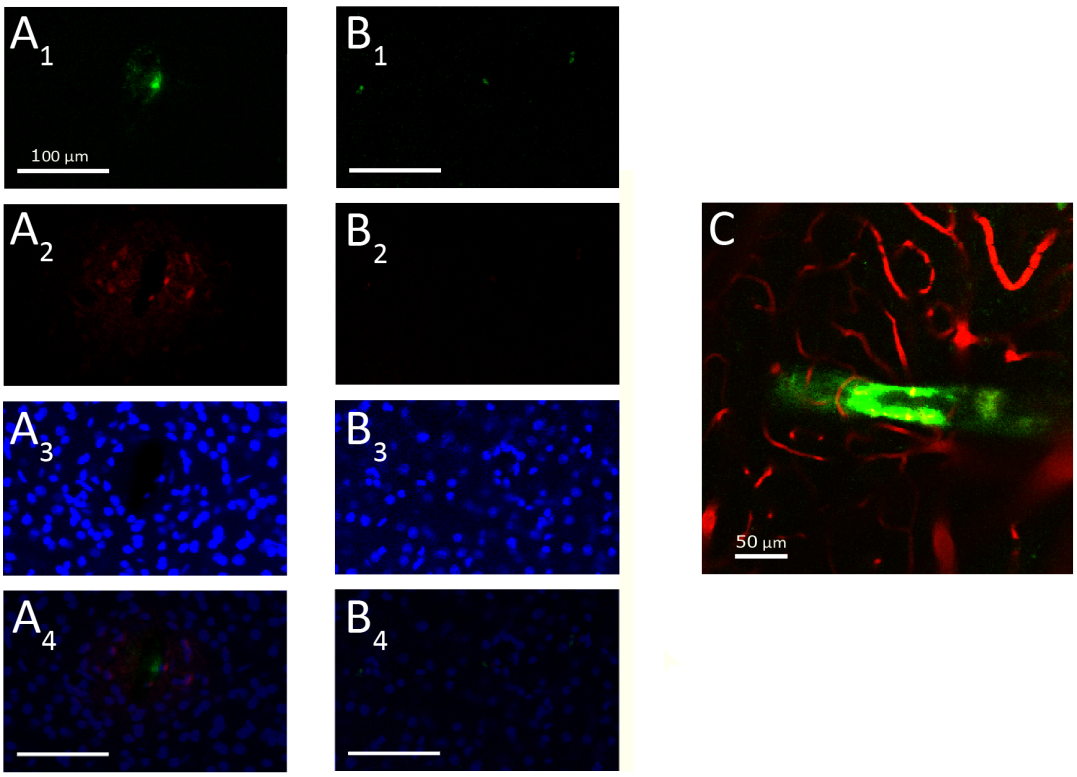

Figure 4.27: Acute damage from insertion of a silicon probe and glass ensheathed microwires. Histology was performed after insertion of a silicon probe with a 123 µm wide shank **(A)** and 30° angle polished glass ensheathed microwires **(B)**. Insertion sites are marked with arrows. Three fluorescent dyes were employed: DiO which traced the insertion lesion (1, green), Evans Blue which binds to albumin and represents rupture of the blood brain barrier (2, red), DAPI which stains cell nuclei (3, blue), and a color overlay of each image with opacities adjusted to make each layer visible. All scale bars are 100 µm. **(C)** Two-photon microscopy image of an angle polished wire coated in DiO inserted into tissue with blood vessels stained by Sulforhodamine 101.

Based on images with all three histological markers, microwires had a smaller insertion profile than the silicon probe. The silicon probe caused bleeding as evidenced by the Evans Blue stain and left a tear in tissue nearly 100 µm wide. In contrast, the spaced microwires did not cause any detectable blood brain barrier damage and had an insertion track of only a few microns. Fig. 4.27C demonstrates that single wires can be inserted

and penetrate through brain tissue such that blood vessels are not severed. These results taken together suggests that in acute experiments, individual microwires cause much less damage than the standard silicon probe.

To visualize the insertion of a bundle electrode in 3D, a micro-CT was used to image an entire mouse head after insertion (see 3.15). Fig. 4.28 shows hundreds of angle polished wires after insertion into cortex. It demonstrates that large bundle electrodes easily penetrate tissue and that in the 3D image the wires can be detected against the background tissue. However, the bundle does not readily spread out during insertion and clusters together when no effort is made to space the wires in the bundle.

Figure 4.28: Micro-CT of bundle insertion. Low resolution image of the bundle electrode (1100 microwires) inserting into the whole brain and a high resolution image of a portion of the neuronal end of the bundle electrode in tissue.

4.4.4 Conclusion

These results demonstrate that functionalized angle polished wires can serve as electrodes to record LFP and spikes as part of a jULIE connected to a conventional amplifier or as a bundle electrode connected to the camera readout. jULIEs can even detect amplitude change with proximity to the neuron. It may be possible to estimate the point source (neuronal cell body) location from these amplitude vs vertical displacement plots. If more data was collected within a precisely controlled preparation, the recording quality of different jULIE designs or other electrode technologies could be compared.

In anaesthetized odor presentation experiments, cells in the OB responded to isoamyl acetate and were coupled to the animal's respiration. To verify the biological origin of the spikes, muscimol was applied to the brain which inhibited the spiking activity of the recorded cell. If more electrodes could simultaneously record *in vivo*, the activity of entire olfactory circuits could be studied in response to different odor stimuli.

Angle polished microwires perform well in acute experiments because there is barely detectable tissue damage after insertion and the electrode impedance does not significantly change after insertion into tissue. Histological experiments could be improved in order to gain a more complete understanding of the foreign body response to bundle electrodes. Stains for cell membrane integrity (such as propidium iodide, Blanche et al., 2005) and immunohistological stains for glial cells (such as Iba-1 for microglia and glial fibrillary acidic protein for astrocytes, Kozai et al., 2012a) would determine how the electrodes are encapsulated during the inflammatory response. Histology should also be performed days to weeks after electrode implantation to uncover the chronic tissue response to these electrodes.

Though individual microwires, readily insert into tissue without causing excessive damage, micro-CT images demonstrate that larger bundle electrodes do not appear to separate in tissue. Thus suggests new insertion methods and methods to control the spacing of wires during bundle electrode fabrication should be developed to minimize tissue damage (see 5.4). Locating the tips of electrodes within the acquired 3D image is possible but without custom algorithms it the images would need to be manually segmented. Automating this process would be computationally difficult for bundles >100 wires as the electrodes are in different planes. However, histological contrast agents could help to better separate the metal/glass electrodes from the surrounding tissue in these images.

5 Discussion

5.1 Proof of Principle

The aim of my project was to develop a new technology that was a scalable approach to large scale electrophysiology. I have described an extracellular recording technique combining glass ensheathed gold microwire bundles and a high speed ROIC chip which can viably record single unit activity *in vivo*. Experiments *in vitro* demonstrated that bundle electrodes have predictable stray capacitance based on their dimensions and that microwires with electrochemically functionalized low impedance films connected to the camera readout can record and resolve simulated spike-like signals (see 4.3). *In vivo* recordings reveal functionalized angle polished wires connected to the camera readout are capable of recording local field potentials and individual action potentials. The action potential firing rate was coupled to the animal's respiration cycle, increasing when odor was presented, and was abolished with the application of the drug muscimol (a GABA agonist which inhibits neural activity), confirming that recorded spikes were biological in origin (see 4.4.2).

This design has multiple advantages over existing techniques for large scale neuronal recording. The camera readout has a sampling rate of 1.7 kHz full frame (up to 200 kHz for smaller frames) which is greater than the sampling rate of modern two-photon imaging techniques which struggle to record at 1 kHz. Unlike the ~2 mm recording depth limitation of 2-photon microscopy, this technique does not have a recording depth limitation, potentially allowing recording from deep brain structures more than 5 mm below the brain surface. Bundle electrodes have more flexible design parameters (variety of microwire diameters, polishing angles, and overall bundle geometry) and greater horizontal coverage of tissue than planar silicon probes. Microwires also cause less acute tissue damage and have lower stray capacitance than traditional silicon probes (see 4.4.3). Though this neurotechnology is very scalable - as discussed below, we do not yet show data of more than a few simultaneous channels. Though once the problem of bundle electrode to readout connectivity is solved, the number of recorded neurons will scale with higher wire count bundle electrodes and the increasing density of readout electronics.

5.2 Scalability

A system is *scalable* if its performance improves proportionally to the increasing capacity of its hardware. Imaging techniques such as two-photon microscopy have increasing temporal resolution with faster beam repositioning due to hardware improvements with acouso-optic deflectors and other devices. However, the scalability of this technique is fundamentally limited because light diffraction in tissue limits the recording depth and since light dissipates as heat in tissue the brain would overheat with many recorded neurons at high

framerates. To overcome these limits, systems that could excite two-photon fluorescence without high energy laser pulses or fluorophores that are excited at infrared wavelengths would need to be developed (Marblestone et al., 2013). Silicon probes for extracellular recording have increasing recording site density and matching on-wafer electronics due to their photolithographic fabrication process which has allowed an exponential increase in simultaneously recorded neurons over the years (Fig. 1.3). But tissue damage scales with the size of and number of electrode shanks. Advanced extracellular technologies (such as carbon fibers and flexible polymer electrodes) integrate into tissue very well but do not have scalable fabrication or readout electronics which limits the number of simultaneous channels (Park et al., 2017; Patel et al., 2015). The connection to the electronics would need to be fundamentally redesigned for the number of recording channels to scale up.

Both the bundle electrodes and electronic readout scale easily to higher densities in this design. The readout integrated circuit (ROIC) currently has more than 300,000 active amplifiers. ROIC technology will continue to develop in the future creating denser amplifier arrays with better temporal resolution. Software and data storage/transfer rates will also scale with cutting edge higher density readouts. The bundle electrodes are scalable because the number of microwires in a bundle is only limited by how many spools are wrapped together. Bundle electrodes are currently fabricated with up to 2,000 wires, but it takes minutes to wrap thousands of more wires. The fundamental limit to bundle electrode size is that the area of the tissue end must be small enough to insert into a craniotomy and not cause excessive damage in the target brain region.

5.3 Improving connectivity

The indium bumps on each pixel of the camera chip were designed to be bonded to a photodetector layer and remain sealed beneath the chip package. In this system the photodetector is never added and the indium bumps are exposed to air where the indium can readily oxidize and the bumps are contacted to the back end of electrodes with varying amounts of force. The malleable bumps deform and break during electrode contact (Fig. 4.8) and the indium oxide layer may be increasing the connection resistance. If the pads on each pixel were a harder and more inert metal, electrode contact would be more straightforward and could be stable for longer timescales.

It is possible to replace indium bumps on a ROIC chip by taking wafers from the manufacturer that have not been indium bump bonded and depositing platinum pads on every pixel through a mask (Mina Hanna, Nick Melosh, and Andreas Schaefer, personal communication). Chips modified in this way should allow a more reliable and reversible metal contact between bundle electrodes and the readout electronics. Alternative readout electronics will also be considered in the future. Other ROICs designed for imaging applications are also available off the shelf. Higher resolution arrays (up to 1280x1024) are

available from multiple vendors (Cardinal, Mikro-Tasarim, Princeton Infrared Technologies, FLIR) but these designs do not match the >1 kHz framerate of the Xenics Cheetah ROIC. The disadvantages of this chip are its internal offset voltage and the innate differences in gain between pixels which means that equal changes in pixel value may not represent identical voltage signals. It is possible for a custom designed chip to withhold this offset voltage but this custom design would not be independently developed by the infrared imaging industry. An alternate ROIC design has also been developed which allows for in-pixel digitization, greatly reducing the complexity, size, and power requirement of its chip (Rider et al., 2011).

There are a few commercially available multielectrode array (MEA) designs which were designed for *in vitro* neuronal recordings but could potentially function as a readout for bundle electrodes. MEAs from 3Brain have an array of 4096 electrodes that can simultaneously stream data (Maccione et al., 2015) and MaxWell Biosystems produce an MEA with 26,400 electrodes with 1024 simultaneous channels (Müller et al., 2015). Both of these systems have dedicated software for filtering and spike detection and are less expensive than the high speed infrared cameras which contain ROICs. However, since these MEAs are built with wells for *in vitro* recording, they may require significant modification to allow connection of bundle electrodes.

Bundle electrodes can connect to the ROIC chip via interconnect foils or freed wire alignment (see 4.2). The alignment system has 3 micromanipulators which move the electrode and greatly increase the size and weight of the entire system. A more advanced version of the alignment system is being developed which has a much smaller profile and does not require added manipulators. In this passive alignment system only as large as the camera lid, the bundle electrode self-aligns while force is applied from a screw around the embedded electrode. The alignment process is faster for the experimenter and improved connection rates have been reported (Mina Hanna, Nick Melosh, and Andreas Schaefer, personal communication). A more advanced future technique would be designing ordered bundles which match the pitch of the chip which could be precisely aligned by perpendicularly illuminating with laser light and interpretation of light diffraction patterns.

5.4 Bundle electrode insertion and spacing

There are a variety of forces acting on extracellular probes when they are inserted into brain tissue. Insertion can be divided into three stages: the tissue compression stage where the tissue dimples beneath the probe, the tissue penetration where the probe ruptures the tissue and the resistance force decreases, and the loading phase where as the probe travels deeper into tissue the friction increases the resistance force (Sharp et al., 2009). The extent of these forces depends on probe material elasticity, probe size, probe sharpness, and insertion rate. Probes with smaller cross sectional area have smaller penetration forces

but are more susceptible to buckling, as modeled by the Euler buckling force:

$$F = \frac{\pi^2 EI}{(KL)^2}$$

For a glass ensheathed gold microwire, the modulus of elasticity, E ≈ 70 GPa (79 GPa gold, 65-75 GPa glass), the area moment of inertia for the circular cross section, $I = (\frac{\pi}{4})r^4$, and the column effective length factor K = 0.707 for one end fixed and the other end pinned (Marblestone et al., 2013). When the diameter of the wire is 20 µm with a free length of 2 cm the calculated buckling force is ≈ 27 µN and when the free length is 1 mm the buckling force is 10.8 N. For a wire 20 µm in diameter, an estimated force based on the experimental tissue resistance results of Sharp et al. is about 100 µN, which sets a threshold for when the wire would buckle. This is a rough estimate because in that study the wires were tungsten and 100 µm in diameter (the exact relationship of tissue resistance to probe area is not known). However, this suggests that for 20 µm microwires when the freed length is less than ~1 cm they are unlikely to buckle during tissue penetration.

For *in vivo* experiments the bundle electrodes had about 5 mm of freed length and the neuronal end of the electrode was inserted at ~1-5 µm per second by raising the anaesthetized mouse with a micromanipulator into the perpendicularly aligned bundle electrode. There is no consensus on the ideal parameters for electrode insertion speed (Hosseini et al., 2007; Bjornsson et al., 2006; Casanova et al., 2014; Mahvash and Dupont, 2010) or angle with respect to the brain (Claverol-Tinture and Nadasdy, 2004). In order to elucidate this question, experiments could be performed varying variables such as insertion rate, wire diameter, and polishing angle and relating them to the amount of tissue compression during insertion and the amount of damage evidenced through histology in order to optimize insertion parameters for the bundle electrodes.

It is clear from imaging bundles in tissue that when individual angle polished microwires are spaced by ~100 µm there is minimal damage (Fig. 4.27). In its current design the tissue damage caused by individual microwires is less than that of an entire silicon probe shank. However in the same tissue volume around the insertion track the bundle electrode features less channels than that of the silicon probe shank. Also, dense bundles do not readily spread out in tissue (Fig. 4.28) which will increase the local tissue damage and limits the volume of tissue in which neurons can be recorded. If future developments could allow for uniform spacing of wires within a bundle electrode during insertion, the overall tissue damage could be reduced below that of standard electrodes.

There are a number of ways in which spacing of bundle electrodes could be controlled during fabrication. The microwires themselves could be manufactured such that they have double glass cladding where the outer glass has a matched melting point to the inner glass but is etchable in acid (Tonucci and Hubler, 2007). With these etchable wires, the tissue end could be spaced by immersing in acid after polishing and the spacing distance

would be determined by the outer glass diameter and packing density. The center of bundles could also be filled with glass beads to separate the wires before the bundle is sealed. A more controlled method would be spraying the microwires with insulating parylene before wrapping with the insulation thickness determining the bundle spacing. If a reliable method was found to regularly space the tissue end of bundle electrodes, this should result in less tissue damage and bleeding during insertion which would ultimately increase the yield of recorded units. However, even with adequately spaced bundles, additional modifications may need to be made to the bundle electrodes in order to have the microwires splay out in tissue to record from a greater tissue volume. Electrodes could be pre-splayed before insertion by dividing the bundle into smaller bundles and twisting them such that they actively spread when released in tissue.

5.5 Improving bundle electrode fabrication and density

Currently the procedure for bundle electrode fabrication is very time consuming and involves manual intervention. If the electrode fails in an early stage (generally because a significant amount of wires within a bundle are not electrically connected for deposition, see 4.1.3), fabrication must restart. If fabrication methods can be more standardized and automated the final product will be reproducible, more symmetrical electrodes likely with improved connectivity. Opportunities for fabrication standardization include designing interlocking polypropylene support tubes, building molds which perfectly center the bundles during embedding, and standardizing the volumes of embedding materials. Since each bundle electrode is an investment of time (minimum 2 days for a batch of electrodes) and materials (especially when the number of microwires in the electrode increases), techniques should be developed to clean and reuse bundle electrodes after insertion into the brain. Commercial silicon probes such as NeuroNexus can be re-used 10-15 times until the impedance begins to rise to unacceptable levels (NeuroNexus, 2008).

The number of active recording sites in bundle electrodes must increase to take advantage of the high density readout of the camera electronics and to record from many more neurons simultaneously. A possible fabrication process to accommodate bundles of 10 thousand microwires is described in Fig. 5.1. The first major difficulty with larger bundles was in sealing the outer glass such that electrolyte could not flow through the bundle as common epoxies were too viscous to penetrate a bundle of this size. In pilot experiments, this was attempted by fusing the outer glass by heating to the glass melting point with a high powered induction heater, a process we call 'caking'. Embedding large bundles in Crystalbond 509 polymer (CB) resulted in groups of wires left un-embedded which damaged the wire surfaces during polishing. However, by implementing high temperature desiccation, these bundles could be completely embedded in CB and complete removal of CB to separate the wires for tissue insertion was accomplished by increasing the number

of washes in CB stripper. During first attempts at fabricating full length bundles with over 1000 wires, gold was unable to be electrodeposited on a significant fraction of the wires after polishing possibly due to damage incurred by the wires during caking. An alternative method for increasing the number of microwires in an electrode would be fabricating several bundles individually and connecting them to the ROIC chip together. In this way, a greater fraction of the chip could be utilized whilst allowing individual bundles within the electrode to be customized for different brain areas.

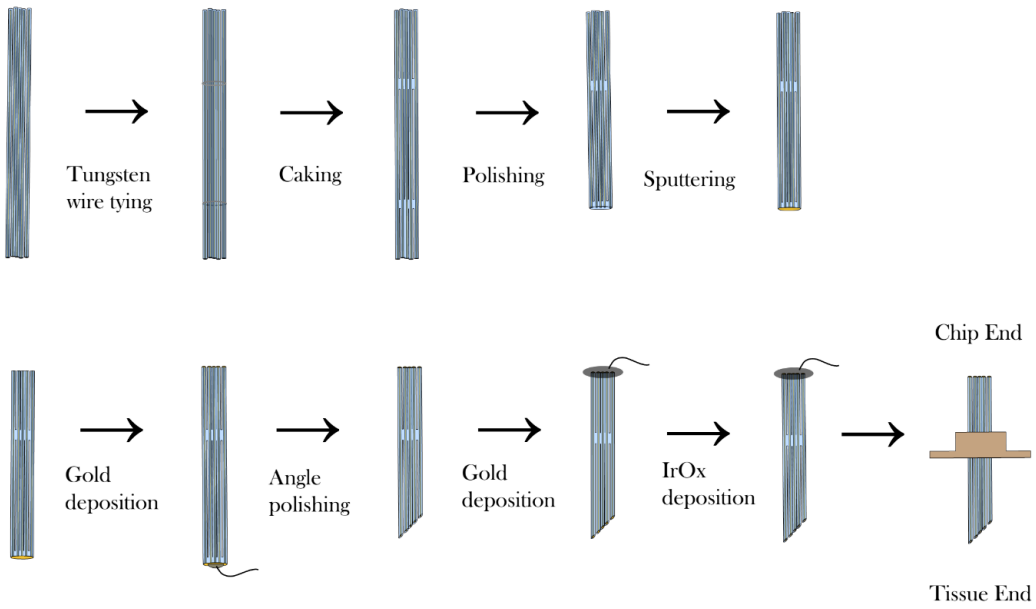

Figure 5.1: Large bundle fabrication schematic. A possible future design to fabricate bundles of thousands of microwires for *in vivo* experiments.

Part of the reason glass ensheathed metal microwires were initially chosen as an electrode material is that it had been reported that bundles of thousands of microwires could be heated and pulled to a taper which reduced the overall size of the bundle while maintaining the inner to outer diameter ratio (Badinter et al., 2010). This tapering could eventually be applied to the bundle electrode fabrication protocol. With a tapered tip, the tissue end would displace significantly less tissue during insertion while the chip end would maintain its dimensions for chip connectivity. However, thinner wires are more prone to buckling so a shorter freed length may be required for these bundles to penetrate tissue. Also, as a possible solution to stiffen the microwires and reduce buckling, the bundles could be coated with a biocompatible coating such as silk (Tien et al., 2013), gelatine (Etemadi et al., 2016), or polyethylene glycol (Patel et al., 2015).

5.6 Chronic recordings

To understand how neural circuits function, neural activity must be recorded over longer time periods than the few minutes used to generate *in vivo* results in this thesis (see 4.4.2). The bundle electrodes and ROIC interface would need to be modified in order to adapt to chronic experiments. Firstly, additional histology experiments should be performed to better understand the inflammatory response to bundle electrodes (see 4.4.4) and determine the timescale of glial encapsulation. *In vivo* recordings (with jULIEs or bundle electrodes connected to the camera readout) could be repeated hours after insertion to determine if tissue damage and the foreign body response affects the recording properties of electrodes. Another requirement for chronic experiments is improvement of the stability of electrode connectivity to the chip (discussed in 5.3).

Electrode technologies which permit animals to move freely during recording allow the study of more complex behaviors than in head-fixed preparations (such as social interactions between animals and spatial memory tasks). To allow animals fee movement during recordings, longer bundle electrodes could be used which would allow the readout electronics to sit farther away from the animal. Long electrodes are feasible because of the flexibility of the microwires and their very low stray capacitance (~1 pF/cm, Fig. 4.15). It is unlikely for the chassis of the ROIC electronics to decrease in size enough in the near future to be mounted to a rodent, although if the technology were applied to primates, this might be feasible. If this technology can be improved to record over longer timescales without the need to restrict the animal's head movement, it can be further developed as a neuroprosthetic device in larger mammals (sheep, primates, etc.) and ultimately in human trials.

5.7 Alternate bundle electrode materials

Within the same bundle electrode architecture, different electrode materials could be considered which offer specific advantages. Polymer microwires could be considered as an alternative to glass ensheathed gold microwires for bundle electrodes (Yaman et al., 2011; Tao et al., 2012). These wires are pulled from a polymer preform at a lower temperature and are softer and more flexible than glass and metal. Polymer wires can be made with cores of semiconductors, conductive polymer composites, low melting point metals such as tin, or even fiber optic channels for light delivery (Canales et al., 2015). These conductive core materials have higher axial resistance than pure metal cores meaning they would limit the signal to noise ratio recorded by surface areas <50 μm^2. Also, since the wires are so flexible (Young's modulus ~3 GPA) they are more likely to buckle and thus may need a coating to stiffen them or a shuttle to enable insertion into tissue.

The polished interface of glass ensheathed gold microwires are an established substrate for the electrodeposition of IrOx. However, it would be easier to pull metal cores to smaller dimensions from an alloy than from gold. In this case electrodes would need a layer of electrodeposited gold on the alloy core to act as a substrate for IrOx because IrOx does not deposit well on copper alloys. Also, other alternative low impedance coatings for the recording sites could be considered, such as PEDOT (Wilks et al., 2009) or carbon nanotubes (Bareket-Keren and Hanein, 2013). These coatings may offer better adherence to the electrode, longer lifetime, and lower impedance.

5.8 Wire localization

Once high channel counts can be recorded with bundle electrodes *in vivo*, the implementation of spike sorting algorithms will be necessary to identify individual units recorded by multiple wires. The large amount of recordings that can be collected in a single session and the file size of these datasets will continue to be a challenge in the future. Improved software will need to be developed in order to filter out signals from unconnected wires and to reduce the dimensionality of acquired data in order to reduce file sizes. The wires will not be regularly spaced in tissue because the wires are not at exactly the same height after fabrication and individual wires will have non-parallel trajectories through non-uniform brain tissue. Depending on the recording density, we may also consider trying to estimate the location of signal sources from information in the extracellular traces (Cybulski et al., 2015) or by imaging with 3D micro-CT after *post-hoc*. Additionally, if the necessary optics could be accommodated, specific target neurons could be stimulated optogenetically in order to probe the circuit, aiding the identification of units of a given molecular identity. However, from bundle electrode recordings the function (spike rate, waveform, response to stimuli, etc.) of the recorded neurons and its relationship to the activity of other neurons is more important than their absolute position in the brain or molecular identity.

5.9 Theoretical limits

It is difficult to determine the idealized bundle electrode geometry to record from a maximum number of neurons in an entire brain or brain region. Properties of the bundle electrode such as individual wire diameter, recording site area, and distance between the wires all affect the theoretical threshold of recorded neurons and the total volume displacement. The anatomical spacing of active neuronal cell bodies in the target brain region will also determine the yield of neurons.

Extracellular voltages are detected in a sphere around each electrode recording site. The relatively large recording sites in traditional silicon probes and tetrodes allow the activity of multiple neurons to be recorded at each channel which are separated into individual

units via spike sorting methods (see 1.3.4). The absolute algorithmic limits of spike sorting is estimated to allow unit separation of ~100 neurons per electrode which would require 750,000 recording sites spaced 80 µm from each other in a cubic lattice to record from an entire mouse brain (Marblestone et al., 2013). However, if recording sites are small enough and proximal enough to the cell membrane to measure the activity from only individual neurons, there will not be multiple units to sort. If bundle electrodes were perfectly designed to record from only single neurons at each recording site, this inability to spike sort could decrease the overall yield of recorded units from a brain area.

For bundle electrodes, changes in core diameter affect the volume from which the recording site can sample neural activity, while the thickness of the insulating glass affects the tissue volume the electrode will displace and the stray capacitance along the electrode length. Marblestone et al. suggest displacement of 1% of total tissue volume as an absolute limit for extracellular recording. In this case, whole brain recordings in the mouse are unlikely to be limited by volume constraints, but depending on how many neurons can be recorded by a single wire, wires would need to shrink down to ~200 nm to record from a whole brain without displacing too much tissue (Marblestone et al., 2013).

Idealized electrode geometries also come with practical limitations. Electrode bundles composed of nanowires would be nearly impossible to fabricate and handle. Bundle electrodes comprising tens of thousands of wires, especially if they are spaced, would require a very large craniotomy covering a significant portion of the cortex in order to be inserted. In short, the ideal electrode parameters which minimize tissue damage and maximize cell yield are still up for debate.

5.10 Outlook

In proof of principle experiments I have demonstrated that the combination of microwire bundle electrodes and ROICs is a promising method for large scale neuronal recording *in vivo*. There are numerous developments to be made in this technique, but the overall design is highly scalable and will advance alongside integrated circuit technology. This technique could potentially accelerate the existing trend towards a greater number of simultaneously recorded neurons (Fig. 1.3) in behaving mice and other animal experiments. There is also the prospect that this design may be of use in human subjects, as a neuroprosthesis re-enabling loss of limb control due to spinal chord injury, to reduce the symptoms of Parkinson's disease and ALS, or to restore deafness and blindness. Massively parallel electrode neurotechnologies could also potentially lead to brain machine interfaces with digital intelligence, the possibilities of which are as yet unexplored.

6 References

References

Abbott J, Ye T, Qin L, Jorgolli M, Gertner RS, Ham D, Park H (2017) CMOS nanoelectrode array for all-electrical intracellular electrophysiological imaging. *Nature Nanotechnology* 12:460–466.

Abidian MR, Kim DH, Martin DC (2006) Conducting-polymer nanotubes for controlled drug release. *Advanced Materials* 18:405–409.

Alivisatos AP, Chun M, Church GM, Greenspan RJ, Roukes ML, Yuste R (2012) The Brain Activity Map Project and the challenge of functional connectomics. *Neuron* 74:970–974.

Anderson DJ, Najafi K, Tanghe SJ, Evans DA, Levy KL, Hetke JF, Xue X, Zappia JJ, Wise KD (1989) Batch-Fabricated Thin-Film Electrodes for Stimulation of the Central Auditory System. *IEEE Transactions on Biomedical Engineering* 36:693–704.

Angle MR, Schaefer AT (2012) Neuronal recordings with solid-conductor intracellular nanoelectrodes (SCINEs). *PLoS ONE* 7.

Azevedo FAC, Carvalho LRB, Grinberg LT, Farfel JM, Ferretti REL, Leite REP, Filho WJ, Lent R, Herculano-Houzel S (2009) Equal numbers of neuronal and nonneuronal cells make the human brain an isometrically scaled-up primate brain. *Journal of Comparative Neurology* 513:532–541.

Badinter E, Ioisher A, Monaico E, Postolache V, Tiginyanu IM (2010) Exceptional integration of metal or semimetal nanowires in human-hair-like glass fiber. *Materials Letters* 64:1902–1904.

Bakkum DJ, Frey U, Radivojevic M, Russell TL, Müller J, Fiscella M, Takahashi H, Hierlemann A (2013) Tracking axonal action potential propagation on a high-density microelectrode array across hundreds of sites. *Nature Communications* 4:1–12.

Bareket-Keren L, Hanein Y (2013) Carbon nanotube-based multi electrode arrays for neuronal interfacing: progress and prospects. *Frontiers in Neural Circuits* 6:1–16.

Bean BP (2007) The action potential in mammalian central neurons. *Nature Reviews Neuroscience* 8:451–465.

Bérces Z, Tóth K, Márton G, Pál I, Kováts B (2016) Neurobiochemichal changes in the vicinity of a nanostructured neural implant. *Scientific Reports* 6.

Berényi A, Somogyvári Z, Nagy AJ, Roux L, Long JD, Fujisawa S, Stark E, Leonardo A, Harris TD, Buzsáki G (2014) Large-scale, high-density (up to 512 channels) recording of local circuits in behaving animals. *Journal of Neurophysiology* 111:1132–1149.

Biran R, Martin DC, Tresco PA (2005) Neuronal cell loss accompanies the brain tissue response to chronically implanted silicon microelectrode arrays. *Experimental Neurology* 195:115–126.

Bjornsson CS, Oh SJ, Al-Kofahi Ya, Lim YJ, Smith KL, Turner JN, De S, Roysam B, Shain W, Kim SJ (2006) Effects of insertion conditions on tissue strain and vascular damage during neuroprosthetic device insertion. *Journal of Neural Engineering* 3:196–207.

Blanche TJ, Spacek MA, Hetke JF, Swindale NV (2005) Polytrodes: high-density silicon electrode arrays for large-scale multiunit recording. *Journal of Neurophysiology* 93:2987–3000.

Boehler C, Stieglitz T, Asplund M (2015) Nanostructured platinum grass enables superior impedance reduction for neural microelectrodes. *Biomaterials* 67:346–353.

Boehler C, Oberueber F, Schlabach S, Stieglitz T, Asplund M (2017) Long-Term Stable Adhesion for Conducting Polymers in Biomedical Applications: IrOx and Nanostructured Platinum Solve the Chronic Challenge. *ACS Applied Materials & Interfaces* 9:189–197.

Bollmann L, Koser DE, Shahapure R, Gautier HOB, Holzapfel GA, Scarcelli G, Gather MC, Ulbricht E, Franze K (2015) Microglia mechanics: immune activation alters traction forces and durotaxis. *Frontiers in Cellular Neuroscience* 9.

Brown EN, Kass RE, Mitra PP (2004) Multiple neural spike train data analysis: state-of-the-art and future challenges. *Nature Neuroscience* 7:456–461.

Brown E, Frank L, Tang D, Quirk M, Wilson MA (1998) A statistical paradigm for neural spike train decoding applied to position prediction from ensemble firing patterns of rat hippocampal place cells. *Journal of Neuroscience* 18:7411–7425.

Brummer SB, Robblee LS, Hambrecht FT (1983) Criteria for Selecting Electrodes for Electrical Stimulation: Theoretical and Practical Considerations. *Annals New York Academy of Sciences* 405:159–171.

Buzsáki G (2004) Large-scale recording of neuronal ensembles. *Nature Neuroscience* 7:446–451.

Buzsáki G (2010) Neural Syntax: Cell Assemblies, Synapsembles, and Readers. *Neuron* 68:362–385.

Buzsáki G, Anastassiou Ca, Koch C (2012) The origin of extracellular fields and currents–EEG, ECoG, LFP and spikes. *Nature reviews. Neuroscience* 13:407–20.

Caesar K, Thomsen K, Lauritzen M (2003) Dissociation of spikes, synaptic activity, and activity-dependent increments in rat cerebellar blood flow by tonic synaptic inhibition. *Proceedings of the National Academy of Sciences* 100:16000–16005.

Canales A, Jia X, Froriep UP, Koppes RA, Tringides CM, Selvidge J, Lu C, Hou C, Wei L, Fink Y, Anikeeva P (2015) Multifunctional fibers for simultaneous optical , electrical and chemical interrogation of neural circuits in vivo. *Nature Biotechnology* 2:1–10.

Casanova F, Carney PR, Sarntinoranont M (2014) Effect of needle insertion speed on tissue injury, stress, and backflow distribution for convection-enhanced delivery in the rat brain. *PLoS ONE* 9.

Castagnola E, Maggiolini E, Ceseracciu L, Ciarpella F, Zucchini E, De Faveri S, Fadiga L, Ricci D (2016) pHEMA Encapsulated PEDOT-PSS-CNT Microsphere Microelectrodes for Recording Single Unit Activity in the Brain. *Frontiers in Neuroscience* 10:1–14.

Castelo-Branco M, Goebel R, Neuenschwander S, Singer W (2000) Neural synchrony correlates with surface segregation rules. *Nature* 405:685–689.

Chen TW, Wardill TJ, Sun Y, Pulver SR, Renninger SL, Baohan A, Schreiter ER, Kerr RA, Orger MB, Jayaraman V (2013) Ultrasensitive fluorescent proteins for imaging neuronal activity. *Nature* 499:295–300.

Chestek CA, Gilja V, Nuyujukian P, Kier RJ, Solzbacher F, Ryu SI, Harrison RR, Shenoy KV (2009) HermesC : Low-Power Wireless Neural Recording System for Freely Moving Primates. *IEEE Transactions on Neural Systems and Rehabilitation Engineering* 17:330–338.

Claverol-Tinture E, Nadasdy Z (2004) Intersection of Microwire ElectrodesWith Proximal CA1 Stratum-Pyramidale Neurons at Insertion for Multiunit Recordings Predicted by a 3-D Computer Model Enric. *IEEE Transactions on Biomedical Circuits and Systems* 51:2211–2216.

Cogan SF (2008) Neural stimulation and recording electrodes. *Annual Review of Biomedical Engineering* 10:275–309.

Cogan SF, Troyk PR, Ehrlich J, Plante TD, Detlefsen DE (2006) Potential-biased, asymmetric waveforms for charge-injection with activated iridium oxide (AIROF) neural stimulation electrodes. *IEEE Transactions on Biomedical Engineering* 53:327–332.

Conway BE, Mozota J (1983) Surface and bulk processes at oxidized iridium electrodes-II. Conductivity-switched behaviour of thick oxide films. *Electrochimica Acta* 28:9–16.

Csicsvari J, Henze DA, Jamieson B, Harris KD, Sirota A, Kenneth D (2003) Massively Parallel Recording of Unit and Local Field Potentials With Silicon-Based Electrodes. *Journal of Neurophysiology* 90:1314–1323.

Cui X, Martin DC (2003) Electrochemical deposition and characterization of poly(3,4-ethylenedioxythiophene) on neural microelectrode arrays. *Sensors and Actuators B: Chemical* 89:92–102.

Cybulski TR, Glaser JI, Marblestone AH, Zamft BM, Boyden ES, Church GM, Kording KP (2015) Spatial information in large-scale neural recordings. *Frontiers in Computational Neuroscience* 8:1–16.

Delgado Ruz I, Schultz SR (2014) Localising and classifying neurons from high density MEA recordings. *Journal of Neuroscience Methods* 233:115–128.

Denk W, Strickler J, Webb W (1990) Two-Photon Laser Scanning Fluorescence Microscopy. *Science* 248:73–76.

Desai M, Kahn I, Knoblich U, Bernstein J, Atallah H, Yang A, Kopell N, Buckner RL, Graybiel AM, Moore CI (2011) Mapping brain networks in awake mice using combined optical neural control and fMRI. *Journal of neurophysiology* 105:1393–1405.

Dombeck DA, Khabbaz AN, Collman F, Adelman TL, Tank DW (2007) Imaging Large-Scale Neural Activity with Cellular Resolution in Awake, Mobile Mice. *Neuron* 56:43–57.

Donald IW (1987) Production, properties and applications of microwire and related products. *Journal of Materials Science* 22:2661–2679.

Donoghue JP (2002) Connecting cortex to machines: recent advances in brain interfaces. *Nature Neuroscience* 5:1085–1088.

Drake KL, Wise KD, Farraye J, Anderson DJ, BeMent SL (1988) Performance of Planar Multisite Microprobes in Recording Extracellular Single-Unit Intracortical Activity. *IEEE Transactions on Biomedical Engineering* 35:719–732.

Du J, Riedel-Kruse IH, Nawroth JC, Roukes ML, Laurent G, Masmanidis SC (2009) High-resolution three-dimensional extracellular recording of neuronal activity with microfabricated electrode arrays. *Journal of neurophysiology* 101:1671–1678.

Ebner TJ, Chen G (1995) Use of voltage-sensitive dyes and optical recordings in the central nervous system. *Progress in Neurobiology* 46:463–506.

Elias J, Gizowska M, Brodard P, Widmer R, Dehazan Y, Graule T, Michler J, Philippe L (2012) Electrodeposition of gold thin films with controlled morphologies and their applications in electrocatalysis and SERS. *Nanotechnology* 23:255705.

Engel AK, Singer W (2001) Temporal binding and the neural correlates of sensory awareness. *Trends in Cognitive Sciences* 5:16–25.

Etemadi L, Mohammed M, Thorbergsson PT, Ekstrand J, Friberg A, Granmo M, Pettersson LME, Schouenborg J (2016) Embedded ultrathin cluster electrodes for long-term recordings in deep brain centers. *PLoS ONE* 11:1–18.

Eversmann B, Jenkner M, Hofmann F, Paulus C, Brederlow R, Holzapfl B, Fromherz P, Merz M, Brenner M, Schreiter M, Gabl R, Plehnert K, Steinhauser M, Eckstein G, Schmitt-Landsiedel D, Thewes R (2003) A 128 x 128 CMOS Biosensor Array for Extracellular Recording of Neural Activity. *IEEE Journal of Solid-State Circuits* 38:2306–2317.

Ferrea E, Maccione A, Medrihan L, Nieus T, Ghezzi D, Baldelli P, Benfenati F, Berdondini L (2012) Large-scale, high-resolution electrophysiological imaging of field potentials in brain slices with microelectronic multielectrode arrays. *Frontiers in Neural Circuits* 6:1–14.

Fields RD (2002) New Insights into Neuron-Glia Communication. *Science* 298:556–562.

Fiscella M, Farrow K, Jones IL, Jäckel D, Müller J, Frey U, Bakkum DJ, Hantz P, Roska B, Hierlemann A (2012) Recording from defined populations of retinal ganglion cells using a high-density CMOS-integrated microelectrode array with real-time switchable electrode selection. *Journal of Neuroscience Methods* 211:103–113.

Fitch MT, Doller C, Combs CK, Landreth GE, Silver J (1999) Cellular and molecular mechanisms of glial scarring and progressive cavitation: in vivo and in vitro analysis of inflammation-induced secondary injury after CNS trauma. *The Journal of neuroscience : the official journal of the Society for Neuroscience* 19:8182–98.

Frey U, Egert U, Heer F, Hafizovic S, Hierlemann A (2009) Microelectronic system for high-resolution mapping of extracellular electric fields applied to brain slices. *Biosensors and Bioelectronics* 24:2191–2198.

Frostig RD, Lieke EE, Ts'o DY, Grinvald A (1990) Cortical functional architecture and local coupling between neuronal activity and the microcirculation revealed by in vivo high-resolution optical imaging of intrinsic signals. *Proceedings of the National Academy of Sciences of the United States of America* 87:6082–6086.

Fukunaga I, Berning M, Kollo M, Schmaltz A, Schaefer AT (2012) Two distinct channels of olfactory bulb output. *Neuron* 75:320–329.

Gabay T, Ben-David M, Kalifa I, Sorkin R, Abrams ZR, Ben-Jacob E, Hanein Y (2007) Electro-chemical and biological properties of carbon nanotube based multi-electrode arrays. *Nanotechnology* 18:035201.

Geddes LA (1972) *Electrodes and the measurement of bioelectric events* Wiley-Interscience.

Gholipour B, Bastock P, Cui L, Craig C, Khan K, Hewak DW, Soci C (2016) Lithography Assisted Fiber-Drawing Nanomanufacturing. *Scientific Reports* 6:1–8.

Gilgunn PJ, Khilwani R, Kozai TDY, Weber DJ, Cui XT, Erdos G, Ozdoganlar OB, Fedder GK (2012) An ultra-compliant, scalable neural probe with molded biodissolvable delivery vehicle. *Proceedings of the IEEE International Conference on Micro Electro Mechanical Systems (MEMS)* pp. 56–59.

Gillis WF, Lissandrello CA, Shen J, Pearre BW, Mertiri A, Deku F, Cogan S, Holinski BJ, Chew DJ, White AE, Gardner TJ, Otchy TM (2017) Carbon Fiber On Polyimide Ultra-Microelectrodes. *bioRxiv* .

Glaser JI, Zamft BM, Marblestone AH, Moffitt JR, Tyo K, Boyden ES, Church G, Kording KP (2013) Statistical analysis of molecular signal recording. *PLoS Computational Biology* 9:1–14.

Gold C, Henze DA, Koch C, Buzsáki G (2006) On the origin of the extracellular action potential waveform: a modeling study. *Journal of Neurophysiology* 95:3113–3128.

Gray CM, Maldonado PE, Wilson M, McNaughton B (1995) Tetrodes markedly improve the reliability and yield of multiple single-unit isolation from multi-unit recordings in cat striate cortex. *Journal of Neuroscience Methods* 63:43–54.

Green R, Abidian MR (2015) Conducting Polymers for Neural Prosthetic and Neural Interface Applications. *Advanced Materials* pp. 7620–7637.

Green Ra, Hassarati RT, Bouchinet L, Lee CS, Cheong GLM, Yu JF, Dodds CW, Suaning GJ, Poole-Warren La, Lovell NH (2012) Substrate dependent stability of conducting polymer coatings on medical electrodes. *Biomaterials* 33:5875–5886.

Grewe BF, Langer D, Kasper H, Kampa BM, Helmchen F (2010) High-speed in vivo calcium imaging reveals neuronal network activity with near-millisecond precision. *Nature Methods* 7:399–405.

Guitchounts G, Markowitz JE, Liberti WA, Gardner TJ (2013) A carbon-fiber electrode array for long-term neural recording. *Journal of Neural Engineering* 10:1–13.

Hackwood S (1981) Anodic Evolution of Oxygen on Sputtered Iridium Oxide Films. *Journal of The Electrochemical Society* 128:2569–2573.

Hämäläinen MS, Hari R, Ilmoniemi RJ, Knuutila J, Lounasmaa OV (1993) Magnetoencephalography - theory, instrumentation, and applications to noninvasivee studies of the working human brain. *Reviews of Modern Physics* 65:413–505.

Hamill OP, Marty A, Neher E, Sakmann B, Sigworth FJ (1981) Improved patch-clamp techniques for high-resolution current recording from cells and cell-free membrane patches. *Pflügers Archiv European Journal of Physiology* 391:85–100.

Harris JP, Hess AE, Rowan SJ, Weder C, Zorman CA, Tyler DJ, Capadona JR (2011) In vivo deployment of mechanically adaptive nanocomposites for intracortical microelectrodes. *Journal of Neural Engineering* 8:1–13.

Harris KD, Henze DA, Csicsvari J, Hirase H, Buzsáki G (2000) Accuracy of tetrode spike separation as determined by simultaneous intracellular and extracellular measurements. *Journal of Neurophysiology* 84:401–14.

Harris KD (2005) Neural signatures of cell assembly organization. *Nature Reviews Neuroscience* 6:399–407.

Heim M, Yvert B, Kuhn A (2012) Nanostructuration strategies to enhance microelectrode array (MEA) performance for neuronal recording and stimulation. *Journal of Physiology - Paris* 106:137–45.

Helmchen F, Imoto K, Sakmann B (1996) Ca2+ buffering and action potential-evoked Ca2+ signaling in dendrites of pyramidal neurons. *Biophysical Journal* 70:1069–1081.

Helmchen F, Denk W, Kerr JND (2013) Miniaturization of two-photon microscopy for imaging in freely moving animals. *Cold Spring Harbor Protocols* 2013:904–913.

Henze D, Borhegyi Z, Csicsvari J, Mamiya A, Harris KD, Buzsáki G (2000) Intracellular features predicted by extracellular recordings in the hippocampus in vivo. *Journal of Neurophysiology* 84:390–400.

Hodgkin A, Huxley A (1952) A quantitative description of membrane current and its application to conduction and excitation in nerve. *The Journal of Physiology* 117:500–544.

Hopt A, Neher E (2001) Highly nonlinear photodamage in two-photon fluorescence microscopy. *Biophysical Journal* 80:2029–2036.

Hosseini NH, Hoffmann R, Kisban S, Stieglitz T, Paul O, Ruther P (2007) Comparative study on the insertion behavior of cerebral microprobes. *Proceedings of the 29th Annual International Conference of the IEEE Engineering in Medicine and Biology* pp. 4711–4714.

House PA, MacDonald JD, Tresco PA, Normann RA (2006) Acute microelectrode array implantation into human neocortex: preliminary technique and histological considerations. *Neurosurgical Focus* 20:1–4.

Hsieh CC, Wu CY, Jih FW, Sun TP (1997) Focal-plane-arrays and CMOS readout techniques of infrared imaging systems. *IEEE Transactions on Circuits and Systems for Video Technology* 7:594–605.

Hubel D (1957) Tungsten Microelectrode for Recording from Single Units. *Science* 125:549–550.

Hughes JR, Hendrix DE, Cohen J, Duffy FH, Mayman CI, Scholl ML, Cuffin BN (1976) Relationship of the magnetoencephalogram to the electroencephalogram. Normal wake and sleep activity. *Electroencephalography and Clinical Neurophysiology* 40:261–278.

Humphrey DR, Schmidt EM (1990) Extracellular Single-Unit Recording Methods In Boulton AA, Baker GB, Vanderwolf C, editors, *Neuromethods Vol. 15: Neurophysiological Techniques*. Humana Press.

Huys R, Braeken D, Jans D, Stassen A, Collaert N, Wouters J, Loo J, Severi S, Vleugels F, Callewaert G, Verstreken K, Bartic C, Eberle W (2012) Single-cell recording and stimulation with a 16k micro-nail electrode array integrated on a 0.18 μm CMOS chip. *Lab on a Chip* 12:1274.

Jan E, Hendricks JL, Husaini V, Richardson-Burns SM, Sereno A, Martin DC, Kotov NA (2009) Layered Carbon Nanotube-Polyelectrolyte Electrodes Outperform Traditional Neural Interface Materials. *Nano Letters* 9:4012–4018.

Jayant K, Hirtz JJ, Plante IJL, Tsai DM, De Boer WDAM, Semonche A, Peterka DS, Owen JS, Sahin O, Shepard KL, Yuste R (2016) Targeted intracellular voltage recordings from dendritic spines using quantum-dot-coated nanopipettes. *Nature Nanotechnology* 12:335–342.

Johnson LJ, Cohen E, Ilg D, Klein R, Skeath P, Scribner DA (2012) A novel high electrode count spike recording array using an 81,920 pixel transimpedance amplifier-based imaging chip. *Journal of Neuroscience Methods* 205:223–232.

Johnston, Wu (1995) *Foundations of cellular neurophysiology* The MIT Press.

Jun JJ, Mitelut C, Lai C, Gratiy SL, Anastassiou CA, Harris TD (2017) Real-time spike sorting platform for high-density extracellular probes with ground-truth validation and drift correction. *bioRxiv* pp. 1–33.

Kane SR, Cogan SF, Ehrlich J, Plante TD, McCreery DB, Troyk PR (2013) Electrical performance of penetrating microelectrodes chronically implanted in cat cortex. *IEEE Transactions on Biomedical Engineering* 60:2153–2160.

Keefer EW, Botterman BR, Romero MI, Rossi AF, Gross GW (2008) Carbon nanotube coating improves neuronal recordings. *Nature Nanotechnology* 3:434–439.

Kerr JND, Denk W (2008) Imaging in vivo: watching the brain in action. *Nature Reviews Neuroscience* 9:195–205.

Khodagholy D, Gelinas JN, Thesen T, Doyle W, Devinsky O, Malliaras GG, Buzsaki G (2015) NeuroGrid: recording action potentials from the surface of the brain. *Nature Neuroscience* 18:310–315.

Khodagholy D, Gelinas JN, Zhao Z, Yeh M, Long M, Greenlee JD, Doyle W, Devinsky O, Buzsaki G (2016) Organic electronics for high-resolution electrocorticography of the human brain. *Science Advances* 2:1–8.

Kim S, Bhandari R, Klein M, Negi S, Rieth L, Tathireddy P, Toepper M, Oppermann H, Solzbacher F (2009) Integrated wireless neural interface based on the Utah electrode array. *Biomedical Microdevices* 11:453–466.

Kim YT, Hitchcock RW, Bridge MJ, Tresco PA (2004) Chronic response of adult rat brain tissue to implants anchored to the skull. *Biomaterials* 25:2229–2237.

Klein JD, Clauson SL, Cogan SF (1989) Morphology and charge capacity of sputtered iridium oxide films. *Journal of Vacuum Science & Technology A* 7:3043–3047.

Kloosterman F, Davidson TJ, Gomperts SN, Layton SP, Hale G, Nguyen DP, Wilson MA (2009) Microdrive array for chronic in vivo recording: drive fabrication. *Journal of Visualized Experiments* pp. 1–4.

Kodandaramaiah SB, Franzesi GT, Chow BY, Boyden ES, Forest CR (2012) Automated whole-cell patch-clamp electrophysiology of neurons in vivo. *Nature Methods* 9:585–587.

Kolarcik CL, Luebben SD, Sapp SA, Hanner J, Snyder N, Kozai TDY, Chang E, Nabity JA, Nabity ST, Lagenaur CF, Cui XT (2015) Elastomeric and soft conducting microwires for implantable neural interfaces. *Soft Matter* 11:4847–61.

Kollo M, Schmaltz A, Abdelhamid M, Fukunaga I, Schaefer AT (2014) 'Silent' mitral cells dominate odor responses in the olfactory bulb of awake mice. *Nature Neuroscience* 17:1313–5.

Kozai TDY, Catt K, Li X, Gugel ZV, Olafsson VT, Vazquez AL, Cui XT (2015a) Mechanical failure modes of chronically implanted planar silicon-based neural probes for laminar recording. *Biomaterials* 37:25–39.

Kozai TDY, Jaquins-Gerstl AS, Vazquez AL, Michael AC, Cui XT (2015b) Brain tissue responses to neural implants impact signal sensitivity and intervention strategies. *ACS Chemical Neuroscience* 6:48–67.

Kozai TDY, Kipke DR (2009) Insertion shuttle with carboxyl terminated self-assembled monolayer coatings for implanting flexible polymer neural probes in the brain. *Journal of Neuroscience Methods* 184:199–205.

Kozai TDY, Langhals NB, Patel PR, Deng X, Zhang H, Smith KL, Lahann J, Kotov NA, Daryl R (2013) Ultrasmall implantable composite microelectrodes with bioactive surfaces for chronic neural interfaces. *Nature Materials* 11:1065–1073.

Kozai TDY, Langhals NB, Patel PR, Deng X, Zhang H, Smith KL, Lahann J, Kotov NA, Kipke DR (2012a) Ultrasmall implantable composite microelectrodes with bioactive surfaces for chronic neural interfaces. *Nature materials* 11:1065–73.

Kozai TDY, Vazquez AL, Weaver CL, Kim SG, Cui XT (2012b) In vivo two-photon microscopy reveals immediate microglial reaction to implantation of microelectrode through extension of processes. *Journal of Neural Engineering* 9:066001.

Kozlowski L (1996) Low-noise capacitive transimpedance amplifier performance versus alternative IR detector interface schemes in submicron CMOS. *Proceedings of SPIE* 2745.

Kralik JD, Dimitrov DF, Krupa DJ, Katz DB, Cohen D, Nicolelis Ma (2001) Techniques for long-term multisite neuronal ensemble recordings in behaving animals. *Methods* 25:121–50.

Kuzum D, Takano H, Shim E, Reed JC, Juul H, Richardson AG, de Vries J, Bink H, Dichter MA, Lucas TH, Coulter DA, Cubukcu E, Litt B (2014) Transparent and flexible low noise graphene electrodes for simultaneous electrophysiology and neuroimaging. *Nature Communications* 5:1–10.

Lacour SP, Benmerah S, Tarte E, Fitzgerald J, Serra J, McMahon S, Fawcett J, Graudejus O, Yu Z, Morrison B (2010) Flexible and stretchable micro-electrodes for in vitro and in vivo neural interfaces. *Medical and Biological Engineering and Computing* 48:945–954.

Lacour SP, Courtine G, Guck J (2016) Materials and technologies for soft implantable neuroprostheses. *Nature Reviews Materials* 1:16063.

Laurent G (2002) Olfactory network dynamics and the coding of multidimensional signals. *Nature Reviews Neuroscience* 3:884–895.

Lebedev MA, Nicolelis MAL (2006) Brain-machine interfaces: past, present and future. *Trends in Neurosciences* 29:536–546.

Lei N, Ramakrishnan S, Shi P, Orcutt JS, Yuste R, Kam LC, Shepard KL (2011) High-resolution extracellular stimulation of dispersed hippocampal culture with high-density CMOS multielectrode array based on non-Faradaic electrodes. *Journal of Neural Engineering* 8:1–6.

Leutgeb S (2005) Independent Codes for Spatial and Episodic Memory in Hippocampal Neuronal Ensembles. *Science* 309:619–623.

Lewicki MS (1998) A review of methods for spike sorting: the detection and classification of neural action potentials. *Network: Computation in Neural Systems* 9:R53–78.

Lind G, Linsmeier CE, Schouenborg J (2013) The density difference between tissue and neural probes is a key factor for glial scarring. *Scientific Reports* 3:1–7.

Lind G, Linsmeier CE, Thelin J, Schouenborg J (2010) Gelatine-embedded electrodes–a novel biocompatible vehicle allowing implantation of highly flexible microelectrodes. *Journal of Neural Engineering* 7.

Liu R, Chen R, Elthakeb AT, Lee SH, Hinckley S, Khraiche ML, Scott J, Pre D, Hwang Y, Tanaka A, Ro YG, Matsushita AK, Dai X, Soci C, Biesmans S, James A, Nogan J, Jungjohann KL, Pete DV, Webb DB, Zou Y, Bang AG, Dayeh SA (2017) High Density Individually Addressable Nanowire Arrays Record Intracellular Activity from Primary Rodent and Human Stem Cell Derived Neurons. *Nano Letters* 17:2757–5764.

Long M, Lee AK (2012) Intracellular recording in behaving animals. *Current Opinion in Neurobiology* 22:34–44.

Lopez CM, Putzeys J, Raducanu BC, Ballini M, Wang S, Andrei A, Rochus V, Vandebriel R, Severi S, Van Hoof C, Musa S, Van Helleputte N, Yazicioglu RF, Mitra S (2017) A Neural Probe With Up to 966 Electrodes and Up to 384 Configurable Channels in 0.13 μm SOI CMOS. *IEEE Transactions on Biomedical Circuits and Systems* pp. 1–14.

Lopez CM, Andrei A, Mitra S, Welkenhuysen M, Eberle W, Bartic C, Puers R, Yazicioglu RF, Gielen G (2014) An Implantable 455-Active-Electrode 52-Channel. *IEEE Journal of Solid-State Circuits* 49:1–14.

Lu C, Froriep UP, Koppes RA, Canales A, Caggiano V, Selvidge J, Bizzi E, Anikeeva P (2014) Polymer Fiber Probes Enable Optical Control of Spinal Cord and Muscle Function In Vivo. *Advanced Functional Materials* 24:6594–6600.

Luan L, Wei X, Zhao Z, Siegel JJ, Potnis O, Tuppen CA, Lin S, Kazmi S, Fowler RA, Holloway S, Dunn AK, Chitwood RA, Xie C (2017) Ultraflexible nanoelectronic probes form reliable, glial scar-free neural integration. *Science Advances* 3:1–10.

Ludwig KA, Uram JD, Yang J, Martin DC, Kipke DR (2006) Chronic neural recordings using silicon microelectrode arrays electrochemically deposited with a poly(3,4-ethylenedioxythiophene) (PEDOT) film. *Journal of Neural Engineering* 3:59–70.

Luo X, Weaver CL, Zhou DD, Greenberg R, Cui XT (2011) Highly stable carbon nanotube doped poly(3,4-ethylenedioxythiophene) for chronic neural stimulation. *Biomaterials* 32:5551–7.

Maccione A, Gandolfo M, Zordan S, Amin H, Di Marco S, Nieus T, Angotzi GN, Berdondini L (2015) Microelectronics, bioinformatics and neurocomputation for massive neuronal recordings in brain circuits with large scale multielectrode array probes. *Brain Research Bulletin* 119:118–126.

Maccione A, Hennig MH, Gandolfo M, Muthmann O, van Coppenhagen J, Eglen SJ, Berdondini L, Sernagor E (2014) Following the ontogeny of retinal waves: pan-retinal recordings of population dynamics in the neonatal mouse. *The Journal of Physiology* 592:1545–1563.

Mahvash M, Dupont PE (2010) Mechanics of dynamic needle insertion into a biological material. *IEEE Transactions on Biomedical Engineering* 57:934–943.

Mailley SC, Hyland M, Mailley P, McLaughlin JM, McAdams ET (2002) Electrochemical and structural characterizations of electrodeposited iridium oxide thin-film electrodes applied to neurostimulating electrical signal. *Materials Science and Engineering C* 21:167–175.

Malerba M, Angotzi G, Mandelbaum G, Sabatini B, Berdondini L (2016) A 512-channels, whole array readout, CMOS implantable probe for acute recordings in the brain In *Society for Neuroscience Meeting*.

Marblestone AH, Zamft BM, Maguire YG, Shapiro MG, Cybulski TR, Glaser JI, Amodei D, Stranges PB, Kalhor R, Dalrymple Da, Seo D, Alon E, Maharbiz MM, Carmena JM, Rabaey JM, Boyden ES, Church GM, Kording KP (2013) Physical principles for scalable neural recording. *Frontiers in Computational Neuroscience* 7:1–34.

Margrie TW, Brecht M, Sakmann B (2002) In vivo, low-resistance, whole-cell recordings from neurons in the anaesthetized and awake mammalian brain. *European Journal of Physiology* 444:491–498.

Maynard EM, Nordhausen CT, Normann RA (1997) The Utah Intracortical Electrode Array: a recording structure for potential brain-computer interfaces. *Electroencephalography and clinical Neurophysiology* 102:228–239.

McClain MA, Clements IP, Shafer RH, Bellamkonda RV, LaPlaca MC, Allen MG (2011) Highly-compliant, microcable neuroelectrodes fabricated from thin-film gold and PDMS. *Biomedical Microdevices* 13:361–373.

McNaughton BL, O'Keefe J, Barnes Ca (1983) The stereotrode: A new technique for simultaneous isolation of several single units in the central nervous system for multiple unit records. *Journal of Neuroscience Methods* 8:391–397.

Mendoza G, Peyrache A, Gámez J, Prado L, Buzsáki G, Merchant H (2016) Recording extracellular neural activity in the behaving monkey using a semi-chronic and high-density electrode system. *Journal of Neurophysiology* pp. 563–574.

Merrill DR, Bikson M, Jefferys JGR (2005) Electrical stimulation of excitable tissue: Design of efficacious and safe protocols. *Journal of Neuroscience Methods* 141:171–198.

Meyer RD, Cogan SF, Nguyen TH, Rauh RD (2001) Electrodeposited iridium oxide for neural stimulation and recording electrodes. *IEEE Transactions on Neural Systems and Rehabilitation Engineering* 9:2–11.

Michon F, Aarts A, Holzhammer T, Ruther P, Borghs G, McNaughton B, Kloosterman F (2016) Integration of silicon-based probes and micro-drive array for chronic recordings of large populations of neurons in behaving animals. *Journal of Neural Engineering* 13:1–11.

Müller J, Ballini M, Livi P, Chen Y, Radivojevic M, Shadmani A, Viswam V, Jones IL, Fiscella M, Diggelmann R, Stettler A, Frey U, Bakkum DJ, Hierlemann A (2015) High-resolution CMOS MEA platform to study neurons at subcellular, cellular, and network levels. *Lab on a Chip* 15:2767–2780.

Najafi K, Wise K (1986) An implantable multielectrode array with on-chip signal processing. *IEEE Journal of Solid-State Circuits* 21:1035–1044.

Nauhaus I, Nielsen KJ, Callaway EM (2012) Nonlinearity of two-photon Ca2+ imaging yields distorted measurements of tuning for V1 neuronal populations. *Journal of Neurophysiology* 107:923–936.

Negi S, Bhandari R, Rieth L, Van Wagenen R, Solzbacher F (2010) Neural electrode degradation from continuous electrical stimulation: Comparison of sputtered and activated iridium oxide. *Journal of Neuroscience Methods* 186:8–17.

Neto JP, Lopes G, Frazão J, Nogueira J, Lacerda P, Baião P, Aarts A, Andrei A, Musa S, Fortunato E, Barquinha P, Kampff AR (2016) Validating silicon polytrodes with paired juxtacellular recordings: method and dataset. *Journal of Neurophysiology* 116:892–903.

NeuroNexus (2008) Silicon Microelectrode array Research Product Catalog & Manual.

Neys J, Bentell J, O'Grady M, Vermeiren J, Colin T, Hooylaerts P, Grietens B (2008) Cheetah: a high frame rate, high resolution SWIR image camera. *Proceedings of SPIE* 7106.

Nguyen DP, Layton SP, Hale G, Gomperts SN, Davidson TJ, Kloosterman F, Wilson MA (2009) Microdrive array for chronic in vivo recording: tetrode assembly. *Journal of Visualized Experiments* pp. 1–3.

Nguyen-Vu TDB, Chen H, Cassell AM, Andrews RJ, Meyyappan M, Li J (2007) Vertically aligned carbon nanofiber architecture as a multifunctional 3-D neural electrical interface. *IEEE Transactions on Biomedical Engineering* 54:1121–1128.

Nicolelis MAL, Ghazanfar A, Faggin BM, Votaw S, Oliveira LM (1997) Reconstructing the engram: simultaneous, multisite, many single neuron recordings. *Neuron* 18:529–37.

Nicolelis MAL, Dimitrov D, Carmena JM, Crist R, Lehew G, Kralik JD, Wise SP (2003) Chronic, multisite, multielectrode recordings in macaque monkeys. *Proceedings of the National Academy of Sciences of the United States of America* 100:11041–11046.

Obien MEJ, Deligkaris K, Bullmann T, Bakkum DJ, Frey U (2015) Revealing neuronal function through microelectrode array recordings. *Frontiers in Neuroscience* 8:1–30.

Ogawa S, Lee T (1990) Brain magnetic resonance imaging with contrast dependent on blood oxygenation. *Proceedings of the National Academy of Sciences of the United States of America* 87:9868–72.

O'Keefe J, Recce ML (1993) Phase relationship between hippocampal place units and the EEG theta rhythm. *Hippocampus* 3:317–330.

Okun M, Lak A, Carandini M, Harris KD (2016) Long term recordings with immobile silicon probes in the mouse cortex. *PLoS ONE* 11:1–15.

Pachitariu M, Steinmetz N, Kadir S, Carandini M, Harris KD (2016) Kilosort : realtime spike-sorting for extracellular electrophysiology with hundreds of channels b c. *bioRxiv* pp. 1–14.

Packer AM, Russell LE, Dalgleish HWP, Häusser M (2014) Simultaneous all-optical manipulation and recording of neural circuit activity with cellular resolution in vivo. *Nature Methods* 12:140–146.

Panzeri S, Petersen RS, Schultz SR, Lebedev M, Diamond ME (2001) The role of spike timing in the coding of stimulus location in rat somatosensory cortex. *Neuron* 29.

Park DW, Schendel AA, Mikael S, Brodnick SK, Richner TJ, Ness JP, Hayat MR, Atry F, Frye ST, Pashaie R, Thongpang S, Ma Z, Williams JC (2014) Graphene-based carbon-layered electrode array technology for neural imaging and optogenetic applications. *Nature Communications* 5:5258.

Park S, Guo Y, Jia X, Choe HK, Grena B, Kang J, Park J, Lu C, Canales A, Chen R, Yim YS, Choi GB, Fink Y, Anikeeva P (2017) One-step optogenetics with multifunctional flexible polymer fibers. *Nature Neuroscience* pp. 1–8.

Patel PR, Na K, Zhang H, Kozai TDY, Kotov NA, Yoon E, Chestek CA (2015) Insertion of linear 8.4 μm diameter 16 channel carbon fiber electrode arrays for single unit recordings. *Journal of Neural Engineering* 12:046009.

Podgorski K, Ranganathan G (2016) Brain heating induced by near-infrared lasers during multiphoton microscopy. *Journal of Neurophysiology* 116:1012–1023.

Polikov VS, Tresco PA, Reichert WM (2005) Response of brain tissue to chronically implanted neural electrodes. *Journal of Neuroscience Methods* 148:1–18.

Pologruto T, Yasuda R, Svoboda K (2004) Monitoring Neural Activity and [Ca 2+] with Genetically Encoded Ca 2+ Indicators. *Journal of Neuroscience* 24:9572–9579.

Purves R (1981) *Microelectrode methods for intracellular recording and ionophoresis.* Academic Press.

Rancz EA, Franks KM, Schwarz MK, Pichler B, Schaefer AT, Margrie TW (2011) Transfection via whole-cell recording in vivo: bridging single-cell physiology, genetics and connectomics. *Nature Neuroscience* 14:527–532.

Rey HG, Pedreira C, Quian Quiroga R (2015) Past, present and future of spike sorting techniques. *Brain Research Bulletin* 119:106–117.

Rider D, Blavier Jf, Cunningham T, Hancock B, Key R, Pannell Z, Sander S, Seshadri S, Sun C, Wrigley C (2011) Fast Imaging Detector Readout Circuits with In-Pixel ADCs for Fourier Transform Imaging Spectrometers Technical report.

Robblee LS, Lekko JL, Brummer SB (1983) Activated Ir: An electrode suitable for reversible charge injection in saline solution. *Journal of The Electrochemical Society* 130:731–733.

Robinson JT, Jorgolli M, Park H (2013) Nanowire electrodes for high-density stimulation and measurement of neural circuits. *Frontiers in Neural Circuits* 7:38.

Rose TL, Robblee LS (1990) Electrical Stimulation with Pt Electrodes. VIII. Electrochemically Safe Charge Injection Limits with 0.2 ms Pulses. *IEEE Transactions on Biomedical Engineering* 37:1118–1120.

Rossant C, Kadir SN, Goodman DFM, Schulman J, Belluscio M, Buzsaki G, Harris KD (2015) Spike sorting for large, dense electrode arrays. *Nature Neuroscience* 19:634–41.

Ruther P, Paul O (2015) New approaches for CMOS-based devices for large-scale neural recording. *Current Opinion in Neurobiology* 32:31–37.

Scholvin J, Kinney JP, Bernstein JG, Moore-Kochlacs C, Kopell N, Fonstad CG, Boyden ES (2016) Close-packed silicon microelectrodes for scalable spatially oversampled neural recording. *IEEE Transactions on Biomedical Engineering* 63:120–130.

Schwarz DA, Lebedev MA, Hanson TL, Dimitrov DF, Lehew G, Meloy J, Rajangam S, Subramanian V, Ifft PJ, Li Z, Ramakrishnan A, Tate A, Zhuang KZ, Nicolelis MAL (2014) Chronic, wireless recordings of large-scale brain activity in freely moving rhesus monkeys. *Nature Methods* 11:670–676.

Serway RA (1998) *Principles of Physics* Fort Worth, Texas, 2nd edition.

Sharp AA, Ortega AM, Restrepo D, Curran-Everett D, Gall K (2009) In vivo penetration mechanics and mechanical properties of mouse brain tissue at micrometer scales. *IEEE Transactions on Biomedical Engineering* 56:45–53.

Shobe JL, Claar LD, Parhami S, Bakhurin KI, Masmanidis SC (2015) Brain activity mapping at multiple scales with silicon microprobes containing 1024 electrodes. *Journal of Neurophysiology* 114:2043–2052.

Smetters D, Majewska A, Yuste R (1999) Detecting Action Potentials in Neuronal Populations with Calcium Imaging. *Methods* 18:215–221.

Sofroniew NJ, Flickinger D, King J, Svoboda K (2016) A large field of view two-photon mesoscope with subcellular resolution for in vivo imaging. *eLife* 5:1–20.

Sohal HS, Jackson A, Jackson R, Clowry GJ, Vassilevski K, O'Neill A, Baker SN (2014) The sinusoidal probe: a new approach to improve electrode longevity. *Frontiers in Neuroengineering* 7:1–10.

Sridharan A, Nguyen JK, Capadona JR, Muthuswamy J (2016) Compliant Intracortical Implants Reduce Strains and Strain Rates in Brain Tissue In Vivo. *Journal of Neural Engineering* 3:973–982.

Steinmetz N, Pachitariu M, Rossant C, Hunter M, Burgess C, Carandini M, Harris K (2016) Dataset: simultaneous recording with two Neuropixels Phase3 electrode arrays.

Stevenson IH, Kording KP (2011) How advances in neural recording affect data analysis. *Nature Neuroscience* 14:139–142.

Stirman JN, Smith IT, Kudenov MW, Smith SL (2016) Wide field-of-view, multi-region, two-photon imaging of neuronal activity in the mammalian brain. *Nature Biotechnology* 34:857–862.

Suyatin DB, Wallman L, Thelin J, Prinz CN, Jörntell H, Samuelson L, Montelius L, Schouenborg J (2013) Nanowire-based electrode for acute in vivo neural recordings in the brain. *PLoS ONE* 8:1–8.

Takeuchi S, Ziegler D, Yoshida Y, Mabuchi K, Suzuki T (2005) Parylene flexible neural probes integrated with microfluidic channels. *Lab on a Chip* 5:519–23.

Tao G, Stolyarov AM, Abouraddy AF (2012) Multimaterial Fibers. *International Journal of Applied Glass Science* 3:349–368.

Tien LW, Wu F, Tang-Schomer MD, Yoon E, Omenetto FG, Kaplan DL (2013) Silk as a multifunctional biomaterial substrate for reduced glial scarring around brain-penetrating electrodes. *Advanced Functional Materials* 23:3185–3193.

Tonucci RJ, Hubler GK (2007) Materials characterization and nanofabrication methods - Nanochannel glass materials. *AIP Conference Proceedings* 959:59–71.

Van Hippel A (1944) Tables of Dielectric Materials Technical report.

Vincent T, Thiessen J, Kurjewicz L, Germscheid S, Turner A, Zhilkin P, Alexander M, Martin M (2010) Longitudinal Brain Size Measurements in APP/PS1 Transgenic Mice. *Magnetic Resonance Insights* 4:19–26.

Viventi J, Kim DH, Vigeland L, Frechette ES, Blanco Ja, Kim YS, Avrin AE, Tiruvadi VR, Hwang SW, Vanleer AC, Wulsin DF, Davis K, Gelber CE, Palmer L, Van der Spiegel J, Wu J, Xiao J, Huang Y, Contreras D, Rogers Ja, Litt B (2011) Flexible, foldable, actively multiplexed, high-density electrode array for mapping brain activity in vivo. *Nature Neuroscience* 14:1599–605.

Ward MP, Rajdev P, Ellison C, Irazoqui PP (2009) Toward a comparison of microelectrodes for acute and chronic recordings. *Brain Research* 1282:183–200.

Ware T, Simon D, Hearon K, Liu C, Shah S, Reeder J, Khodaparast N, Kilgard MP, Maitland DJ, Rennaker RL, Voit WE (2012) Three-dimensional flexible electronics enabled by shape memory polymer substrates for responsive neural interfaces. *Macromolecular Materials and Engineering* 297:1193–1202.

Weiland JD, Anderson DJ (2000) Chronic neural stimulation with thin-film, iridium oxide electrodes. *IEEE Transactions on Biomedical Engineering* 47:911–918.

Wellman SM, Eles JR, Ludwig KA, Seymour JP, Michelson NJ, Mcfadden WE, Vazquez AL, Kozai TD (2017) A Materials Roadmap to Functional Neural Interface Design. *Advanced Functional Materials* 1701269:1–38.

Wessberg J, Stambaugh CR, Kralik JD, Beck PD, Laubach M, Chapin JK, Kim J, Biggs SJ, Srinivasan MA, Nicolelis MAL (2000) Real-time prediction of hand trajectory by ensembles of cortical neurons in primates. *Nature* 408:361–365.

Wessling B, Mokwa W, Schnakenberg U (2006) RF-sputtering of iridium oxide to be used as stimulation material in functional medical implants. *Journal of Micromechanics and Microengineering* 16:S142–S148.

Wilks SJ, Richardson-Burns SM, Hendricks JL, Martin DC, Otto KJ (2009) Poly(3,4-ethylenedioxythiophene) as a Micro-Neural Interface Material for Electrostimulation. *Frontiers in Neuroengineering* 2:1–8.

Wilson M, McNaughton B (1993) Dynamics of the hippocampal ensemble code for space. *Science* 261:1055–1058.

Wilson M, McNaughton B (1994) Reactivation of Hippocampal Ensemble Memories During Sleep. *Science* 265:5–8.

Wise KD, Anderson DJ, Hetke JF, Kipke DR, Najafi K (2004) Wireless implantable microsystems: High-density electronic interfaces to the nervous system. *Proceedings of the IEEE* 92:76–97.

Wise KD, Angell JB, Starr A (1970) An Integrated-Circuit Approach to Extracellular Microelectrodes. *IEEE Transactions on Biomedical Engineering* BME-17:238–247.

Wise KD, Sodagar AM, Yao Y, Gulari MN, Perlin GE, Najafi K (2008) Implantable Neural Microsystems. *Proceedings of the IEEE* 96:1184–1202.

Xiang Z, Yen SC, Xue N, Sun T, Tsang WM, Zhang S, Liao LD, Thakor NV, Lee C (2014) Ultra-thin flexible polyimide neural probe embedded in a dissolvable maltose-coated microneedle. *Journal of Micromechanics and Microengineering* 24:1–11.

Xiao Y, Martin DC, Cui X, Shenai M (2006) Surface modification of neural probes with conducting polymer poly(hydroxymethylated-3,4- ethylenedioxythiophene) and its biocompatibility. *Applied Biochemistry and Biotechnology* 128:117–130.

Xie C, Liu J, Fu TM, Dai X, Zhou W, Lieber CM (2015) Three-dimensional macroporous nanoelectronic networks as minimally invasive brain probes. *Nature Materials* 14:1286–1292.

Yamamoto J, Wilson MA (2008) Large-Scale Chronically Implantable Precision Motorized Microdrive Array for Freely Behaving Animals. *Journal of Neurophysiology* 100:2430–2440.

Yaman M, Khudiyev T, Ozgur E, Kanik M, Aktas O, Ozgur EO, Deniz H, Korkut E, Bayindir M (2011) Arrays of indefinitely long uniform nanowires and nanotubes. *Nature Materials* 10:494–501.

Yamanaka K (1989) Anodically Electrodeposited Iridium Oxide Films (AEIROF) from Alkaline Solutions for Electrochromic Display Devices. *Japanese Journal of Applied Physics* 28:632–637.

Yamazaki K (1995) Elastic Interconnector.

Yang W, Miller JeK, Carrillo-Reid L, Pnevmatikakis E, Paninski L, Yuste R, Peterka DS (2016) Simultaneous Multi-plane Imaging of Neural Circuits. *Neuron* 89:284.

Yizhar O, Fenno LE, Davidson TJ, Mogri M, Deisseroth K (2011) Optogenetics in neural systems. *Neuron* 71:9–34.

Yoon H, Hankins P, Oh S, Harbaugh RE, Varadan VK (2010) Heterostructured IrO2/Au Nanowire Electrodes and Unit Recordings From Hippocampal Rat Brain. *Journal of Nanotechnology in Engineering and Medicine* 1:1–4.

Zong W, Wu R, Li M, Hu Y, Li Y, Li J, Rong H, Wu H, Xu Y, Lu Y, Jia H, Fan M, Zhou Z, Zhang Y, Wang A, Chen L, Cheng H (2017) Fast high-resolution miniature two-photon microscopy for brain imaging in freely behaving mice. *Nature Methods* 14:713–719.